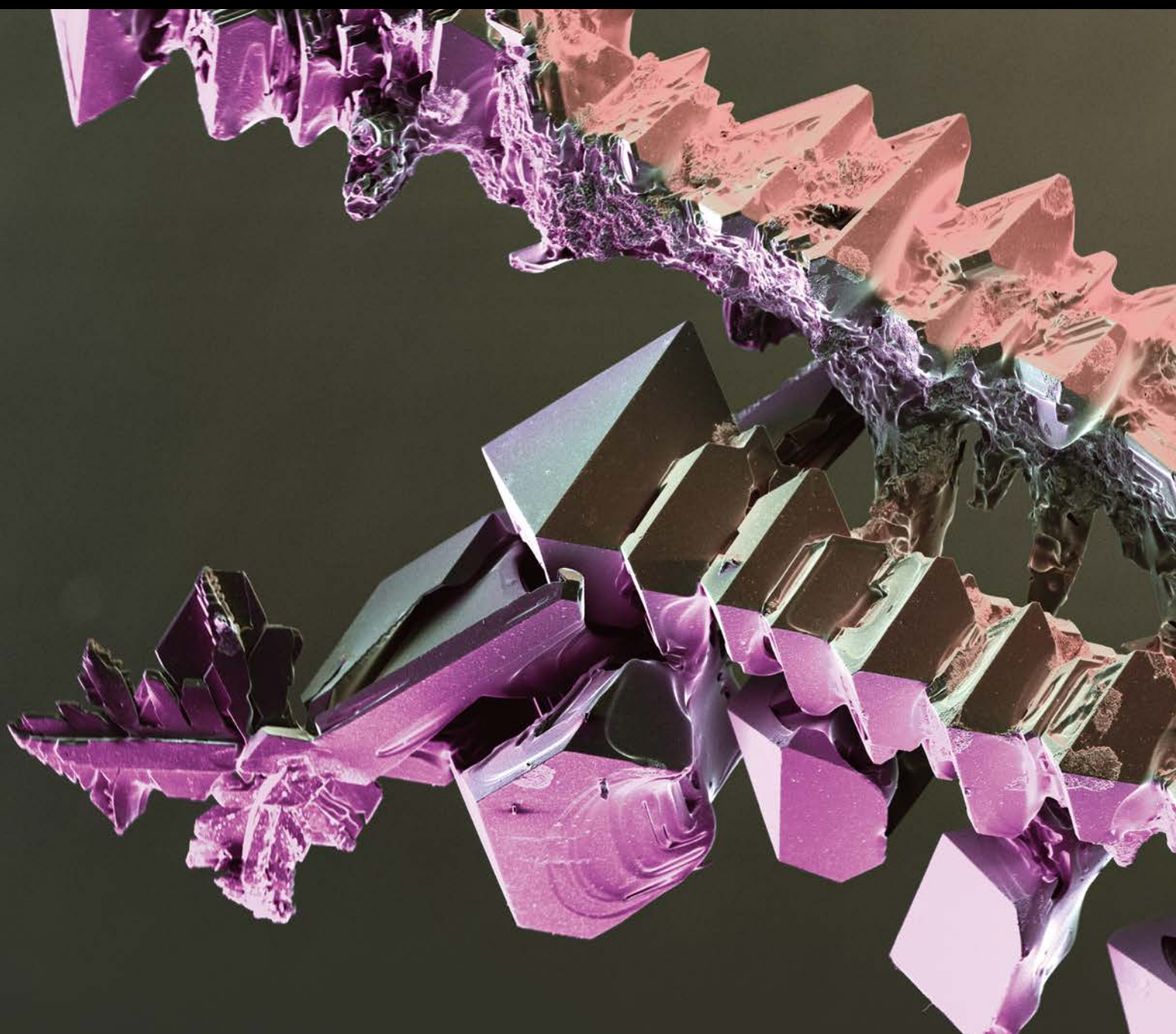


International Journal of Chemical Engineering

Exergetic Optimization of Power Generation Systems

Guest Editors: Pouria Ahmadi, Halil S. Hamut, Ahmadreza Ghaffarizadeh, Pedram Hanafizadeh, and Esmail Ghasemisahebi





Exergetic Optimization of Power Generation Systems

Exergetic Optimization of Power Generation Systems

Guest Editors: Pouria Ahmadi, Halil S. Hamut,
Ahmadreza Ghaffarizadeh, Pedram Hanafizadeh,
and Esmail Ghasemisahebi



Copyright © 2016 Hindawi Publishing Corporation. All rights reserved.

This is a special issue published in “International Journal of Chemical Engineering.” All articles are open access articles distributed under the Creative Commons Attribution License, which permits unrestricted use, distribution, and reproduction in any medium, provided the original work is properly cited.

Editorial Board

Jerzy Bałdyga, Poland
Mostafa Barigou, UK
Gino Baron, Belgium
Giuseppe Caputo, Italy
Raghunath V. Chaudhari, USA
Jean-Pierre Corriou, France
Sébastien Déon, France
Donald L. Feke, USA
Jinlong Gong, China
Thomas R. Hanley, USA
Michael Harris, USA

Xijun Hu, Hong Kong
M. G. Ierapetritou, USA
Konstantinos Kakosimos, Qatar
Dilhan M. Kalyon, USA
Iftekhhar A. Karimi, Singapore
Bhaskar Kulkarni, India
Deepak Kunzru, India
Janez Levec, Slovenia
Jose C. Merchuk, Israel
Subrata Mondal, India
Badie I. Morsi, USA

Sohail Murad, USA
Dmitry Murzin, Finland
Doraiswami Ramkrishna, USA
Jose Alberto Romagnoli, USA
Evangelos Tsotsas, Germany
Toshinori Tsuru, Japan
Junwu Wang, China
Tapio Westerlund, Finland
Jaime Wisniak, Israel
King Lun Yeung, Hong Kong

Contents

Exergetic Optimization of Power Generation Systems

Pouria Ahmadi, Halil S. Hamut, Ahmadreza Ghaffarizadeh, Pedram Hanafizadeh,
and Esmail Ghasemisahebi

Volume 2016, Article ID 3962847, 2 pages

Exergy and Exergoenvironmental Analysis of a CCHP System Based on a Parallel Flow Double-Effect Absorption Chiller

Ali Mousafarash

Volume 2016, Article ID 2370305, 8 pages

Exergy and Environmental Impact Assessment between Solar Powered Gas Turbine and Conventional Gas Turbine Power Plant

Ali Rajaei, Hasan Barzegar Avval, and Elmira Eslami

Volume 2016, Article ID 8323859, 8 pages

Performance Assessment of a Hybrid Solar-Geothermal Air Conditioning System for Residential Application: Energy, Exergy, and Sustainability Analysis

Yasser Abbasi, Ehsan Baniasadi, and Hossein Ahmadikia

Volume 2016, Article ID 5710560, 13 pages

Exact Optimum Design of Segmented Thermoelectric Generators

M. Zare, H. Ramin, S. Naemi, and R. Hosseini

Volume 2016, Article ID 6914735, 11 pages

Power Prediction and Technoeconomic Analysis of a Solar PV Power Plant by MLP-ABC and COMFAR III, considering Cloudy Weather Conditions

M. Khademi, M. Moadel, and A. Khosravi

Volume 2016, Article ID 1031943, 8 pages

Modeling and Assessment of a Biomass Gasification Integrated System for Multigeneration Purpose

Shoailb Khanmohammadi, Kazem Atashkari, and Ramin Kouhikamali

Volume 2016, Article ID 2639241, 11 pages

Editorial

Exergetic Optimization of Power Generation Systems

**Pouria Ahmadi,¹ Halil S. Hamut,² Ahmadreza Ghaffarizadeh,³
Pedram Hanafizadeh,⁴ and Esmail Ghasemisahebi⁵**

¹*Fuel Cell Research Lab (FCReL), Simon Fraser University (SFU), Vancouver, BC, Canada*

²*Technological Research Council of Turkey, Kocaeli, Turkey*

³*University of Southern California, Los Angeles, CA, USA*

⁴*University of Tehran, Tehran, Iran*

⁵*Florida International University, Miami, FL, USA*

Correspondence should be addressed to Pouria Ahmadi; pahmadi@sfu.ca

Received 19 May 2016; Accepted 19 May 2016

Copyright © 2016 Pouria Ahmadi et al. This is an open access article distributed under the Creative Commons Attribution License, which permits unrestricted use, distribution, and reproduction in any medium, provided the original work is properly cited.

With increasing global population and dwindling energy sources, generation of energy in a cost-effective manner with minimum waste and environmental footprint becomes one of the greatest challenges of our time. Thus, there is an increasing need for more capable and intelligent use of energy sources by incorporating enriched designs and optimized algorithms to enhance the sustainability of energy systems through innovative solutions. In this regard, the methods and tools for novel analyses and evaluation of energy systems to improve their efficiency and reduce their cost and environmental impact become imperative and require significant attention.

Recently, exergy has become a new distinct discipline for system design, analysis, optimization, and performance evaluation; and its use has been expanded drastically. Many researchers and practicing engineers refer to exergy methods as powerful tools for analyzing, assessing, designing, improving, and optimizing systems and processes. Exergy analysis appears to be an important tool to industry in (a) addressing the impact of energy resource utilization on the environment and economics, (b) furthering the goal of more efficient energy resource utilization, (c) determining locations, types, and true magnitudes of wastes and losses, (d) revealing whether or not and how much it is possible to design more efficient energy systems by reducing the inefficiencies, and (e) providing a sustainable development as a result of sustainable supply of energy resources. Exergy analysis is a method that uses the conservation of mass and conservation of energy

principles together with the second law of thermodynamics for the analysis, design, and improvement of energy systems. The exergy method is a useful tool for furthering the goal of more efficient energy resource use, for it enables the locations, types, and true magnitudes of wastes and losses to be determined. Many engineers and scientists suggest that the thermodynamic performance of a process is best evaluated by performing an exergy analysis in addition to or in place of conventional energy analysis because exergy analysis appears to provide more insights and to be more useful in efficiency improvement efforts than energy analysis.

In the following, a brief overview and summary of the individual contributions are given.

The first contribution in this issue from S. Khanmohammadi et al. (University of Guilan, Rasht, Iran) is titled “Modeling and Assessment of a Biomass Gasification Integrated System for Multigeneration Purpose.” This paper focuses on the accurate modeling of biomass gasification process and the optimal design of a multigeneration system (heating, cooling, electrical power, and hydrogen as energy carrier) to take the advantage of this clean energy. In the process of gasification modeling, a thermodynamic equilibrium model based on Gibbs energy minimization is used. The results show that with exergy efficiency as an objective function this parameter can increase from 19.6% in the base case to 21.89% in the optimized case. Also, for the total cost rate of the system as an objective function, it can decrease from 154.4 \$/h to 145.1 \$/h.

The paper by M. Khademi et al. (Islamic Azad University, South Tehran Branch, Tehran, Iran) is titled "Power Prediction and Technoeconomic Analysis of a Solar PV Power Plant by MLP-ABC and COMFAR III, considering Cloudy Weather Conditions." The authors try to predict the output power of a 3.2 kW PV power plant using the MLP-ABC (multilayer perceptron-artificial bee colony) algorithm. Experimental data (ambient temperature, solar radiation, and relative humidity) were gathered at five-minute intervals from Tehran University's PV Power Plant from September 22, 2012, to January 14, 2013. A detailed economic analysis is also presented for sunny and cloudy weather conditions using COMFAR III software. A detailed cost analysis indicated that the total investment payback period would be 3.83 years in sunny periods and 4.08 years in cloudy periods. The results showed that the solar PV power plant is feasible from an economic point of view in both cloudy and sunny weather conditions.

The paper "Exact Optimum Design of Segmented Thermoelectric Generators" by M. Zare et al. (Amirkabir University of Technology, Tehran, Iran) highlights the importance of thermoelectric generator for power generation. This study mainly focuses on the employment of exact method for design and optimization of STEGs and comparison of exact and approximate results. Thus, using new, highly efficient thermoelectric materials, four STEGs are proposed to operate in the temperature range of 300 to 1300 Kelvins. Design and performance characteristics of the optimized generators, including maximum conversion efficiency and length of elements, are calculated through both exact and approximate methods. The comparison indicates that the approximate method can cause a difference up to 20% in the calculation of some design characteristics despite its appropriate results in efficiency calculation. The results also show that the maximum theoretical efficiency of 23.08% is achievable using the new proposed STEGs.

The paper by Y. Abbasi et al. (University of Isfahan, Isfahan) is entitled "Performance Assessment of a Hybrid Solar-Geothermal Air Conditioning System for Residential Application: Energy, Exergy, and Sustainability Analysis." This paper investigates the performance of a ground source heat pump that is coupled with a photovoltaic system to provide cooling and heating demands of a zero-energy residential building. Exergy and sustainability analyses have been conducted to evaluate the exergy destruction rate and SI of different compartments of the hybrid system. The results show that the exergetic efficiency of the solar-geothermal heat pump system does not exceed 10 percent, and most exergy destruction takes place in photovoltaic panel, condenser, and evaporator. Although SI of PV system remains constant during a year, SI of GSHP varies depending on cooling and heating mode. The results also show that utilization of this hybrid system can reduce CO₂ emissions by almost 70 tons per year.

Exergy and exergoenvironmental analysis of a CCHP system based on a parallel flow double-effect absorption chiller is conducted by A. Mousafarash (Shahid Rajaee Teacher Training University, Tehran, Iran). A CCHP system is comprised of a gas turbine, a heat recovery steam generator, and a double-effect absorption chiller. Exergy and exergoeconomic analyses are conducted as a potential tool to assess the system.

The results show that exergy efficiency of the CCHP system is higher than the power generation system and the cogeneration system. In addition, the results indicate that when waste heat is utilized in the heat recovery steam generator, the greenhouse gasses are reduced when the fixed power output is generated. In addition, an increase in gas turbine inlet temperature increases the system exergy efficiency and decreases the total exergy destruction rate consequently.

The last paper of this special issue by A. Rajaei et al. (Power and Water University of Technology, Tehran, Iran) is titled "Exergy and Environmental Impact Assessment between Solar Powered Gas Turbine and Conventional Gas Turbine Power Plant." In this paper a comprehensive comparison between these two systems in terms of energy, exergy, and environmental impacts is carried out. To evaluate the effects of energy resources relevantly, exergy destruction rates are categorized into two types: renewable and nonrenewable which expresses how much green the cycles are. Nonrenewable exergy destruction and loss are reduced compared to GT with the recuperator cycle by 34.89% and 47.41%, respectively. They defined a renewable factor to evaluate resources quality and measure how green an exergy loss or destruction or a system as a whole is. Reduction in CO₂, NO_x, and CO compared to GT with the recuperator cycle by 49.92%, 66.14%, and 39.77%, respectively, is in line with the renewable factor value of around 55.7 which proves the ability of the proposed green measure to evaluate and compare the cycles' performance.

This special issue tried to shed light on the importance of exergy analysis for better design, better efficiency, and better assessment of power generation systems. The exergy analysis has been extended to include environmental, economical, and societal considerations. Environmental issues such as air pollution, global warming, and recycling have been linked to exergy. In this regard, some methods such as "exergoecology" and "exergoenvironment" have been proposed. We are confident that there will be more advancements in this field which will be seen in the coming years. Although exergy analysis has helped to design more efficient energy systems, the connection between economy and environment is necessary as well.

Acknowledgments

We would like to express our sincere thanks to all the reviewers for the time they spent on the review process of this special issue.

*Pouria Ahmadi
Halil S. Hamut
Ahmadreza Ghaffarizadeh
Pedram Hanafizadeh
Esmail Ghasemisahebi*

Research Article

Exergy and Exergoenvironmental Analysis of a CCHP System Based on a Parallel Flow Double-Effect Absorption Chiller

Ali Mousafarash

Mechanical Engineering Department, Shahid Rajaee Teacher Training University (SRTTU), Tehran 16788 15811, Iran

Correspondence should be addressed to Ali Mousafarash; alimoosafarash@gmail.com

Received 3 November 2015; Revised 27 March 2016; Accepted 14 April 2016

Academic Editor: Halil S. Hamut

Copyright © 2016 Ali Mousafarash. This is an open access article distributed under the Creative Commons Attribution License, which permits unrestricted use, distribution, and reproduction in any medium, provided the original work is properly cited.

A combined cooling, heating, and power (CCHP) system which produces electricity, heating, and cooling is modeled and analyzed. This system is comprised of a gas turbine, a heat recovery steam generator, and a double-effect absorption chiller. Exergy analysis is conducted to address the magnitude and the location of irreversibilities. In order to enhance understanding, a comprehensive parametric study is performed to see the effect of some major design parameters on the system performance. These design parameters are compressor pressure ratio, gas turbine inlet temperature, gas turbine isentropic efficiency, compressor isentropic efficiency, and temperature of absorption chiller generator inlet. The results show that exergy efficiency of the CCHP system is higher than the power generation system and the cogeneration system. In addition, the results indicate that when waste heat is utilized in the heat recovery steam generator, the greenhouse gasses are reduced when the fixed power output is generated. According to the parametric study results, an increase in compressor pressure ratio shows that the network output first increases and then decreases. Furthermore, an increase in gas turbine inlet temperature increases the system exergy efficiency, decreasing the total exergy destruction rate consequently.

1. Introduction

Fossil fuels release harmful gases to the atmosphere; in addition, they have limited resources that will be exhausted in the early future. Such a fact makes the world face a serious crisis in the 21st century. An increase in earth temperature and seriousness of greenhouse gases may burden extra costs on industries and the economy of those countries with high per capita consumption. Due to fossil fuel depletion, increasing fuel prices, and energy demand the use of high efficiencies power plants is very important. In traditional power generation systems a large amount of heat is lost by exhaust gases. Consequently using of waste heat increases power plant's efficiency. The combined cooling, heating, and power (CCHP) is a system that can produce power, heating, and cooling from a common energy source such as natural gas, oil, or sun. In a CCHP system, waste heat drives heating and cooling devices. The waste heat can be used for space heating, domestic hot water production, or production of steam. The waste heat can be used for cooling by driving a refrigeration system like an absorption chiller. The overall

energy efficiency of a trigeneration plant can attain 80% [1]. Through the absorption chiller and heat recovery steam generator in these systems, the extra heat releasing from the gas turbine can provide the needed cryogenic and thermal energies of a given site and supply the electricity without any separate consumption of fuel.

In recent years, economy is not the only matter; built environment is important too. Numerous studies have been carried out to reduce the greenhouse gas emissions and there have been several efforts worldwide to come up with plans and strategies for global warming mitigation. Nowadays, environmental impact of a plant is a design consideration beside the plants' economy. Furthermore, due to energy resources shortages, systems are designed to utilize the energy sources as efficient as possible. Economy, environment, and sustainability of energy resources are the basic criteria for any energy systems. By the advent of the exergy definition, exergy efficiency has become popular since it has a close relation with sustainability. Furthermore, because exergy evaluates the exact value of the extractable work from a stream or resource, it is more suitable for economic evaluation and

analysis. Hence, the exergy-economic and environmental assessment and modeling approach is an acceptable method for analyzing and designing the energy systems.

Exergy efficiency stands for energy sources management but linked with the economy of the plant and has a direct relationship with environmental emission. Since then it is always subjected to optimization. Other objectives are cost of the plant and emission. Nowadays, carbon taxes and emission cost are evaluated and implemented in plant cost considerations. Other emissions like NO_x , SO_x , and CO which are classified as toxic or hazard gases have their own costs and taxes as well. To evaluate the exact plant cost these issues must add to the total cost of the plant.

Havelský [2] analyzed the problem of energy efficiency evaluation of cogeneration systems for combined heating, cooling, and power production and presented equations for energy efficiency and primary energy savings. Athanasovici et al. [3] offered a unified comparison method for the thermodynamic efficiency of combined heat and power plants. A comparison between separate and combined energy production processes has been studied by using this analysis method. Minciuc et al. [4] proposed a method for the analysis of triple generation systems and established some limiting thermodynamic boundaries for optimum performance of triple generation systems combined with absorption chiller.

Sahoo [5] performed economic energy for a combined power and heat system. Huicochea et al. [6] analyzed theoretically the thermodynamic performance of a trigeneration system formed by a microturbine and a double-effect water/LiBr absorption chiller and evaluated that at different operating conditions. Ahmadi et al. [7] carried out energy and exergy analyses, environmental impact assessments, and related parametric studies for a trigeneration system. Their results show that trigeneration exhibits higher exergy efficiencies and lower environmental impacts compared to typical combined heat and power systems or gas turbine cycles.

Al-Sulaiman et al. [8] indicated that using the trigeneration plant compared with the power cycle eventuated efficiency gain of more than 22%. They also demonstrate the maximum efficiency is 74% for the trigeneration system, 71% for CHP system, and 46% for net electricity generation. Amrollahi et al. [9] performed thermodynamic analysis of postcombustion CO_2 capture in a natural gas-fired power plant. Rezaie and Rosen [10] have reviewed district energy systems and possible future developments. They discussed various assortments, definitions, and applications of district cooling and heating and described elements of a district energy system.

In this research study, exergy and environmental impact assessment are performed for a trigeneration system based on a parallel flow double-effect absorption chiller modeled by thermodynamic equations. The parametric evaluations of changes on selected design parameters (compressor pressure ratio, gas turbine inlet temperature, gas turbine isentropic efficiency, compressor isentropic efficiency, and temperature of absorption chiller generator inlet) on exergy and energy efficiencies were evaluated.

2. Energy Analysis

In this part, the CCHP cycle is modeled using EES software, by thermodynamic equations. To determine energy of different lines, it is required to identify thermodynamic parameters of the cycle through modeling its components. Modeling of each component is performed in terms of the first law and mass-energy balance law. Next, exergy of various points in the cycle, shown in Figure 1, is calculated and exergy efficiency and destruction are computed by writing the exergy balance for every component of the cycle.

2.1. Gas Turbine Cycle. Gas turbine cycle was modeled based on first law of thermodynamics. As shown in Figure 1, the air enters the compressor at ambient conditions (point 1); hot air then enters a combustion chamber where fuel is injected to increase its temperature at point 3. Next, the flue gas generated from combustion in the combustion chamber is extracted (point 3) and the power is produced by passing this gas from gas turbine (point 4). Gas turbine cycle wastes typically occur in three main components including compressor, combustion chamber, and gas turbine. To calculate irreversibility computations for each component, it is required to consider each of them as a control volume. Energy balance and the governing equations of this cycle components are as follows.

Air compressor:

$$T_2 = T_1 \left(1 + \frac{1}{\eta_c} \left(r_c^{\gamma_a - 1} - 1 \right) \right), \quad (1)$$

$$\dot{W}_c = \dot{m}_a C_{pa} (T_2 - T_1),$$

where \dot{m}_a is air mass flow rate, η_c is air compressor isentropic efficiency, γ_a is specific heat ratio, r_c is compressor pressure ratio, and C_{pa} is considered a function of temperature as follows [11]:

$$C_{pa}(T) = 1.048 - \left(\frac{1.83T}{10^4} \right) + \left(\frac{9.45T^2}{10^7} \right) - \left(\frac{5.49T^3}{10^{10}} \right) + \left(\frac{7.92T^4}{10^{14}} \right). \quad (2)$$

Combustion chamber:

$$\dot{m}_a h_2 + \dot{m}_f \text{LHV} = \dot{m}_g h_3 + (1 - \eta_{CC}) \dot{m}_f \text{LHV},$$

$$\frac{P_3}{P_2} = (1 - \Delta P_{CC}), \quad (3)$$

$$\dot{m}_g = \dot{m}_a + \dot{m}_f.$$

Gas turbine:

$$T_4 = T_3 \left(1 - \eta_{GT} \left(1 - r_{GT}^{(1-\gamma_g)/\gamma_g} \right) \right),$$

$$\dot{W}_{GT} = \dot{m}_g C_{pg} (T_3 - T_4), \quad (4)$$

$$\dot{W}_{net} = \dot{W}_{GT} - \dot{W}_c,$$

where \dot{m}_f is fuel mass flow rate, \dot{m}_a is air mass flow rate, \dot{m}_g is combustion gases mass flow rate, LHV is the fuel lower heating value, η_{CC} is combustion chamber efficiency, γ_g is combustion gases specific heat ratio, r_{GT} is gas turbine pressure ratio, and C_{pg} is considered a function of temperature as follows [11]:

$$C_{pg}(T) = 0.991 + \left(\frac{6.997T}{10^5}\right) + \left(\frac{2.712T^2}{10^7}\right) - \left(\frac{1.2244T^3}{10^{10}}\right). \quad (5)$$

2.2. Heat Recovery Steam Generator (HRSG). The considered single pressure HRSG consists of an economizer and an evaporator to produce steam. The supply water enters first to the economizer and its temperature rises up to saturation temperature. Then, it enters to the evaporator and vapor quality approaches 1 at a constant temperature and pressure. Some of the vapor enters to absorption chiller and the remaining is used in heat applications. The energy balance for the assumed HRSG is as follows.

Evaporator:

$$\dot{m}_g C_{pg}(T_a - T_b) = \dot{m}_{36}(h_{37} - h_{36}). \quad (6)$$

Economizer:

$$\begin{aligned} \dot{m}_g C_{pg}(T_4 - T_a) &= \dot{m}_{37}(h_{38} - h_{37}), \\ PP &= T_a - T_{38}, \\ AP &= T_{38} - T_{37}, \end{aligned} \quad (7)$$

where C_{pg} is combustion gases specific heat at constant pressure and the pinch point (PP) is defined as the difference between the temperature of the gas at the entrance of the evaporator (T_a) and the saturation temperature (T_{38}) and the approach point (AP) is the temperature differences between the water leaving the economizer (T_{37}) and the saturation temperature (T_{38}).

2.3. Double-Effect Absorption Chiller. In the considered CCHP system in this study, a Li-Br parallel flow double-effect absorption chiller is modeled. It must be noted that, during modeling of this chiller, the hot water output flowing from high-temperature generator (point 6) was used for heating the convection flow of the water and lithium bromide solution to increase the chiller performance. Doing so, coefficient performance of the proposed model increases to about 0.1. Each component of the chiller is assumed as a control volume and their mass-energy balance and thermodynamic equations are expressed as follows [7]:

$$\begin{aligned} \sum \dot{m}_{in} &= \sum \dot{m}_{out}, \\ \sum (\dot{m}x)_{in} &= \sum (\dot{m}x)_{out}, \\ \dot{Q} - \dot{W} &= \sum (\dot{m}h)_{out} - \sum (\dot{m}h)_{in}, \end{aligned} \quad (8)$$

where \dot{m} is working fluid mass flow rate and x is mass concentration of Li-Br in the solution.

2.4. Assumptions. Several assumptions have been used to simplify the model:

- (i) All the processes are done at steady state.
- (ii) Natural gas is the fuel used in the combustion chamber.
- (iii) The dead state is $P_0 = 1.01$ bar and $T_0 = 293.15$ K.
- (iv) Air and combustion products are assumed to be ideal-gas mixtures.

3. Exergy Analysis

Exergy in a system of ideal machines is defined as the maximum theoretical expedient work that may be received from energy. Frankly, exergy is not summarized in a single process and could be diminished as a result of irreversibility. In this way, it is possible to separately scrutinize each portion of the cycle and to attain the share of each element in the overall energy loss of the cycle. Concerning gas turbine power plants, with respect to any input fuel or flow into the power plant, the maximum capacity of the power plant can be calculated via exergy analysis. Exergy of matter flow can be categorized into its major constituents comprising kinetic, potential, physical, and chemical exergies. In this paper, kinetic and potential exergies are ignored due to their dispensable rates. Physical exergy is defined as the maximum theoretical useful work acquired whilst a system interacts with an equilibrium state [12]. Chemical exergy is connected with the departure of the chemical composition of a system from its chemical equilibrium. Chemical exergy is an imperative part of exergy in the combustion process [13]. Using the first and second laws of thermodynamics, we have the following exergy balance:

$$\dot{E}x_Q + \sum_{in} \dot{m}_i ex_i = \sum_{out} \dot{m}_o ex_o + \dot{E}x_W + \dot{E}x_D, \quad (9)$$

where ex is total specific exergy and $\dot{E}x_D$ is exergy destruction rate; other terms in this equation are defined as follows [14]:

$$\begin{aligned} \dot{E}x_Q &= \left(1 - \frac{T_0}{T_i}\right) \dot{Q}_i, \\ \dot{E}x_W &= \dot{W}, \\ ex_{ph} &= (h - h_0) - T_0(s - s_0), \\ \dot{e}x &= \dot{e}x_{ph} + \dot{e}x_{ch}, \end{aligned} \quad (10)$$

where T is absolute temperature (K) and subscripts i and 0 refer to ambient conditions. The mixture chemical exergy is attained using the following relations [15]:

$$ex_{mix}^{ch} = \left[\sum_{i=1}^n X_i ex_i^{ch} + RT_0 \sum_{i=1}^n X_i \ln X_i \right]. \quad (11)$$

The following relation is used to compute fuel exergy [14]:

$$\xi = \frac{ex_f}{LHV_f}. \quad (12)$$

to another heat generator (such as steam boiler in separate generation), and using the clean fuels such as natural gas are considered the essential factors in decreasing pollution produced by these systems. The environmental benefits of combined power and heat systems use less fuel with higher efficiency, consequently leading to less air pollution. Combustion process in a gas turbine occurs with generating large amount of extra air, since the obtained output power highly depends on the mass flow of the turbine. Gas turbine is among the least pollutant fossil fuel consuming equipment in power generation. The main pollutants of the gas turbines are nitrogen oxides, carbon monoxide, and carbon dioxide. The generated nitrogen oxide (gr per kg of the fuel) from combustion chamber is obtained using the following equation [13]:

$$m_{\text{NO}_x} = \frac{0.15 \times 10^{16} \tau^{0.5} \exp(-71100/T_{\text{PZ}})}{P_3^{0.05} (\Delta P_3/P_3)^{0.5}}, \quad (14)$$

$$m_{\text{CO}} = \frac{0.179 \times 10^9 \exp(7800/T_{\text{PZ}})}{P_3^2 \tau (\Delta P_3/P_3)^{0.5}}.$$

Here τ is the residence time in the combustion zone (assumed constant here at 0.002 s), T_{PZ} is the primary zone combustion temperature, P_3 is the combustor inlet pressure, and $\Delta P_3/P_3$ is the nondimensional pressure drop in the combustion chamber [13]. Using the equation of combustion as well as obtained values for the nitrogen oxides and carbon monoxide, the amount of carbon dioxide emission will be achieved.

5. Results and Discussion

Figure 2 presents the charts of energy efficiency, exergy efficiency, and the amount of carbon dioxide emissions per unit of output power for the gas turbine, CHP, and CCHP cycles. It is known that the levels of energy efficiency and exergy efficiency increase with the promotion of gas turbine cycle to CHP and CCHP cycles but the amount of carbon dioxide emissions per unit of output power declines. Increase of CCHP cycle's energy efficiency is much more than its exergy efficiency, because the exergy flow rate of heat transfer is less than the heat rate. In Figure 3, exergy loss is plotted for each of the components of the cycle. According to the chart it is determined that the combustion chamber has the highest rate of irreversibility among other components, and this is due to the chemical reactions taken place in the combustion chamber as well as a large temperature difference between the working fluid and the flame. After combustion chamber, recovery boiler has the most exergy loss.

5.1. Effect of Varying Compressor Pressure Ratio. According to Figure 4, the exergy efficiency for the CCHP cycle is first increased and then decreased. Initially, due to the increased inlet temperature to the combustion chamber and the reduction of the input fuel, efficiency increases. But at a certain pressure ratio, compressor work rate will exceed the fuel reduction rate and leads to reduced exergy efficiency. Figure 5 investigates the changes in the amount of carbon dioxide per unit of output power (including electricity, heat,

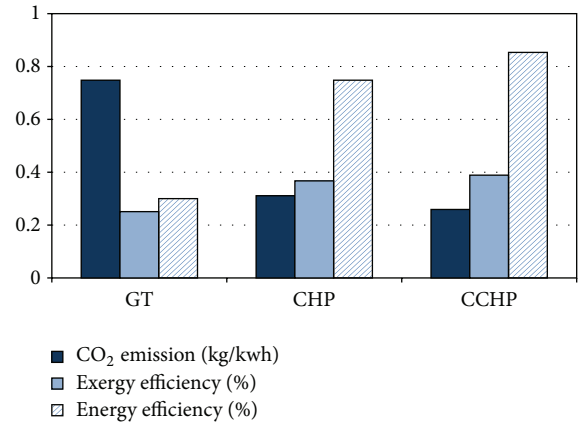


FIGURE 2: Energy efficiency, exergy efficiency, and normalized CO₂ emission for CCHP, CHP, and gas turbine cycles.

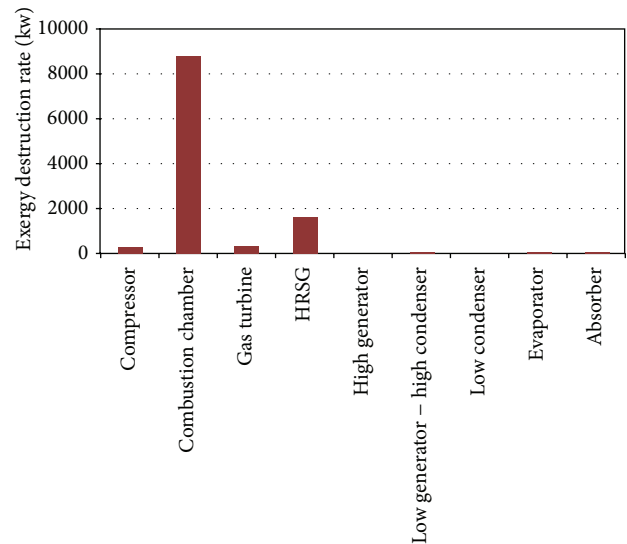


FIGURE 3: Exergy destruction rate for each component of the system.

and cold) compared to the increased compressor pressure. It is observed that, with increasing the pressure ratio of compressor in the desired trigeneration system, the amount of carbon dioxide emissions per unit of output increases, which is due to decrease of heat energy obtained from the recovery boiler.

5.2. Effect of Varying Gas Turbine Inlet Temperature. Gas turbine inlet temperature is one of the most important decision-making parameters in the trigeneration system on the basis of gas turbine. The increase of this temperature can increase the net output of work. Energy balance of the combustion chamber shows that the increase of inlet temperature to the gas turbine will increase the input fuel. As it can be observed in Figure 6, with the increase of inlet temperature to gas turbine, the exergy efficiency of cogeneration cycle will increase. This increase is due to the fact that an increase in the gas turbine inlet temperature will lead to the fact that the rate of network increase in gas

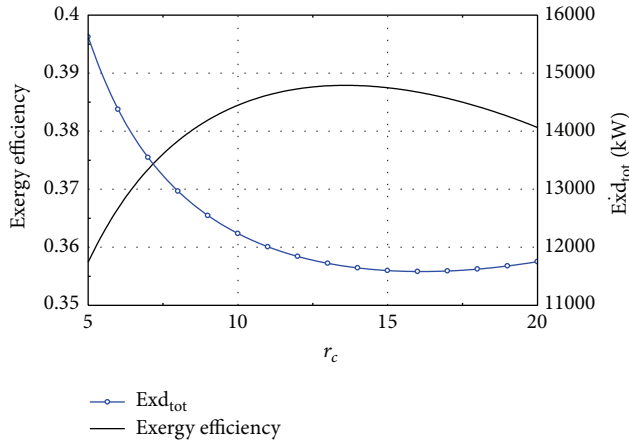


FIGURE 4: Variation with compressor pressure ratio of exergy efficiency and total exergy destruction rate.

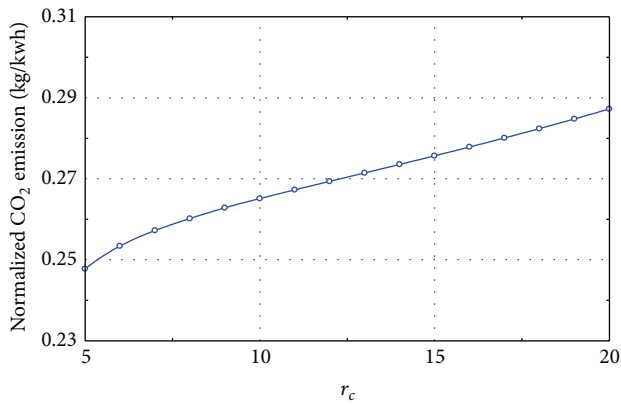


FIGURE 5: Variation with compressor pressure ratio of normalized CO₂ emission.

turbine exceeds the rate of the increased generated heat in the combustion chamber. This increase is because of the fact that, with increasing gas turbine inlet temperature, the rate of network increase of gas turbine exceeds the rate of increase in the amount of heat generated in the combustion chamber. In addition, according to Figure 6, the carbon dioxide emissions per unit of output power are reduced.

5.3. Effect of Varying Gas Turbine Isentropic Efficiency. The isentropic efficiency of the gas turbine is among the important parameters of the design and is indicative of how far the gas turbine performance is from a reversible process. As shown in Figure 7, by increasing the isentropic efficiency of gas turbine, the exergy efficiency of the cycle increases and its exergy loss is reduced.

5.4. Effect of Varying Absorption Generator Temperature. The temperature of the generator in the double-effect absorption chiller is indeed similar to the temperature of the saturated vapor exhausted from the recovery boilers and is related to the recovery boiler pressure. Boiler steam pressure recovery

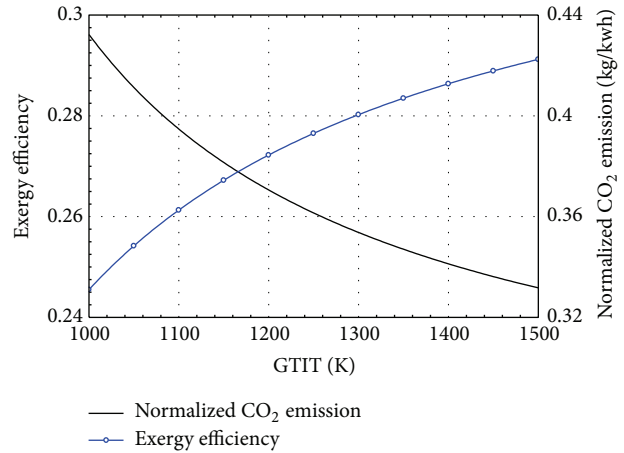


FIGURE 6: Variation with gas turbine inlet temperature of exergy efficiency and normalized CO₂ emission.

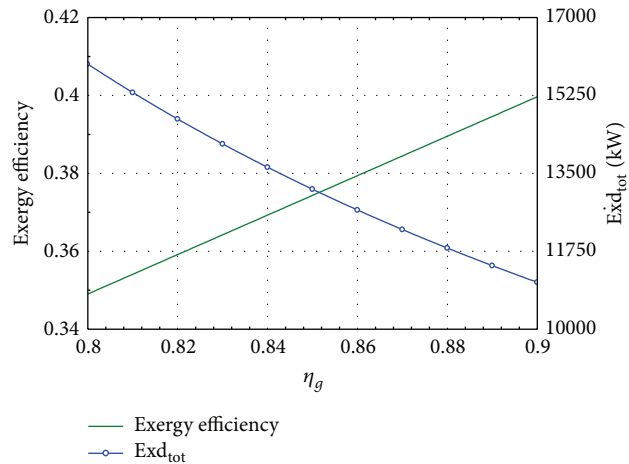


FIGURE 7: Variation with gas turbine isentropic efficiency of exergy efficiency and total exergy destruction rate.

is one of the important design parameters. By increasing the temperature of the exhausting saturated vapors from the recovery boilers, the amount of heat from the recovery boiler is reduced. And the cooling rate of absorption chiller increases. But the rate increase of absorption chiller cooling is much smaller than the rate of heat recovery boiler. Thus, as it can be seen in Figure 8, the exergy efficiency increases with increase of saturated steam temperature, because the exergy related to heat obtained from the recovery boiler and the exergy of cooling in the absorption chiller increase due to increase of saturated steam temperature. The coefficient of performance (COP) for the absorption chiller is achieved through dividing the cooling obtained from evaporator by the heat consumed in the generator. Hence, by increasing the absorption chiller generator temperature, the amount of heat used in the generator reduces and the cooling produced from the chiller evaporator increases; as shown in Figure 9, the performance ratio of chiller improves.

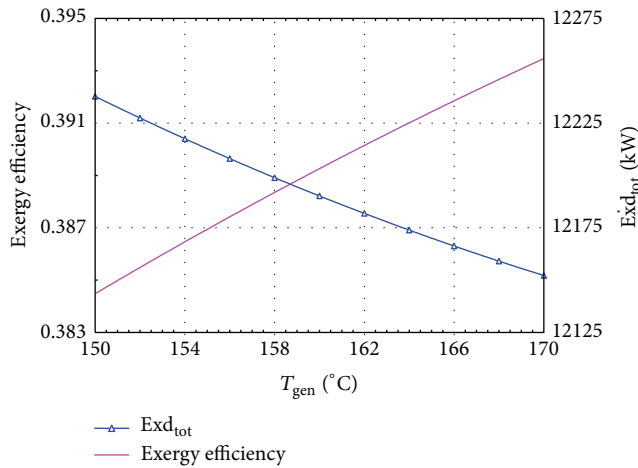


FIGURE 8: Variation with absorption generator temperature of exergy efficiency and total exergy destruction rate.

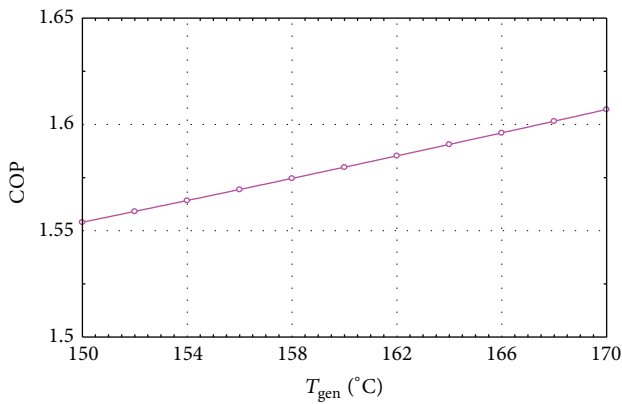


FIGURE 9: Variation with absorption generator temperature of absorption chiller COP.

6. Conclusions

A comprehensive thermodynamic modeling was carried out for a tri-generation system based on a double-effect absorption chiller. This study shed light on the importance of integrated energy system in order to achieve higher exergy efficiency and lower emission compared to single generation energy systems. Exergy analysis showed that the combustion chamber and the heat recovery boiler have the most exergy destruction compared to other components. This is mainly due to the large temperature difference for the heat transfer in both listed components and the combustion reaction in the combustion chamber. System performance significantly is affected by changes in pressure ratio compressor, inlet temperature to gas turbine, and isentropic efficiency of the high-temperature generator. According to the figures obtained from the previous section, the following conclusions can be listed:

- (i) Exergy efficiency of the CCHP cycle is more than CHP and gas turbines cycles.

- (ii) Exergy loss in the absorption chiller is less than other CCHP components.
- (iii) With the increase in compressor pressure ratio, exergy efficiency for the entire CCHP cycle is first increased and then decreased and emissions of carbon dioxide increase as well.
- (iv) Exergy efficiency of the CCHP cycle increases with the increase of gas turbine isentropic efficiency.
- (v) CCHP cycle produces less carbon dioxide per unit output power compared to CHP and gas turbine cycles.
- (vi) Exergy efficiency of the CCHP, CHP, and gas turbine cycles increases with the increasing of the gas turbine inlet temperature.
- (vii) Exergy loss of the CCHP cycle decreases with increasing the high-temperature absorption chiller temperature, but its exergy efficiency increases in this process.

Nomenclature

C_p :	Specific heat at constant pressure (kJ/kg K)
ex :	Specific exergy flow (kJ/kg)
$\dot{E}x$:	Exergy flow rate (kW)
$\dot{E}x_D$:	Exergy destruction rate (kW)
h :	Specific enthalpy (kJ/kg)
LHV:	Lower heating value (kJ/kg)
\dot{m} :	Mass flow rate (kg/s)
P :	Pressure (bar)
ΔP :	Pressure drop (bar)
\dot{Q} :	Heat rate (kW)
R :	Gas constant (kJ/kg K)
s :	Specific entropy (kJ/kg K)
T :	Temperature (K)
\dot{W} :	Work rate (kW)
AP:	Approach point
CHP:	Combined heat and power
HTC:	High temperature condenser
HTG:	High temperature generator
SHE:	Solution heat exchanger
LTC:	Low temperature condenser
LTG:	Low temperature generator
ABS:	Absorber
ECO:	Economizer
EVP:	Evaporator
HRSG:	Heat recovery steam generator
PP:	Pinch point.

Greek Symbols

γ : Specific heat ratio.

Subscripts

C:	Compressor
CC:	Combustion chamber
D:	Destruction

ex: Exergy
 f: Fuel
 g: Combustion gases
 GT: Gas turbine
 i: Inlet condition.

Superscript

ch: Chemical rate.

Competing Interests

The author declares that there are no competing interests.

References

- [1] F. A. Al-Sulaiman, I. Dincer, and F. Hamdullahpur, "Exergy analysis of an integrated solid oxide fuel cell and organic Rankine cycle for cooling, heating and power production," *Journal of Power Sources*, vol. 195, no. 8, pp. 2346–2354, 2010.
- [2] V. Havelský, "Energetic efficiency of cogeneration systems for combined heat, cold and power production," *International Journal of Refrigeration*, vol. 22, no. 6, pp. 479–485, 1999.
- [3] V. Athanasovici, O. Le Corre, G. Brecq, and M. Tazerout, "Thermoeconomic analysis method for cogeneration plants," in *Proceedings of ECOS Netherlands*, pp. 157–164, 2000.
- [4] E. Minciuc, O. Le Corre, V. Athanasovici, M. Tazerout, and I. Bitir, "Thermodynamic analysis of tri-generation with absorption chilling machine," *Applied Thermal Engineering*, vol. 23, no. 11, pp. 1391–1405, 2003.
- [5] P. K. Sahoo, "Exergoeconomic analysis and optimization of a cogeneration system using evolutionary programming," *Applied Thermal Engineering*, vol. 28, no. 13, pp. 1580–1588, 2008.
- [6] A. Huicochea, W. Rivera, G. Gutiérrez-Urueta, J. C. Bruno, and A. Coronas, "Thermodynamic analysis of a trigeneration system consisting of a micro gas turbine and a double effect absorption chiller," *Applied Thermal Engineering*, vol. 31, no. 16, pp. 3347–3353, 2011.
- [7] P. Ahmadi, M. A. Rosen, and I. Dincer, "Greenhouse gas emission and exergo-environmental analyses of a trigeneration energy system," *International Journal of Greenhouse Gas Control*, vol. 5, no. 6, pp. 1540–1549, 2011.
- [8] F. A. Al-Sulaiman, I. Dincer, and F. Hamdullahpur, "Energy analysis of a trigeneration plant based on solid oxide fuel cell and organic Rankine cycle," *International Journal of Hydrogen Energy*, vol. 35, no. 10, pp. 5104–5113, 2010.
- [9] Z. Amrollahi, I. S. Ertesvåg, and O. Bolland, "Thermodynamic analysis on post-combustion CO₂ capture of natural-gas-fired power plant," *International Journal of Greenhouse Gas Control*, vol. 5, no. 3, pp. 422–426, 2011.
- [10] B. Rezaie and M. A. Rosen, "District heating and cooling: review of technology and potential enhancements," *Applied Energy*, vol. 93, pp. 2–10, 2012.
- [11] H. Kurt, Z. Recebli, and E. Gedik, "Performance analysis of open cycle gas turbines," *International Journal of Energy Research*, vol. 33, no. 3, pp. 285–294, 2009.
- [12] I. Dincer and M. A. Rosen, "Energy, environment and sustainable development," *Applied Energy*, vol. 64, no. 1–4, pp. 427–440, 1999.
- [13] P. Ahmadi and I. Dincer, "Exergoenvironmental analysis and optimization of a cogeneration plant system using Multimodal Genetic Algorithm (MGA)," *Energy*, vol. 35, no. 12, pp. 5161–5172, 2010.
- [14] A. Mousafarash and P. Ahmadi, "Exergy and exergo-economic based analysis of a gas turbine power generation system," in *Progress in Exergy, Energy and the Environment*, chapter 7, Springer, 2014.
- [15] A. Bejan, G. Tsatsaronis, and M. Moran, *Thermal Design and Optimization*, John Wiley & Sons, New York, NY, USA, 1996.

Research Article

Exergy and Environmental Impact Assessment between Solar Powered Gas Turbine and Conventional Gas Turbine Power Plant

Ali Rajaei,¹ Hasan Barzegar Avval,² and Elmira Eslami¹

¹Power and Water University of Technology, Tehran, Iran

²Energy Optimization Research and Development Group (EORDG), Tehran, Iran

Correspondence should be addressed to Ali Rajaei; alirajaei10@gmail.com

Received 17 December 2015; Revised 12 April 2016; Accepted 14 April 2016

Academic Editor: Halil S. Hamut

Copyright © 2016 Ali Rajaei et al. This is an open access article distributed under the Creative Commons Attribution License, which permits unrestricted use, distribution, and reproduction in any medium, provided the original work is properly cited.

Recuperator is a heat exchanger that is used in gas turbine power plants to recover energy from outlet hot gases to heat up the air entering the combustion chamber. Similarly, the combustion chamber inlet air can be heated up to temperatures up to 1000 (°C) by solar power tower (SPT) as a renewable and environmentally benign energy source. In this study, comprehensive comparison between these two systems in terms of energy, exergy, and environmental impacts is carried out. Thermodynamic simulation of both cycles is conducted using a developed program in MATLAB environment. Exergetic performances of both cycles and their emissions are compared and parametric study is carried out. A new parameter (renewable factor) is proposed to evaluate resources quality and measure how green an exergy loss or destruction or a system as a whole is. Nonrenewable exergy destruction and loss are reduced compared to GT with recuperator cycle by 34.89% and 47.41%, respectively. Reductions in CO₂, NO_x, and CO compared to GT with recuperator cycle by 49.92%, 66.14%, and 39.77%, respectively, are in line with renewable factor value of around 55.7 which proves the ability of the proposed green measure to evaluate and compare the cycles performances.

1. Introduction

Recuperation as one of the conventional optimization enhancements in gas turbine cycles by preheating inlet air entering combustor which decreases fuel consumption rate dramatically leads to less greenhouse gas emissions. The other way refers to hybridizing gas cycle with solar power. Advantages of combining solar thermal power with power generation systems are reviewed by Jamel et al. [1]. Renewable sources integration with power cycles with the aim of increasing total exergy efficiency based on different scenarios is performed by them.

Several studies are conducted on energy and exergy analysis of hybrid solar gas cycles [2]. Solar power tower as a central receiver system recently has been built in both demonstrational and commercial projects all over the world [3]. Schwarzbözl et al. [4] using advanced software tools carried out design optimization and performance prediction of

the solar tower gas turbine power plants. Their project proved feasibility of solar tower integration with conventional gas turbine power plant. It is proved that hybrid solar gas turbine cycles are more efficient in terms of CO₂ emission prevention compared to conventional gas cycle with recuperator.

Comparing energy systems often is performed through measuring environmental characteristics and performance in terms of energy and exergy analysis [2]. Thermodynamic modeling, second-law based thermodynamic analysis, and multiobjective optimization of a gas turbine power plant with and without recuperator are conducted [5, 6].

In this paper, two scenarios are defined based on different heat sources to preheat the air inlet to combustor. First is a conventional gas turbine cycle with recuperator and the second is a solar power tower coupled with a gas turbine where central receiver plays the same role as the recuperator. In order to find inefficiencies in both cycles, exergy analysis is performed by simulating the cycles using MATLAB program.

Exergoenvironmental analysis tool by predicting emissions rate helps designing a more sustainable cycle. Environmental impacts including CO₂, NO_x, and CO are measured through the developed code. SO_x which is prevented by pre-operations in all gas cycles is considered negligible in modeling.

This analysis is aimed at quantitatively addressing the impact of renewable and nonrenewable sources on environment by introducing renewable factor. In research studies to the authors' knowledge, all sources are considered the same. Losses and destructions from various sources are equivalent in common exergy analysis. However, losses and destructions from renewable resources are different from nonrenewable resources since all exergy flows have impacts on environment. In the present work, a new measure is introduced and renewable and nonrenewable loss and destructions are calculated to show the real effect of using renewable resources in environmental impacts reduction.

The Present study highlights exergy and exergoenvironmental analysis of both mentioned cycles by measuring their exergy destructions throughout the cycle and comparing their total exergy efficiencies in order to reach a better insight:

- (i) To model a new arrangement of new hybrid gas cycle.
- (ii) To conduct exergy and exergoenvironmental analysis in order to find inefficiencies.
- (iii) To propose renewable factor which helps in comparing renewable and nonrenewable sources quantitatively and more accurately.

2. System Description and Assumptions

In this research paper, two scenarios are presented. The first one includes heliostat solar field, central receiver, and power generation system while the second one comprises a recuperator instead of prime solar system.

Figure 1(a) demonstrates SPT cycle designed similarly based on SOLGATE project cycle [4] in which the solar hybrid gas turbine system functions by first concentrating solar energy from a heliostat field (solar field) to a receiver mounted on top of a tower acting as a convective/radiative heat exchanger. These irradiations are converted into heat absorbed by the air coming from compressor. Preheated air enters combustor in order to be mixed with the fuel where the combustion chamber closes the temperature gap between the receiver outlet temperature (800–1000°C at design point) and the turbine inlet temperature (950–1300°C) and provides constant turbine inlet conditions despite fluctuating solar input. The solar power tower technology is used with concentration ratios up to 1000 suns to achieve the high receiver temperatures. More detailed information about the receiver development and test results with receiver temperatures up to 960°C can be found in [7].

To model and compare two cycles, thermodynamic modeling of both systems is carried out. Systems are analyzed at their design point using provided data and average yearly DNI for solar system. Then exergy analysis and emission calculations are carried out and systems' performances are compared.

In the second scenario recuperator is used as a replacement of mentioned solar part in first cycle. Several assumptions are made in order to render the analyses in a traceable way considered to model the cycles in the present study which are listed below:

- (1) All the processes are assumed to work under steady-state condition.
- (2) Combustion products and air stream are considered ideal gas.
- (3) Natural gas enters combustor as fuel.
- (4) Dead state is $P_0 = 1.01$ bar and $T_0 = 293.15$ K.

3. Formulation

The present study performed exergy and exergoenvironmental analysis both on each cycle where in the first one solar receiver, as external source, and in the second one recuperator, as internal source, are considered.

3.1. Recuperator. The energy balance equation for recuperator which is shown in Figure 1 is as follows:

$$\dot{m}_{\text{air}}(h_3 - h_2) = \dot{m}(h_5 - h_6)\eta_{\text{recup}}. \quad (1)$$

Recuperator efficiency is usually 95–97% and in many cases is considered 100%. Here 97% percent is assumed based on an average value in similar GT cycles [5]:

$$\frac{P_3}{P_2} = (1 - \Delta P_{\text{recup}}), \quad (2)$$

where pressure drop through the recuperator is considered 3% of the inlet pressure for both flow streams and through the combustion chamber is 3% of the inlet pressure [5].

3.2. Solar System. As shown in Figure 1, central receiver has two input streams, solar irradiations and compressed air which gets warmer by absorbing the heat coming from solar rays. In this analysis \dot{Q} is the transferred heat rate as

$$\dot{Q} = \frac{H_{\text{out}} - H_{\text{in}}}{\eta_{\text{rec}}}, \quad (3)$$

where H_{out} and H_{in} are outlet and inlet stream enthalpy:

$$\dot{Q}_{\text{rec}} = \dot{Q} * \dot{m}_{\text{air}}, \quad (4)$$

$$\text{Solar share} = \frac{\dot{Q}_{\text{rec}}}{\dot{m}_F * \text{LHV} + \dot{Q}_{\text{rec}}}.$$

Solar share shows renewable heat source contribution into conventional fossil fuel cycles and is defined as below:

$$\text{Solar share} = \frac{\dot{Q}_{\text{rec}}}{\dot{Q}_{\text{natural gas}} + \dot{Q}_{\text{rec}}} * 100, \quad (5)$$

where $\dot{Q}_{\text{natural gas}}$ is the supplied heat by fuel:

$$\dot{Q}_{\text{natural gas}} = \dot{m}_F \text{LHV}. \quad (6)$$

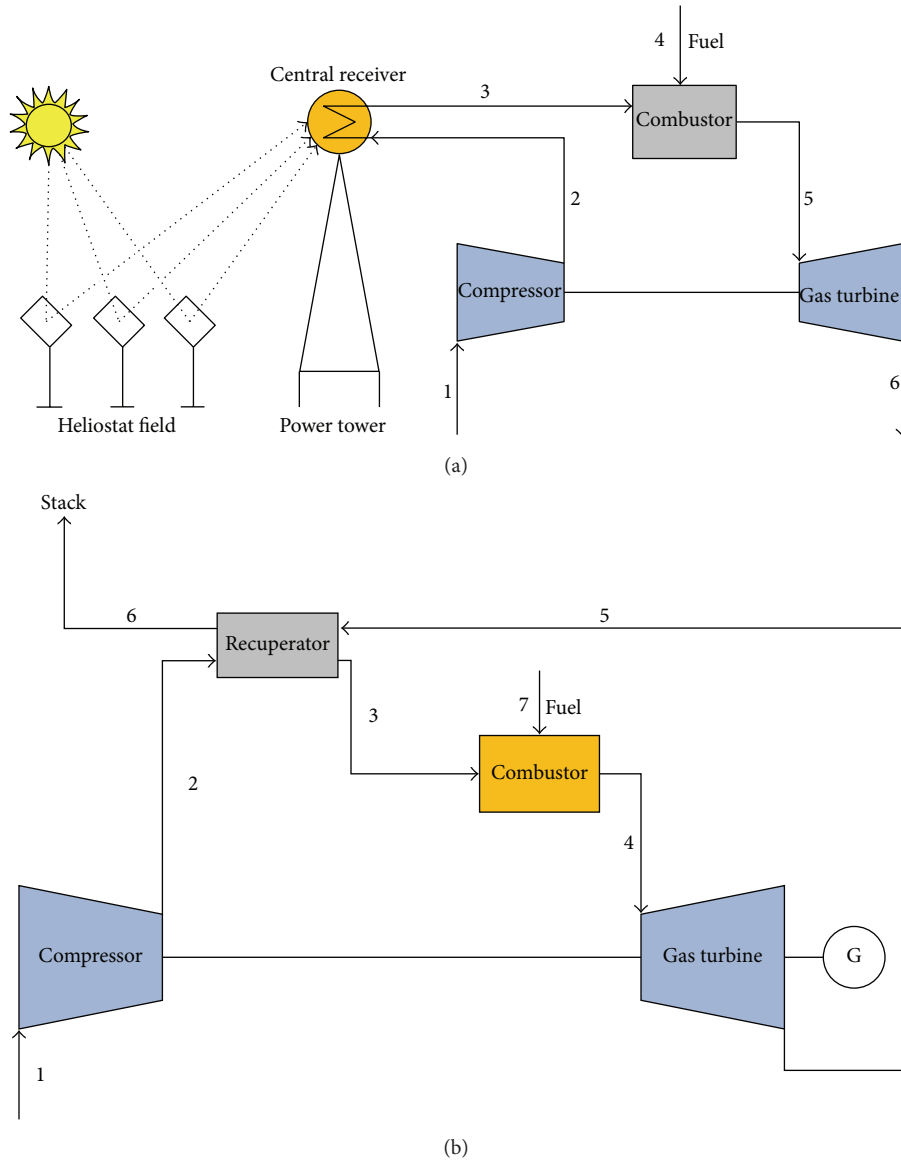


FIGURE 1: Schematic diagram of (a) GT-solar cycle and (b) GT-recuperator cycle.

And \dot{Q}_{rec} is the heat released from irradiations into central receiver:

$$\dot{Q}_{rec} = \eta_{field} \eta_{rec} \dot{Q}_{sol, total} \quad (7)$$

One can write

$$\dot{Q}_{sol, total} = A * DNI. \quad (8)$$

DNI is defined as direct normal irradiance which varies related to the geographical situation and a constant annual average value for a certain location is assumed.

3.3. Exergy Analysis. Exergy analysis is a powerful tool in referring exergy destructions in a power cycle while these wastes cannot be seen through energy analysis [8].

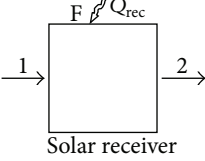
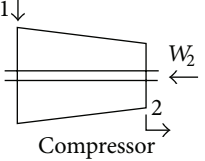
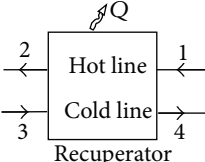
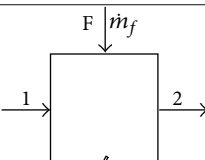
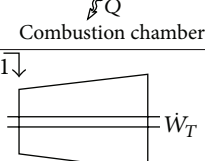
It is worth mentioning that four concepts are demonstrated in the present study. Ex_F and Ex_P are the fuel and product exergy rate, respectively, and also the exergy loss (Ex_L) is defined as the useful exergy which is wasted to the environment with no converting to the work and exergy destruction (Ex_D) due to irreversibilities.

To find the appropriate relation between these concepts, one may write

$$Ex_F = Ex_P + Ex_D. \quad (9)$$

This should be written for all components as shown schematically in Table 1 to calculate the exergy balance in each of them. Considering if the component is assumed adiabatic, the exergy loss would be zero.

TABLE 1: Components exergy balance.

Component	Ex_F	Ex_P	Ex_D
 Solar receiver	$Ex_1 + \frac{Q_{rec}}{\eta_{field}} \left(1 - \frac{T_0}{T_{sun}}\right)$	Ex_2	$Ex_D = Ex_F - Ex_P - Q \left(1 - \frac{T_{sun}}{T_0}\right)$ $Ex_{loss} = Q \left(1 - \frac{T}{T_0}\right)$ $\eta_{ex} = \frac{Ex_P}{Ex_F}$
 Compressor	$Ex_1 + W_2$	Ex_2	$Ex_D = Ex_2 - Ex_1 - W_2$ $\eta_{ex} = \frac{Ex_2}{Ex_1 + W_2}$
 Recuperator	$Ex_1 - Ex_2$	$Ex_4 - Ex_1$	$Ex_D = Ex_F - Ex_P = Q \left(1 - \frac{T}{T_0}\right)$ $\eta_{ex} = \frac{Ex_P}{Ex_F}$
 Combustion chamber	$Ex_F + Ex_1$	Ex_2	$Ex_D = Ex_F - Ex_P - Q \left(1 - \frac{T}{T_0}\right)$ $Ex_{loss} = Q \left(1 - \frac{T}{T_0}\right)$ $\eta_{ex} = \frac{Ex_P}{Ex_F}$
 Gas turbine	$Ex_1 - Ex_2$	\dot{W}_T	$Ex_D = Ex_1 + Ex_2 - \dot{W}_T$ $\eta_{ex} = \frac{\dot{W}_T}{Ex_1 + Ex_2}$

In this research study, input exergy is supplied from two different sources shown in Figure 1. The solar input exergy is defined as below:

$$Ex_{sol} = \frac{Q_{rec}}{\eta_{field}} \left(1 - \frac{T_0}{T_{sun}}\right). \quad (10)$$

3.4. Exergoenvironmental Analysis. Although many studies in the literature are conducted based on integration methods between solar power and conventional power plants which mainly are focused on energy and exergy analysis, there is no attention to environmental issues. The present study highlights greenhouse gas emissions reduction through exergoenvironmental analysis which is conducted on both scenarios. It is considered that CO and NO_x are pollutant emissions in grams per kilogram. The appropriate equations for these pollutants are as follows [9]:

$$\dot{m}_{NO_x} = \frac{0.15E16\tau^{0.5} \exp(-71100/T_{pz})}{P_3^{0.05} (\Delta P_3/P_3)}, \quad (11)$$

$$\dot{m}_{CO} = \frac{0.179E99 \exp(7800/T_{pz})}{P_3^2 \tau (\Delta P_3/P_3)},$$

where τ is the residence time in combustion zone (it is assumed constant and is equal to 0.002 s), T_{pz} is the primary zone combustion temperature, P_3 is the combustor inlet pressure, and $\Delta P_3/P_3$ is the nondimensional pressure drop in the combustion chamber.

Accordingly CO₂ is calculated as below [6]:

$$\varepsilon = \frac{\dot{m}_{CO_2}}{\dot{W}_{net}}. \quad (12)$$

4. Results and Discussion

4.1. Single GT, GT-Recuperator, and GT-Solar Performance Comparison. In terms of exergy and environmental impacts, three mentioned cycles are compared. Exergy efficiency and CO₂ emission for three mentioned cycles are presented in Figure 2. Exergy efficiency for the GT-solar is the least and for the recuperator is the most. It is a clear result of efficiency definition and the vast difference between solar input exergy and fuel exergy. Solar exergy due to high temperature value of its resource is much higher in comparison to fuel exergy. However, solar energy implementation reduces the natural gas consumption rate dramatically and so the emission for this cycle is about half the size of the conventional cycles. Due

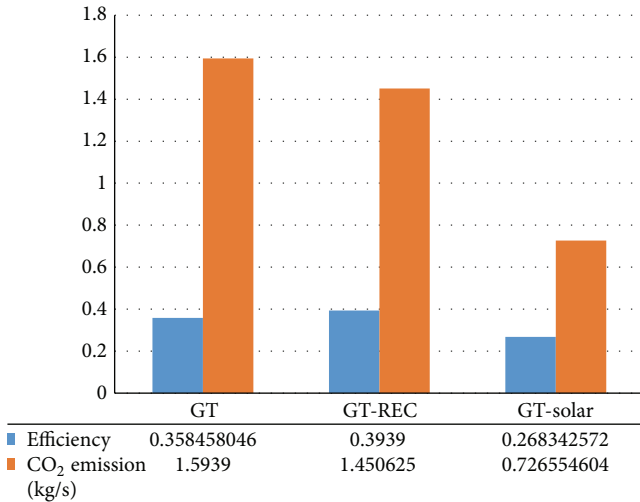


FIGURE 2: Efficiency-emission for different scenarios.

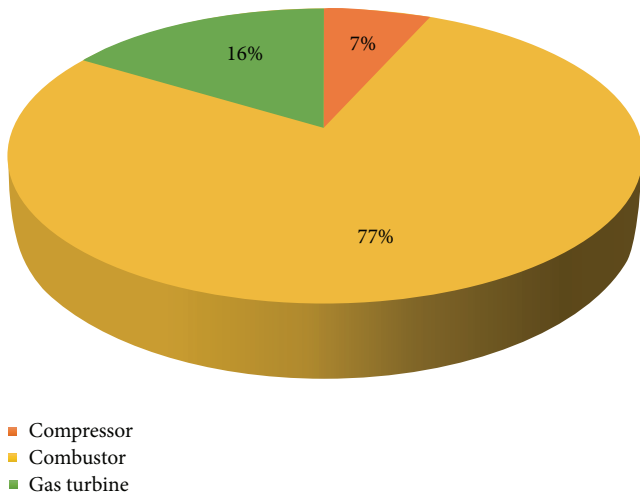


FIGURE 3: Exergy destruction distribution in GT cycle.

to higher efficiency in recuperator relative to single GT cycle, emission and fuel flow rate are lower. For cycle with single sources of exergy or energy, efficiency and CO₂ emission are often correlated inversely.

Exergy flow in these three different cycles shows similar behavior. In Figure 3 exergy destruction rates in single GT are shown. As it is presented combustor is the greatest exergy destructor by 77 percent of overall destruction rate. Similarly in GT-recuperator cycle, it is also presented the same trend.

67 percent of overall exergy destruction is related to combustor in GT-recuperator. 10 percent reduction in destruction is due to higher temperature inlet to the combustor which reduced the combustion rate. If we consider the recuperator as another internal source of exergy, the overall destruction rate in cycle resources is 71 percent in GT-recuperator cycle which is shown in Figure 4.

GT-solar has shown a similar trend by 71 percent of exergy destruction in solar part (from sun to air flow) and 23 percent in combustor. In fact 94 percent of exergy destruction

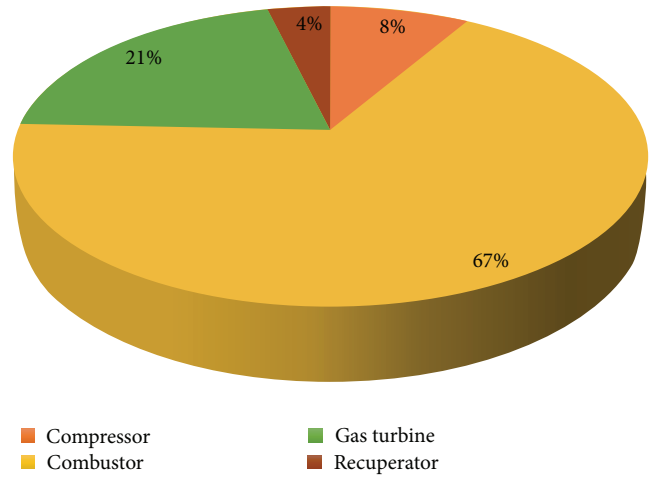


FIGURE 4: Exergy destruction distribution in GT-recuperator cycle.

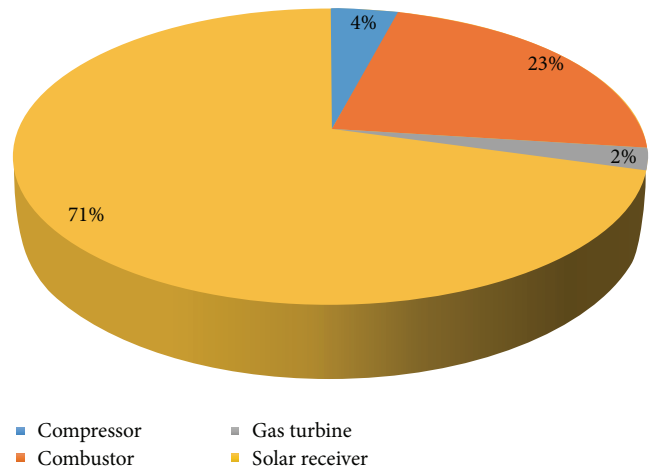


FIGURE 5: Total exergy destruction distribution in GT-solar cycle.

is related to exergy or energy resources conversion parts which has the highest value among other cycles. Figure 5 shows destruction distribution in GT-solar cycle.

Energy resources destruction percentages of total in three cycles are presented and compared in Figure 6 and show the same trend as exergy efficiency. So one may conclude that the cycle with the less exergy destruction in energy resources is the most efficient cycle.

4.2. *Renewable Resources versus Nonrenewable Resources.* In terms of exergy, GT-solar hybrid is the worst cycle. Exergy definition by itself does not provide an insight into the resources types.

The earth receives solar energy daily and continuously and it is absorbed, transformed, rejected, and stored in various types of energy or phenomena. On the other hand, fossil fuels are not energy resources on the planet except for human being. In fact what we are using as fossil fuels are out of the earth, usually ecology, and are the only human being impact or footprint on the environment. So any destruction

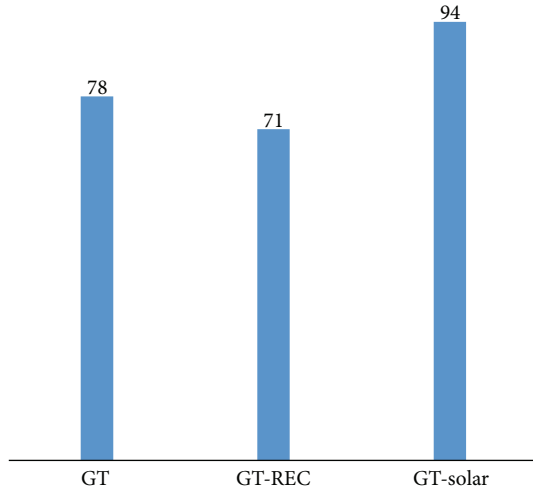


FIGURE 6: Contribution of exergy destruction in resource conversion components in different cycles.

or losses due to fossil fuels can be considered as pollution or impacts on environment.

Here, to give our resources a meaning in destruction, we define renewable and nonrenewable exergy destruction and losses. Exergy losses are important due to the fact that streams with exergy can potentially cause changes in environment because of their exergy. Both single GT and GT-recuperator cycles are purely nonrenewable. However, in GT-solar cycle sources are different. To calculate the renewable and nonrenewable exergy destruction and losses rates in GT-solar cycle, we use the following method.

Exergy comes from two different sources, sun and natural gas. We define resource distribution factor as follows:

$$f_{\text{renewable}} = \frac{(\Delta Ex_{\text{air}})_{\text{rec}}}{(\Delta Ex_{\text{air}})_{\text{rec}} + (\Delta Ex_{\text{flue gas}})_{\text{comb}}} \quad (13)$$

Then we assume that exergy of working fluid is the algebraic combination of various resources. Now we can provide the following equations for exergy destruction and losses:

$$\begin{aligned} (Ex_L)_{\text{non-renewable}} &= (1 - f_{\text{renewable}}) (Ex_L)_{\text{total}} \\ (Exd_i)_{\text{non-renewable}} &= (1 - f_{\text{renewable}_i}) (Exd_i)_{\text{total}} \end{aligned} \quad (14)$$

Furthermore, exergy destruction in solar system is considered purely renewable and destruction in combustor is considered purely nonrenewable. Implementing equations and definitions presented above, nonrenewable destruction distribution is presented in Figure 7.

Figure 8 shows the value of nonrenewable destruction and losses in different cycles. Implementing nonrenewable losses and destructions, the main advantage of the GT-solar cycle is quantitatively measured. Nonrenewable losses which are impacts of human beings activities on environment have their least value in GT-solar cycle.

GT-solar cycle parameters are summarized in Table 2. In this table, parameters like solar share, exergy inputs,

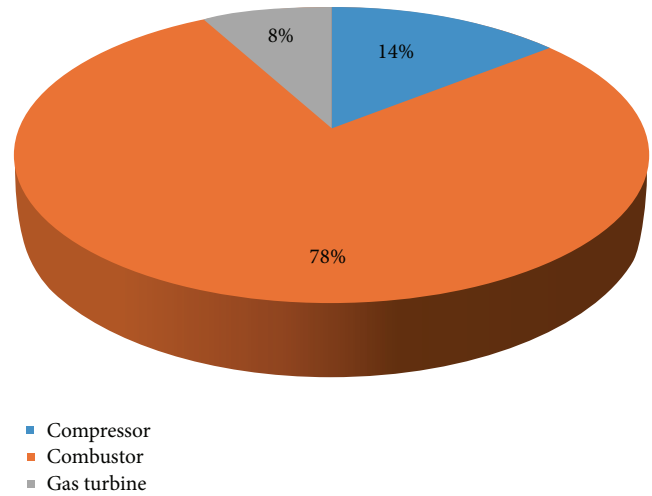


FIGURE 7: Nonrenewable exergy destruction distribution in GT-solar cycle (kW).

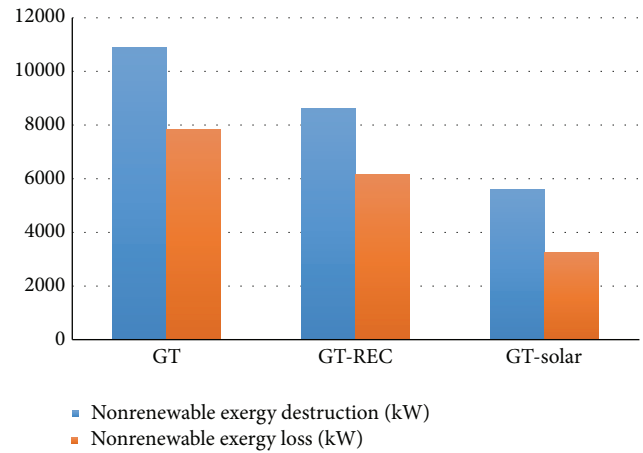


FIGURE 8: Nonrenewable exergy destruction and losses in different cycles.

efficiency, and destruction of different components are presented. Data are assumed based on project SOLGATE [4].

In addition to mentioned analysis, NO_x and CO emission are predicted for different cycles. Results are tabulated in Table 3. Due to lowest fuel flow rate in GT-solar cycle, emissions are lowest values. NO_x in GT-recuperator is higher than GT cycle because of higher combustor inlet temperature. CO emission shows an opposite trend.

5. Conclusions

Different cycles are presented and compared according to exergy and environmental analyzing tools. Although GT-solar cycle is the worst according to exergy analysis, its main advantages over other conventional cycles is highlighted when resource valued exergy analysis is used.

In addition, the above analysis shows that resource conversion processes are the most destructive ones in the cycle. Furthermore, the cycle exergy efficiency is directly correlated to resource destruction contribution in the cycle.

TABLE 2: Performance parameters of GT-solar cycle.

Parameter	Value
Pressure ratio	14
TIT (°C)	1080
η_{comp} (%)	0.835
η_{GT} (%)	0.93
Combustor inlet temperature (°C)	800
Receiver efficiency (%)	0.94
Field efficiency (%)	0.55
Receiver pressure drop	0.03
η_{recup} (%)	0.97
Exergy efficiencies	
Compressor (%)	0.93
Combustor (%)	0.86
Gas turbine (%)	0.97
Receiver (%)	0.41
Exergy destruction rates	
Compressor (kW)	908.53
Combustor (kW)	4973.28
Gas turbine (kW)	504.89
Receiver (kW)	15374.38
Overall cycle parameters	
Solar share (%)	0.56
$f_{\text{renewable}}$.557
Total exergy loss (kW)	7310
Total exergy efficiency (%)	0.268
Total exergy destruction (kW)	21761.09
Solar input exergy (kW)	26200
Fuel flow rate (kg/s)	0.264
Air flow rate (kg/s)	33.63
Predicted NO _x emission (kg/s)	1.27E - 10
Predicted CO emission (kg/s)	0.0108

TABLE 3: NO_x and CO emissions.

	NO _x (kg/s)	CO (kg/s)
GT	3.5478E - 10	0.02
GT-REC	3.7395E - 10	0.0179
GT-SOL	1.2663E - 10	0.0108

Total exergy destruction in GT-solar cycle is higher than other cycles. However, nonrenewable destruction is the lowest for GT-solar among different scenarios. As nonrenewable destructions and losses have significant impacts on the environment, the best advantage of renewable resources and hybrid GT-solar cycle is minimizing the impacts on the environment. NO_x, CO, and CO₂ emissions are also reduced significantly by using solar hybrid cycle.

Nomenclature

A: Area, m²
 DNI: Direct normal irradiance, W/m²
 ex: Specific exergy, kJ/kg

Ex: Exergy, kJ
 Exd: Exergy destruction, kJ
 f : Resource distribution factor
 GT-REC: Gas turbine cycle with recuperator
 GT-SOL: Gas turbine cycle with solar receiver
 h : Specific enthalpy, kJ/kg
 LHV: Lower heating value, kJ/kg
 \dot{m} : Mass flow rate, kg/h
 P : Pressure, bar
 \dot{Q} : Heat transfer, kJ/kg
 s : Specific entropy, kJ/kgK
 TIT: Turbine inlet temperature, °C
 T : Temperature, °C.

Greek Letters

ε : CO₂ emission per net output power, kgCO₂/MWh
 η : Efficiency
 η_{field} : Heliostat field efficiency
 η_{rec} : Receiver efficiency.

Subscripts

0: Dead state
 comb: Combustor
 comp: Compressor
 D: Destruction
 F: Fuel
 GT: Gas turbine
 i: Index
 in: Inlet
 L: Loss
 out: Outlet
 P: Product
 rec: Receiver
 recup: Recuperator
 sol: Solar.

Competing Interests

The authors declare that they have no competing interests.

References

- [1] M. S. Jamel, A. Abd Rahman, and A. H. Shamsuddin, "Advances in the integration of solar thermal energy with conventional and non-conventional power plants," *Renewable and Sustainable Energy Reviews*, vol. 20, pp. 71–81, 2013.
- [2] C. Xu, Z. Wang, X. Li, and F. Sun, "Energy and exergy analysis of solar power tower plants," *Applied Thermal Engineering*, vol. 31, no. 17–18, pp. 3904–3913, 2011.
- [3] O. Behar, A. Khellaf, and K. Mohammadi, "A review of studies on central receiver solar thermal power plants," *Renewable and Sustainable Energy Reviews*, vol. 23, pp. 12–39, 2013.
- [4] P. Schwarzbözl, R. Buck, C. Sugarmen et al., "Solar gas turbine systems: design, cost and perspectives," *Solar Energy*, vol. 80, no. 10, pp. 1231–1240, 2006.
- [5] P. Ahmadi and I. Dincer, "Thermodynamic and exergoenvironmental analyses, and multi-objective optimization of a gas

- turbine power plant,” *Applied Thermal Engineering*, vol. 31, no. 14-15, pp. 2529–2540, 2011.
- [6] P. Ahmadi, H. Barzegar Avval, A. R. Ghaffarizadeh, and M. H. Saidi, “Thermo-economic-environmental multiobjective optimization of a gas turbine power plant with preheater using evolutionary algorithm,” *International Journal of Energy Research*, vol. 35, no. 5, pp. 389–403, 2011.
- [7] P. Heller, M. Pfänder, T. Denk et al., “Test and evaluation of a solar powered gas turbine system,” *Solar Energy*, vol. 80, no. 10, pp. 1225–1230, 2006.
- [8] I. Dincer and M. A. Rosen, *Energy, Environment and Sustainable Development*, Elsevier, Amsterdam, The Netherlands, 2007.
- [9] N. K. Rizk and H. C. Mongia, “Semianalytical correlations for NO_x, CO, and UHC emissions,” *Journal of Engineering for Gas Turbines and Power*, vol. 115, no. 3, pp. 612–619, 1993.

Research Article

Performance Assessment of a Hybrid Solar-Geothermal Air Conditioning System for Residential Application: Energy, Exergy, and Sustainability Analysis

Yasser Abbasi, Ehsan Baniasadi, and Hossein Ahmadikia

Department of Mechanical Engineering, Faculty of Engineering, University of Isfahan, Hezar Jerib Avenue, Isfahan 81746-73441, Iran

Correspondence should be addressed to Ehsan Baniasadi; e.baniasadi@eng.ui.ac.ir

Received 4 December 2015; Revised 7 January 2016; Accepted 12 January 2016

Academic Editor: Pouria Ahmadi

Copyright © 2016 Yasser Abbasi et al. This is an open access article distributed under the Creative Commons Attribution License, which permits unrestricted use, distribution, and reproduction in any medium, provided the original work is properly cited.

This paper investigates the performance of a ground source heat pump that is coupled with a photovoltaic system to provide cooling and heating demands of a zero-energy residential building. Exergy and sustainability analyses have been conducted to evaluate the exergy destruction rate and SI of different compartments of the hybrid system. The effects of monthly thermal load variations on the performance of the hybrid system are investigated. The hybrid system consists of a vertical ground source heat exchanger, rooftop photovoltaic panels, and a heat pump cycle. Exergetic efficiency of the solar-geothermal heat pump system does not exceed 10 percent, and most exergy destruction takes place in photovoltaic panel, condenser, and evaporator. Although SI of PV system remains constant during a year, SI of GSHP varies depending on cooling and heating mode. The results also show that utilization of this hybrid system can reduce CO₂ emissions by almost 70 tons per year.

1. Introduction

The energy consumption for residential applications is almost one-third of the world's primary energy demand, while it is rapidly increasing due to population growth and improvement in human life standards [1, 2]. Currently most of the required energy in this sector is supplied by high-temperature sources to meet low-temperature heating needs. These energy crises besides environmental degradation of earth, global warming, and depletion of natural resources have encouraged researchers to investigate the possibility of using environmentally benign energy resources to drive low exergy systems, that is, solar systems, ground source heat exchangers, and so forth, with working temperatures close to environment temperature. Low exergy systems are basically air conditioning systems that utilize low grade energy of sustainable sources to provide heating and cooling effects at a temperature close to room temperature [3].

As a promising approach in energy conservation, heat pumps can be combined with renewable energy sources to provide a low exergy cooling and heating system. Among the

renewables, geothermal, wind, and solar are more adoptable to sustainable buildings. Most of the research and developments in renewable energy based systems for residential application are conducted to provide hot water, heating, cooling, and ventilation by heat pumps or vapor-power cycles [4–6]. Ground source heat pumps (GSHP), integrated with certain types of low-temperature distribution system, have been identified as the most efficient and ecofriendly heating and cooling technology for various climates. These systems are energy efficient and they are designed based on the relatively constant temperature of the ground to supply heating during the winter and cooling during the summer. Vertical closed-loop systems are the most efficient, though the most expensive, configuration because the subsoil level of temperature increases and stabilizes with depth [7–9]. Analyses of GSHP have been widely conducted in literature from energetic and exergetic points of view [10–13]. Integration of ground source heat pumps with photovoltaic system is a promising option to supply electricity, hot water, and heating and cooling effects for off-network communities and remote areas [14–16].

Combination of different renewable energy sources to meet the demands of a sustainable building is widely studied. Li et al. [17] described a rooftop hybrid heat pump system that uses wind and solar energy to provide hot water, heating, and cooling from energy, exergy, and environmental point of view. Mikati et al. overviewed a small-scale distributed power system that contains photovoltaic arrays, small-scale wind turbines, and an electric grid connection [18]. Dai et al. conducted an experimental study to evaluate the effect of operation modes on the heating performance of a solar assisted ground source heat pump system (SAGSHPS) [19]. Moreover, different concepts of solar assisted heat pump systems with ground heat exchanger are simulated according to IEA SHC Task44/HPP Annex38 reference conditions using TRNSYS software. The dependency of system efficiency on seasonal performance factor and possible shortening of the ground heat exchanger by minimum temperature at the ground heat exchanger inlet are evaluated [20]. The performance of a new system for cooling of solar PV panels called Ground-Coupled Central Panel Cooling System (GC-CPCS), which is in operation at the Energy Park of Rajiv Gandhi Proudyogiki Vishwavidyalaya (RGPV), is studied by Sahay et al. [21]. Exergy analysis of photovoltaic system has been conducted broadly. Sobhnamayan et al. [22] have investigated an optimized solar photovoltaic thermal (PV/T) water collector based on exergy concept. Exergy analyses of photovoltaic (PV) and photovoltaic/thermal (PV/T) systems were presented by Saloux et al. [23]. Gholampour et al. [24] have evaluated the performance of the PV/UTC and UTC systems by introducing energy efficiency as a function of electrical-to-thermal ratio number and also the second law efficiency. Exergy and economic evaluation of thermal photovoltaic (PV/T) water based collectors for different climates in Iran have been conducted by Jahromi et al. [25].

In this study an exergy analysis is conducted to investigate the performance of an integrated PV-GSHP system for space heating and cooling of a remote building. A general arrangement schematic view of the system is illustrated in Figure 1. The required area of SPV panels and GSHP needed length are calculated for the hybrid air conditioning system of a 200 m² building in a remote area. The effect of different climates on system performance is investigated based on the meteorological data of three cities of Iran (Isfahan, Yazd, and Shahrekord). It is assumed that the building structure is identical for all climate case studies; however the cooling and heating loads, solar irradiation, and ground depth temperature are different. The analysis is based on the monthly averaged energy demands of the building. It is assumed that heat and electricity can be stored during daytime. An energy, exergy, and sustainability analysis is conducted to evaluate the feasibility of utilizing solar assisted ground source heat pump (GSHP) for air conditioning purposes.

2. System Analysis

2.1. Heating and Cooling Load. A remote building with 200 m² area located in Isfahan (elevation: 1590 m) is considered to study the performance of an integrated geothermal heat pump and photovoltaic system that provides heating and

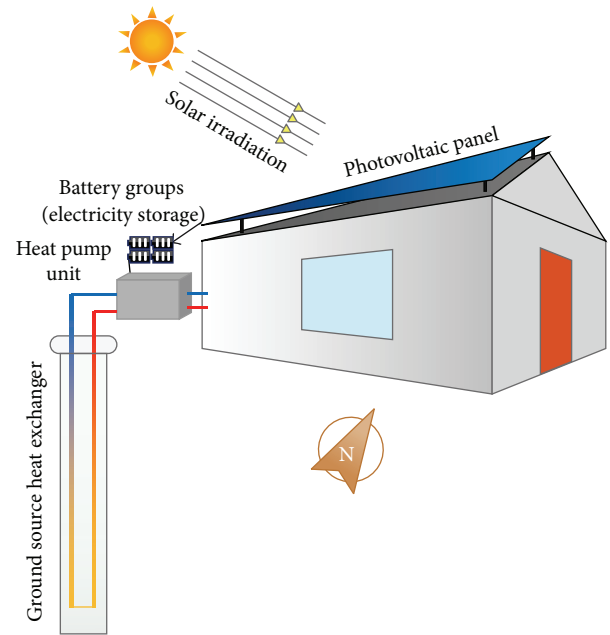


FIGURE 1: Schematic view of the solar assisted GSHP air conditioning system.

cooling loads. The system performances are compared for different cities of Iran including Yazd (elevation: 1216 m) and Shahrekord (elevation: 2061 m). Figure 1 shows a schematic view of the residential building and the solar assisted geothermal heat pump. The heating, cooling, and hot water demands of the building are calculated based on outdoor design conditions of each city on an hourly basis.

2.2. System Description. Figure 3 shows a flow diagram of the integrated solar assisted GSHP system that operates as an off-grid energy system for the specified residential building. It consists of three main loops.

- (1) The ground loop delivers heat energy (in cooling mode) to ground sublayers or takes heat energy (in heating mode) from the ground. A circulating pump circulates water, as a working fluid, in the loop (stream 1). Heat is exchanged with the ground via a network of n number of GSHXs with overall efficiency of $\eta_{g,x}$. The ground temperature T_g is almost constant during a year.
- (2) The primary loop is basically a Rankin refrigeration cycle that consists of two heat exchangers with exchangeable functions depending on cooling or heating season. In heating mode the first heat exchanger takes heat from the ground loop as an evaporator, while the other heat exchanger delivers heat to the secondary loop as a condenser. In cooling mode the first heat exchanger delivers heat to the ground loop as a condenser and the other extracts heat from the secondary loop as an evaporator. A compressor pressurizes refrigerant R-134a in the primary loop. A 4-way valve is adopted to switch

cooling and heating mode functions by reversing the refrigerant flow direction.

- (3) The secondary loop exchanges heat via a fan-coil heat exchanger with the air conditioned space. A pump is used to circulate water through the loop. The photovoltaic system supplies the required electric power of pumps, compressor, and the fan-coil. This system includes PV panels, convertor, and batteries. The batteries store the generated electricity by the PV system during daytime.

3. Energy and Exergy Analyses

The following assumptions are considered for calculating energy and exergy of the streams:

- All of the processes are steady.
- Potential and kinetic energy of the streams are negligible and no chemical reactions exist.
- The compressor mechanical and electrical efficiencies are 80% and 70%, respectively.
- Air is an ideal gas and its specific heat is constant.
- The dead state conditions are selected as $T_0 = 10^\circ\text{C}$ and $P_0 = 101.325\text{ kPa}$.
- The thermodynamic properties of water, air, and R-134a are calculated using the EES software package.
- The mass flow rate calculations are made by EES software.

The case studies are also performed based on the assumptions in Table 1.

3.1. Ground Source Heat Pump. Based on the aforementioned assumptions, mass, energy, and exergy balance equations are applied to find the output power, heat gain, rate of exergy destruction, and energy and exergy efficiencies. The governing equations are as follows [26, 27]:

$$\begin{aligned} \frac{d}{dt}(M_{CV}) &= \sum_{in} \dot{m} - \sum_{out} \dot{m}, \\ \frac{d}{dt}(E_{CV}) &= \dot{Q} + \dot{W} + \sum_{in} \dot{m}h - \sum_{out} \dot{m}h, \\ \frac{d}{dt}(\Phi_{CV}) &= \left[\sum \dot{Q}_i \left(1 - \frac{T_0}{T_i} \right) \right] + \left[\dot{W} + P_0 \frac{d}{dt}(\forall_{CV}) \right] \\ &\quad + \sum_{in} \dot{m}\psi - \sum_{out} \dot{m}\psi - \dot{I}_{CV}, \end{aligned} \quad (1)$$

where exergy of any stream (ψ) is defined as

$$\psi = (h - h_0) - T_0(s - s_0) + \frac{V^2}{2} + gz. \quad (2)$$

TABLE 1: Main assumptions for analysis (Isfahan case study, month of January).

Parameter	Value
<i>General parameters</i>	
Design temperature	22.5 ($^\circ\text{C}$)
Dead state temperature	10 ($^\circ\text{C}$)
Ground temperature	17 ($^\circ\text{C}$)
Thermal load	10.1 (kW)
Solar irradiance	0.2 (kW m^{-2})
Battery efficiency	70%
Power conversion efficiency	18%
<i>GSHX parameters</i>	
Working fluid	Water
Inlet temperature	5 ($^\circ\text{C}$)
Outlet temperature	15 ($^\circ\text{C}$)
Soil resistance	230 ($\text{kW}^{-1} \text{m}^\circ\text{C}$)
Ground pump efficiency	80%
Ground heat exchanger efficiency	80%
<i>Heat pump parameters</i>	
Evaporator pressure	200 (kPa)
Condenser pressure	800 (kPa)
Refrigerant	R-134a
Condenser efficiency	80%
Evaporator efficiency	80%
Compressor efficiency	80%
Expansion valve efficiency	80%
<i>Room heater parameters</i>	
Working fluid	Water
Inlet temperature	20 ($^\circ\text{C}$)
Outlet temperature	30 ($^\circ\text{C}$)
Fan-coil heat exchanger efficiency	80%
Fan-coil pump efficiency	80%

3.1.1. Heat Transfer Process in Fan-Coil. The rate of exergy that is delivered to room due to thermal ($\dot{\Phi}_{load}$) is

$$\dot{\Phi}_{load} = \dot{Q}_{load} \left(1 - \frac{T_0}{T_d} \right), \quad (3)$$

where \dot{Q}_{load} is the heating or cooling load of the building and T_d is indoor design temperature of the building. The irreversibility rate in the air conditioning heat exchanger is

$$\dot{I}_{fan-coil} = \dot{\Phi}_{load} \pm \dot{m}(\psi_{in} - \psi_{out}). \quad (4)$$

3.1.2. Compression Process. In the hybrid cycle, the input exergy required for compression process, either in pumps or in compressor, is delivered from the photovoltaic system with energy efficiency of 15 percent. By neglecting *frictional heating*, the rate of irreversibility for compression process is

$$\dot{I}_{pump} = \dot{W}_{pump} + \dot{m}(\psi_{in} - \psi_{out}). \quad (5)$$

The irreversibility due to energy conversion deficiency in electric motors can be written as

$$\dot{I}_{electric-motor} = \dot{W}_{PV} (1 - \eta_{p,e}). \quad (6)$$

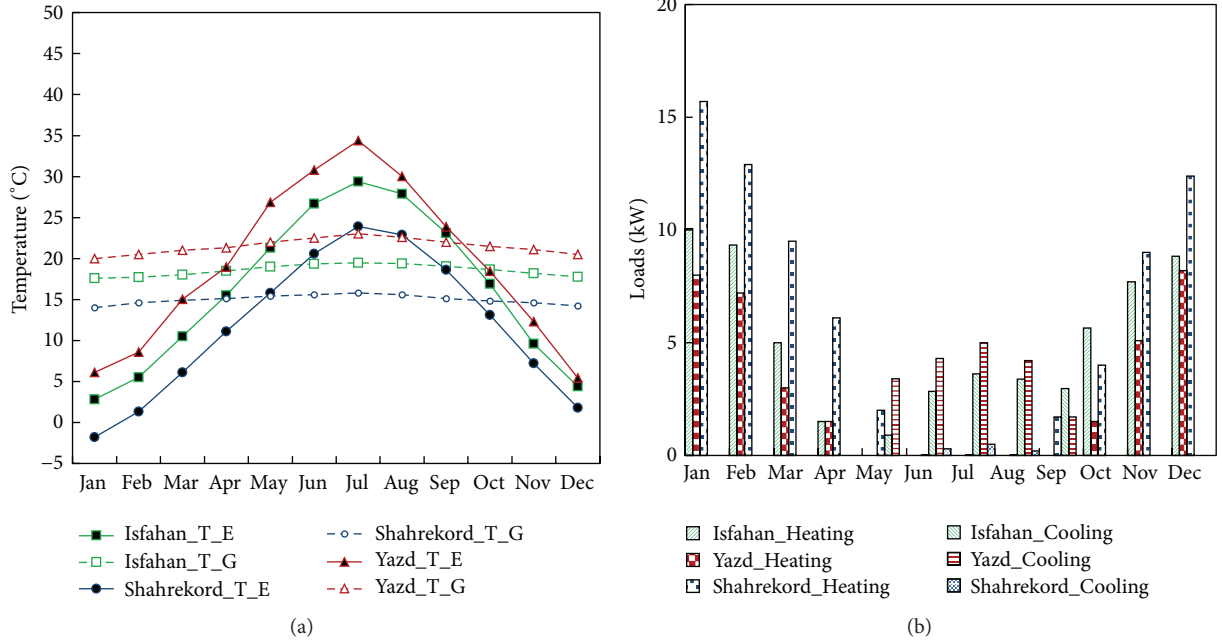


FIGURE 2: Monthly variations of environment and ground temperature for different cities (a) and corresponding cooling and heating loads calculated with available software (b).

3.1.3. *Evaporator and Condenser.* Exergy balance for this process is given by

$$\dot{I}_{CV} = \sum_{in} \dot{m}\psi - \sum_{out} \dot{m}\psi. \quad (7)$$

Thus evaporator or condenser lost exergy is

$$\dot{I}_{e,c} = (\dot{m}_1\psi_{1,in} + \dot{m}_2\psi_{2,in}) - (\dot{m}_1\psi_{1,out} + \dot{m}_2\psi_{2,out}). \quad (8)$$

3.1.4. *Throttling Process.* The exergy loss rate \dot{I}_{CV} in the throttling valve is

$$\dot{I}_{tr} = \dot{m}(\psi_{in} - \psi_{out}). \quad (9)$$

3.1.5. *Ground Source Heat Exchanger.* The exergy rate that is extracted from ground $\dot{\Phi}_{geo}$ is

$$\dot{\Phi}_{geo} = \dot{Q}_{geo} \left(1 - \frac{T_0}{T_{geo}} \right), \quad (10)$$

where \dot{Q}_{geo} is the exchanged heat between the ground and the working fluid in the heat exchanger loop and T_{geo} is the average ground temperature in a specific depth.

The ground temperature T_{geo} is a function of several parameters. It can be calculated using the following equation:

$$T_{geo} = T_{mean} + A' \cos \left(\omega(t - t_0) - \frac{z}{d} \right) \times e^{-z/d}, \quad (11)$$

where T_{mean} is annual average temperature (°C), A' is temperature wave magnitude (°C), ω is temperature wave frequency [$2\pi/(365 \times 24 \text{ hours})$], t_0 is time for the warmest day of a year

(hour), z is ground depth (m), and $d = \sqrt{2\alpha/\omega}$, in which α is heat conductivity of soil (m^2/hour).

The pipe length of GSHX is calculated by

$$L_{GSHX} = \frac{\dot{Q}_{geo}}{T_{geo} - \bar{T}_{W,G}} \frac{1}{R_{tot}}, \quad (12)$$

where R_{tot} is the total thermal resistance of soil, pipe, and water and $\bar{T}_{W,G}$ is the mean temperature of water flowing through ground source heat exchanger. Considering physical properties of polyethylene pipe, soil, and water the total thermal resistance is $R_{tot} \approx 230 \text{ kW/m}^2\text{C}$.

The exergy destruction rate in the heat transfer process is

$$\dot{I}_{GSHX} = \dot{\Phi}_{geo} + \dot{m}(\psi_{in} - \psi_{out}). \quad (13)$$

3.2. *Photovoltaic System.* Solar Irradiance is a measure of how much solar power can be delivered at a specific location. Figure 4 illustrates the monthly solar irradiation averaged over 22 years for different cities. Figure 4 provides the information on the available solar irradiation in case of using PV panel with sun tracking, based on [28]. This information is then used to calculate the average daily power generation from the photovoltaic system in each month.

The actual energy input from solar radiation may be defined as below [23]:

$$\dot{W}_{solar} = AI_s, \quad (14)$$

where I_s is solar irradiance intensity and is A photovoltaic panel net area.

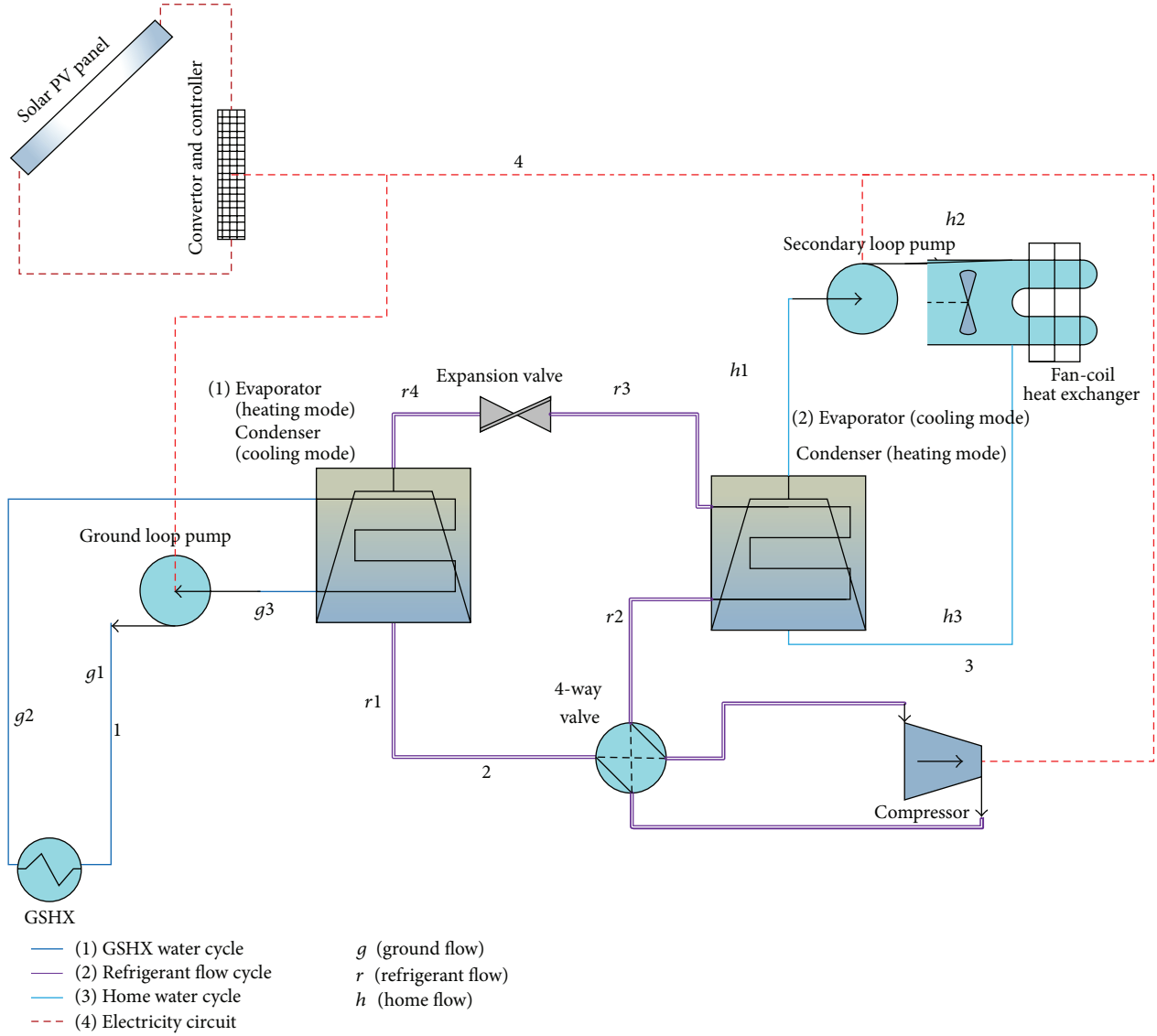


FIGURE 3: Flow diagram of the integrated solar assisted GSHP system.

The input exergy of solar radiation is given by [29]

$$\dot{\Phi}_{\text{in,solar}} = \left(1 - \frac{4}{3} \left(\frac{T_0}{T_s} \right) + \frac{1}{3} \left(\frac{T_0}{T_s} \right)^4 \right) I_s A, \quad (15)$$

where T_s is the sun temperature and is taken as 5777 K. The exergy balance for the PV module can be written to find the associated irreversibility as follows [30–32]:

$$\dot{\Phi}_{\text{in,solar}} = \dot{W}_{\text{PV}} + \dot{I}_{\text{PV}}. \quad (16)$$

It is shown that PV output exergy can be calculated as

$$\dot{W}_{\text{PV}} = V_m I_m, \quad (17)$$

where V_m is PV voltage and I_m is generated current.

The energy conversion efficiency of PV module can be defined as the ratio of the net electrical output power to the input energy as below:

$$\eta_{\text{pce}} = \frac{V_m I_m}{I_s A}. \quad (18)$$

3.3. Overall System Analysis. The input exergy to the hybrid cycle is received from the geothermal source (Φ_{geo}) and photovoltaic system (Φ_{PV}). The desired exergy that is delivered to the house is Φ_{load} . Therefore, the second law efficiency for the hybrid cycle is

$$\eta_{\text{II}} = \frac{\Phi_{\text{load}}}{\Phi_{\text{geo}} + \Phi_{\text{PV}}}. \quad (19)$$

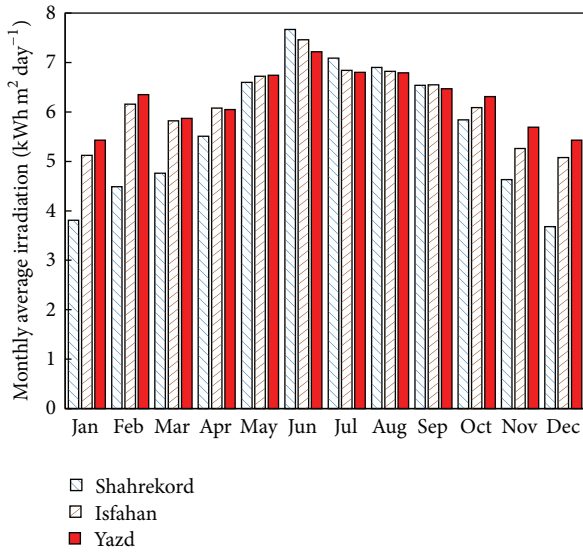


FIGURE 4: Monthly average solar irradiation for different cities.

Total exergy losses are calculated by

$$\dot{I}_{\text{total}} = \dot{I}_{\text{GSHX}} + \dot{I}_{\text{evaporator}} + \dot{I}_{\text{condenser}} + \dot{I}_{\text{tr}} + \sum (\dot{I}_{\text{pump}} + \dot{I}_{\text{electric-motor}}). \quad (20)$$

3.4. Sustainability Analysis. Exergy analysis can be further extended to investigate the sustainability of the cycle, either at design stage or for the existing condition. The sustainability index gives useful information about how exergy efficiency of subsystems affects the sustainability of the energy resources and overall system. Higher sustainability index indicates more sustainability of the process or system. The sustainability index (SI) is defined as [29]

$$SI = \frac{1}{1 - \Psi}, \quad (21)$$

where

$$\Psi = \frac{\text{output exergy}}{\text{input exergy}}. \quad (22)$$

It is also useful to investigate the performance of the subsystems using relative irreversibility (RI), that is, the ratio of the subsystem exergy destruction rate \dot{I}_s to the overall system exergy destruction rate \dot{I}_{tot} :

$$RI = \frac{\dot{I}_s}{\dot{I}_{\text{tot}}}. \quad (23)$$

4. Results and Discussions

4.1. Exergy Flow Diagram. Figure 5 illustrates a Grassmann diagram of the hybrid system. The flow of exergy from energy sources, for example, solar and geothermal energy, useful exergy delivered to building, and exergy destruction are shown, quantitatively. The results are related based on Isfahan

climate in January. It can be concluded that most exergy destruction takes place in photovoltaic modules. Around 82% of the total incident solar exergy is captured by the photovoltaic system, of which about 76% is destroyed due to energy conversion deficiencies of the PV panels. From 24% of the input solar exergy that is delivered to the battery storage, compressor, and pumps, about 15% is destroyed due to irreversibility in these components as well as AC-DC converter. Therefore, almost 10% of solar irradiance exergy would be converted to useful work in the pumps and compressor. Improvement in energy conversion efficiency of the mechanical and electrical equipment's and heat exchanger redesign can avoid exergy losses to some extent. On the other hand, about 67% of the total input exergy from GSHP system that is delivered to the evaporator, condenser, and other heat exchangers is lost due to irreversibility in heat transfer processes.

4.2. Exergy Efficiency. The variation of exergy efficiency of the system during a year is illustrated in Figure 6. The exergy efficiency of the hybrid cycle is almost constant during the hot season and it is at its lowest value of 2%. During the cold season, however, the efficiency of the system would increase. The exergy efficiency is highly dependent on the GSHP performance. During hot seasons, ground temperature and ambient temperature are more close to each other compared to the cold season. It will cause low geothermal exergy input during the hot season. Although, during cold seasons, cooling mode and ambient temperature are so variable (in comparison to the hot season), ground temperature remains nearly constant. This fact causes a variable geothermal exergy input in cold seasons. As solar exergy is relatively less variable during cold seasons, exergy efficiency of the system is highly dependent on geothermal subsystem exergy efficiency. On the other hand, the highest exergy efficiency values are for the coldest season of Jan and Dec. During these seasons, the geothermal system has a better performance because of the highest difference between ground depth temperature and ambient temperature in cold seasons.

4.3. Sustainability and Relative Irreversibility Analysis. Figures 7 and 8 represent the sustainability index of the two main energy harvesting compartments, namely, photovoltaic and geothermal systems, as well as the integrated cycle. As exergy input from the solar system is far greater than the geothermal system (due to extensive destruction of PV system) sustainability index of the integrated system is relatively constant as the solar system. It can be observed from Figure 7 that PV system sustainability has limited dependency on dead state temperature. It can be also concluded from (15) that the difference between temperature of the sun and dead state temperature compensates the effect of this parameter on the input exergy from the sun to the PV system. As shown in Figure 8, the PV system sustainability index is 1.2 during a year. On the other hand, the sustainability index of GSHP system is a function of dead state temperature. Since in this study the ground temperature is taken as 17°C, the GSHP sustainability index is minimum when dead state temperature

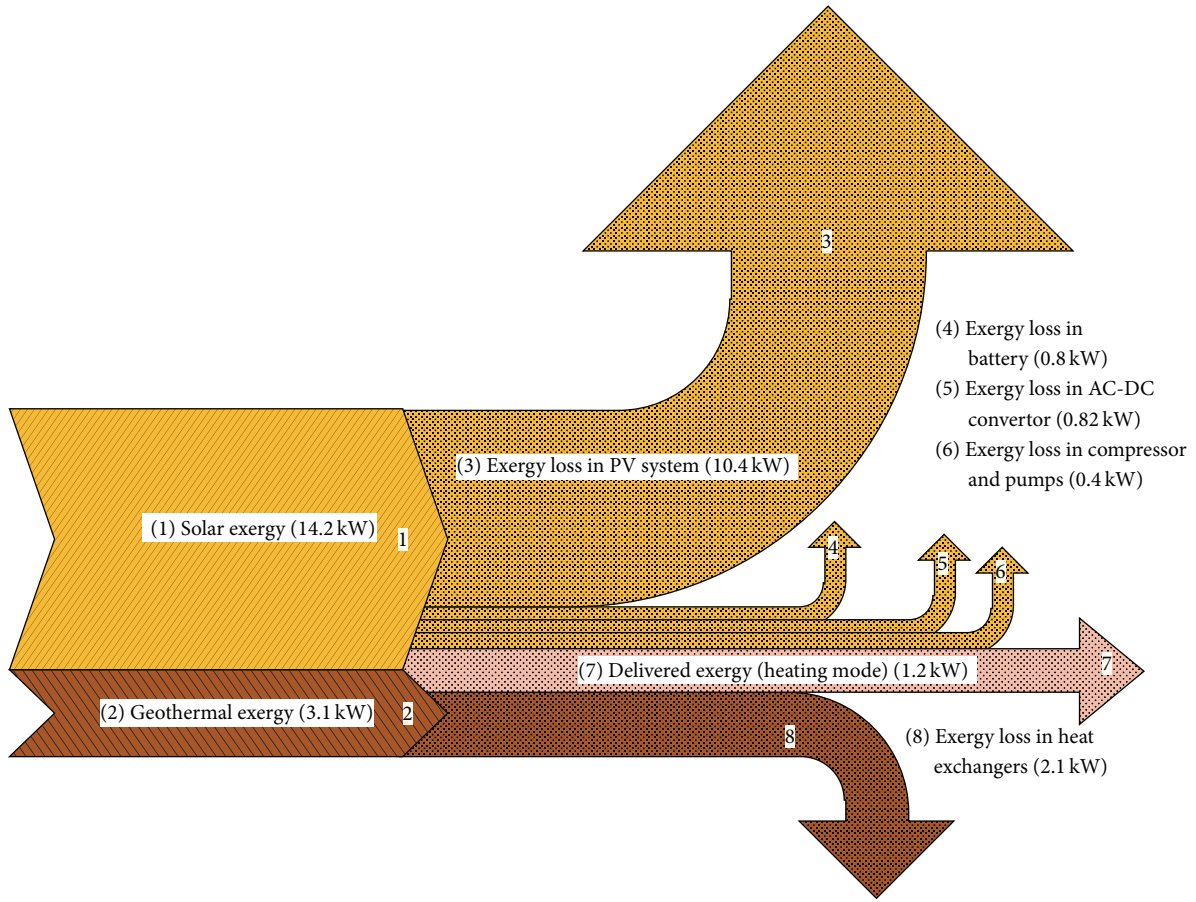


FIGURE 5: Grassmann diagram for hybrid cycle in heating mode (without scale).

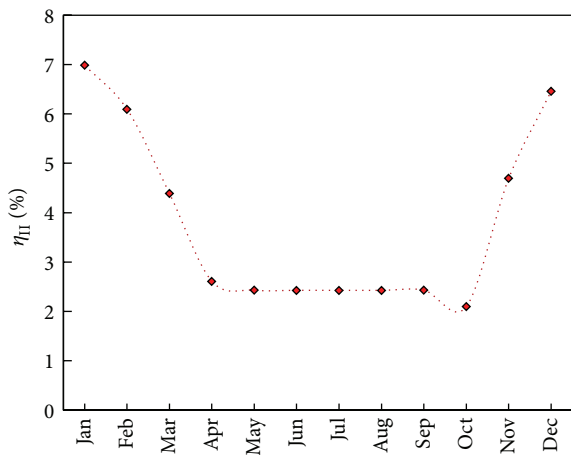


FIGURE 6: Exergy efficiency of integrated SPV and GSHP for different months.

is 15°C. Sustainability index of GSHP will be constant during the hot season (cooling mode) because the design indoor temperature and ground temperature are close to each other and ambient temperature changes are limited. During the cold season, as the ambient temperature decreases the sustainability of GSHP increases. It shows that the hybrid cycle

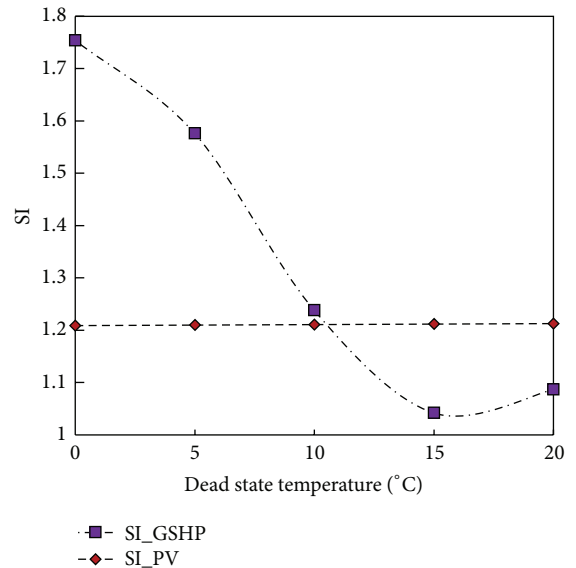


FIGURE 7: Sustainability index of the GSHP and PV systems versus dead state temperature.

is more sustainable, and exergy destruction is lower in the cold season. However, during April and October months due to the close environment temperature to the indoor design

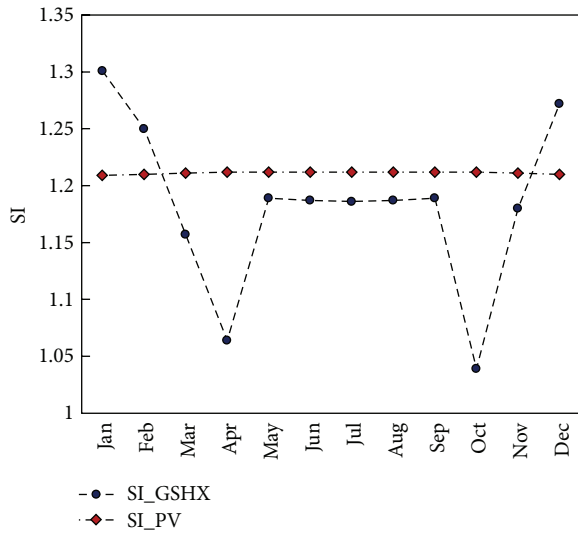


FIGURE 8: Sustainability index of the GSHP and PV systems during a year.

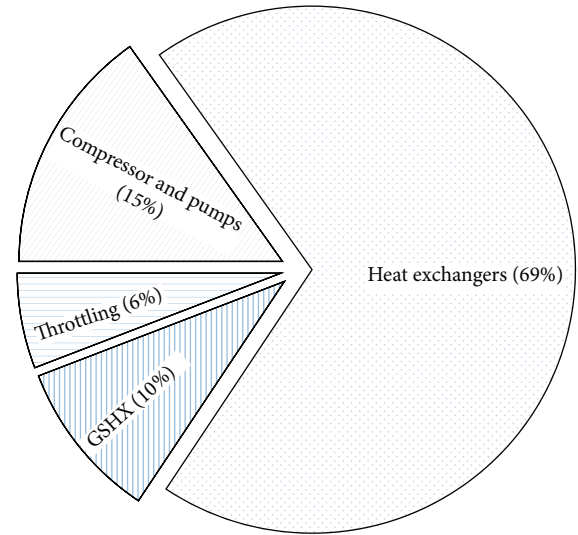


FIGURE 10: Relative irreversibility of GSHP components.

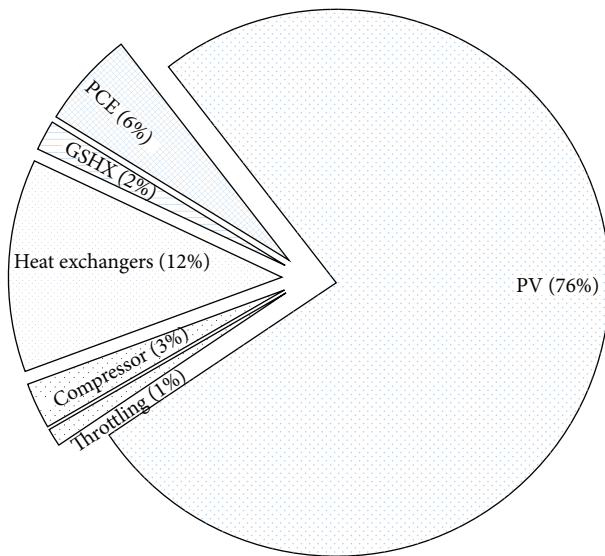


FIGURE 9: Relative irreversibility of components.

temperature, the cooling and heating loads are much smaller than the cycle capacity and the output exergy decreases significantly comparing with input exergy. In fact, the hybrid cycle irreversibility's and exergy destruction increase and its sustainability index are of minimum value during these months.

Figures 9 and 10 illustrate the relative irreversibility of the units/process for the entire cycle and the GSHP subsystem, respectively. It is shown in Figure 9 that most exergy destruction takes place in the PV system. The photovoltaic cells, AC-DC converter, and battery system destruct about 82% of overall input exergy ($I_{PV} + I_{PCE}$). The next most exergy destructive process is related to heat exchange in evaporator and condenser. These two processes destruct almost 12% of the total input exergy. Figure 10 indicates that about 70% of

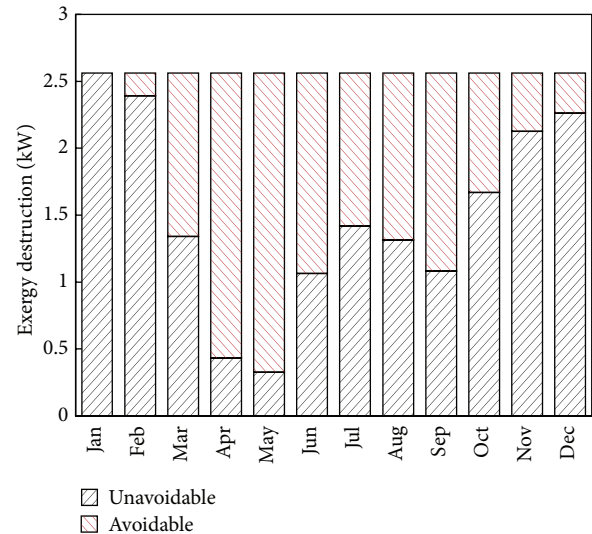


FIGURE 11: Exergy destruction rate of GSHP system during a year.

the exergy destruction in GSHP is due to heat exchange in condenser and evaporator.

4.4. Design Constraint Effects. The main design constraints of the hybrid cycle are the length of ground source heat exchanger and the PV panel's area. Any design criteria for these parameters can change the exergy analysis results. Climate characteristics can also affect the performance of the system. The COP of the system is a function of refrigeration mass flow rate as well. Therefore to reflect the effect of the aforementioned design constraints on the performance of the hybrid cycle from the second law of the thermodynamic point of view, the results are extended as shown in Figures 11–17. The effects of different climates on the performance of the systems are compared in different case scenarios as shown in Figures 16 and 17.

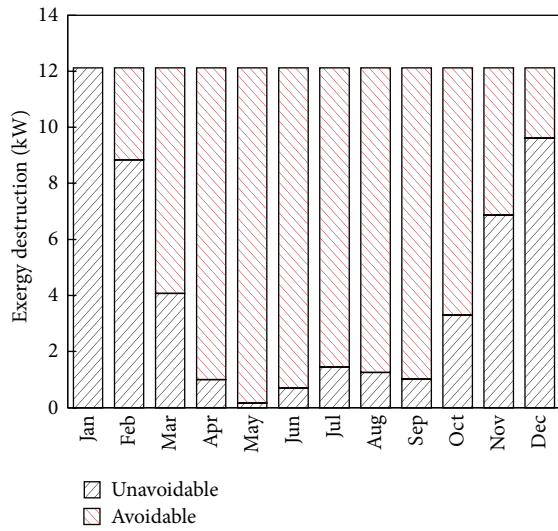


FIGURE 12: Exergy destruction rate of PV system during a year.

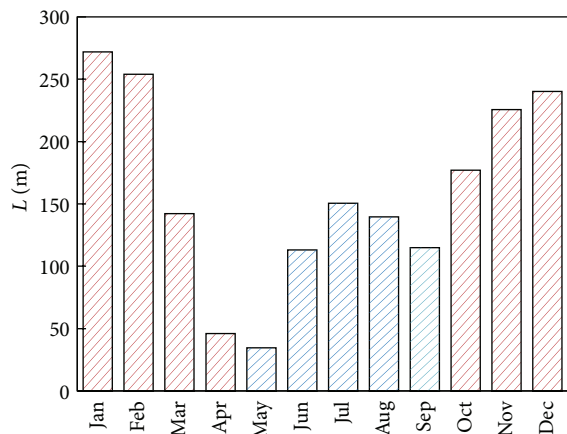


FIGURE 13: GSHX minimum required length for each month.

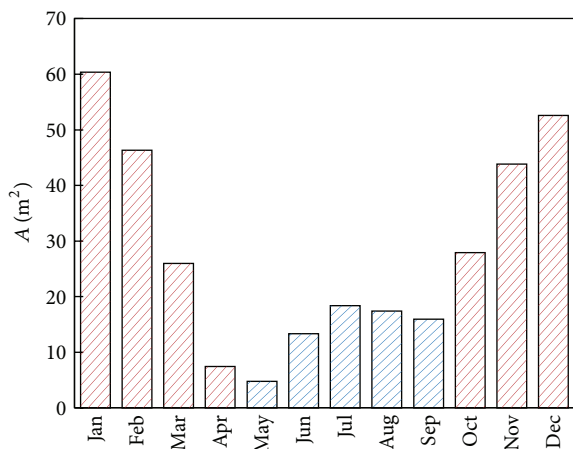


FIGURE 14: PV panel minimum required area for each month.

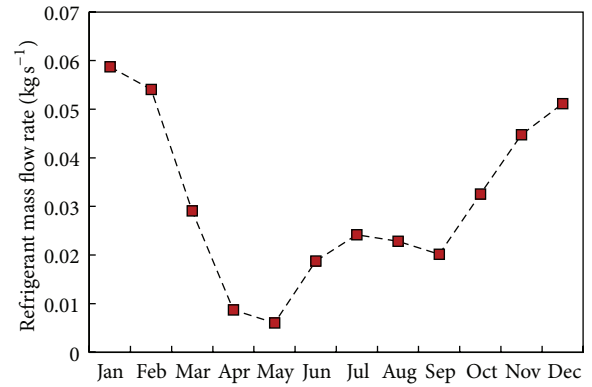


FIGURE 15: Heat pump refrigerant mass flow rate variation.

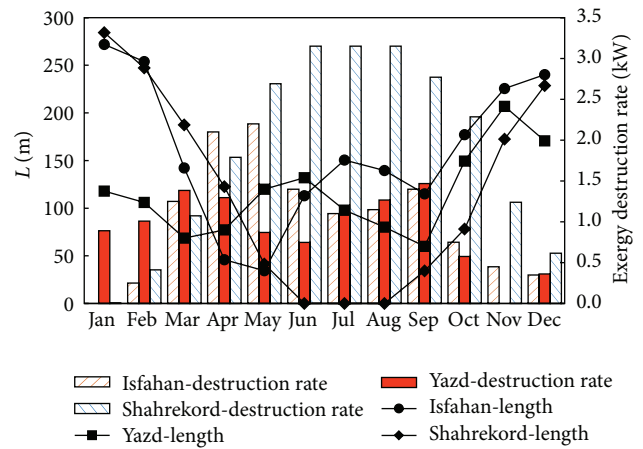


FIGURE 16: Monthly GSHX minimum required length and system exergy destruction rate.

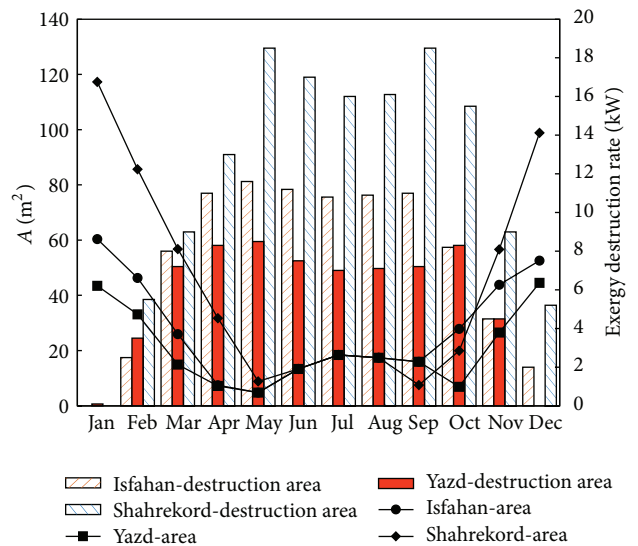


FIGURE 17: Monthly PV panel minimum required area and system exergy destruction rate.

Figures 11 and 12 present the exergy destruction rate of GSHP and PV system during a year based on the minimum required GSHX length and PV panel area, respectively. The exergy destruction rate of the entire cycle can be divided into two unavoidable and avoidable parts. The unavoidable part refers to exergy destruction due to irreversibility of different applicable process that takes place within the hybrid cycle with the minimum required sizes of the compartments, and the other part is related to oversize condition of the system in different months. In other words, unavoidable exergy destruction is due to internal irreversibility of component; however, the avoidable exergy destruction is due to oversize of system such as excessive photovoltaic area or GSHX length. An air conditioning system for a specific building is usually designed for the extreme climate conditions, for example, the hottest and coldest day of a year, and control systems are considered to minimize energy consumption for the rest of the year. However, in case of using solar and geothermal systems, the length of heat exchangers and the area of PV panels only match with the maximum energy demand and it leads to excess input exergy loss during most of the days of operation. It is observed that exergy loss due to input and demand exergy mismatch is much higher in the PV system comparing with GSHP system. Excess available energy can be stored for system operation during either night or peak hours. In fact, the design of the entire cycle can be optimized based on the average energy demand and energy storage systems can be used to compensate for the peak energy consumption conditions. As it is shown in Figures 12 and 14, during the hot season a considerable portion of the solar PV panels is not utilized. Maximum exergy destruction rate occurs in May due to mismatch between system size and building energy demands. The cooling and heating loads at this month are minimum with amount of about 14 kW. Almost 12 kW of destructed exergy at this month is avoidable by energy storage in battery.

The variation of heat pump refrigerant flow rate based on the climate changes during a year is illustrated in Figure 15. It can be concluded that, for the city of Isfahan during the cold months of winter, when both PV panel's area and GSHX length are maximum, high refrigerant flow rates are also required. In fact high energy demand and low solar irradiation during these months lead to considerable almost 2 times increase in irreversibility. This irreversibility mostly occurs in heat exchangers of the hybrid cycle.

4.4.1. Effect of Climate Changes on System Performance. In order to investigate the performance of the hybrid cycle in different climates, the calculations are repeated for two more cities with different weather conditions. The hybrid cycle is designed to supply the maximum and heating and cooling loads during a year. Isfahan city has warm summers and cold winters, Shahrekord city has quite cold winters and mild summers, and Yazd city has very hot summers and mild winters. Ground temperature, weather data, and solar irradiance for the three different cities are obtained via local meteorological data. Variation of the required length of GSHX during a year is more uniform for Yazd city, but the required PV panel area varies considerably. Figures 16 and 17 compare the exergy

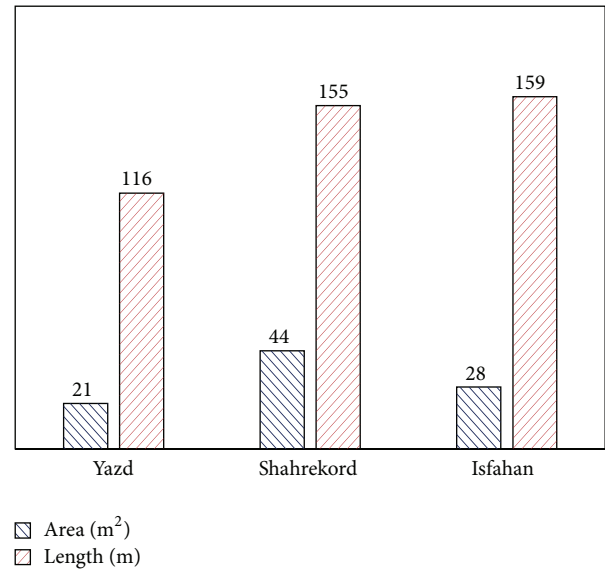


FIGURE 18: Average required PV area and GSHX length.

destruction rates of the hybrid cycle in the three cities. It can be concluded that both GSHX and PV systems have the largest exergy destruction rate in Shahrekord city due to considerable changes of the atmosphere average temperature during a year and also dimensional mismatch between the required and available sizes of GSHX and PV. The building in Shahrekord city has much lower cooling load than heating load, whereas the situation is vice versa in Yazd city. Therefore different arrangements to avoid exergy destruction can be made in these two cities. In other words, energy storage systems and control systems may be applied based on the hybrid cycle performance in each city individually. The results show that the hybrid cycle has almost two times lower exergy destruction rate during the cold season comparing with the hot season. Although the design of GSHX and PV systems is based on the maximum heating and cooling loads, excess absorbed energy can be saved in battery or prevented using a bypass valve in case of ground source heat exchangers.

In another approach, the hybrid cycle can be designed based on the average energy demands of the building during a year. Consequently, the GSHX and PV sizes are reduced and the exergy destruction due to mismatch of the system size and energy demands can be minimized. The capital investment of the system is also reduced considerably. Since the hybrid cycle, in this case, cannot supply the energy demands of the building in some months, the grid electricity may compensate for the required loads. Figure 18 shows the average solar PV panel area and GSHX length for 3 different climates that can be considered for redesigning the cycle; however it might not be the optimum solution as the exergy efficiency and the investment cost should be simultaneously optimized in a detailed study.

4.5. Environmental Benefits. The hybrid GSHP-PV cycle can be utilized to supply the total or part of the building energy demand that leads to considerable decreases in CO₂

emissions. Based on the cooling and heating energy demands of the building that is located in Isfahan, as shown in Figure 2, the annual energy consumption (AEC) would be approximately 60000 kWh per year. Based on the lower heating value (LHV = 47.174 MJ/kg) of natural gas and 40 percent energy conversion efficiency ($\eta = 40\%$) in power plants, almost 20000 m³ of methane will be saved according to (24). Equivalent carbon dioxide emission is calculated by (25). In this equation E_c is specific carbon dioxide emissions of natural gas. Based on (25) (with $E_c = 0.2$) reduction of about 1.2×10^4 kg carbon dioxide emission is achieved annually [22, 33]. If the hybrid cycle is designed based on the average required area and length of PV and GSHX, the annual carbon dioxide emission reduction is almost 0.85×10^4 kg:

$$\forall = 3.6 \text{ (Mj/kWh)} \times \frac{\text{AEC}}{(\rho \times \eta \times \text{LHV})}, \quad (24)$$

$$m = E_c \times \text{AEC}. \quad (25)$$

5. Conclusion

The performance of a hybrid solar-geothermal air conditioning system is investigated to provide the cooling and heating energy demands of a residential building. Utilization of green sources of energy results in low exergy efficiency of about 10 percent, since solar and geothermal energy conversion facilities are considerably exergy destructive. However considerable saving in fossil fuels and reduction in green house effects are observed. The hybrid cycle performance in different climates is evaluated, and it is observed that the exergy destruction due to mismatch of the area of solar panels and length of ground source heat exchanger with energy demands in each month is less in climates with very hot summer and mild winter. The sustainability index of the ground source heat pump systems greatly depends on the dead state temperature whereas the PV system does not. Almost 76 percent of the exergy destruction in the hybrid cycle is due to inefficiencies of the PV system and about 70 percent of irreversibility in GSHP system occurs in the heat exchangers. The following conclusions are made in this study:

- (i) The hybrid system has higher exergy efficiency during the cold season.
- (ii) In the hybrid system, exergy destruction mostly takes place in photovoltaic modules.
- (iii) The photovoltaic cells, AC-DC converter, and battery system destruct about 82% of overall input exergy.
- (iv) About 76% of PV panel input exergy is destroyed due to energy conversion deficiencies of the PV panels.
- (v) Exergy loss due to mismatch of input and demand exergy is much higher in the PV system comparing with the GSHP system.
- (vi) In the GSHP system, most exergy destruction takes place in heat exchangers.
- (vii) Geothermal system has a better performance during the cold season, because of the highest difference

between ground depth temperature and ambient temperature.

- (viii) The PV system sustainability index is 1.2 during a year, but the sustainability index of GSHP system is a function of dead state temperature.
- (ix) The hybrid system is more sustainable during the cold season.
- (x) If the hybrid cycle is designed based on the average energy demands of the building during a year, the GSHX and PV sizes are reduced and the exergy destruction due to mismatch of the system size and energy demands can be minimized.
- (xi) If the cycle is designed based on the average required area and length of PV and GSHX the annual carbon dioxide emission reduction is almost 5×10^4 kg.

The evaluation of the hybrid system (GSHP coupled with PV panel) for different cities (with different climates) results in the following conclusions:

- (i) Both GSHX and PV systems have the largest exergy destruction rate in Shahrekord city (the coldest climate) due to considerable changes of the atmosphere average temperature during a year and also dimensional mismatch between the required and available sizes of GSHX and PV.
- (ii) Different arrangements to avoid exergy destruction can be made in Shahrekord and Yazd.

Although coupling the GSHX and PV systems causes considerable exergy destruction (especially during the cold season), the hybrid system is capable of providing a clean source of district cooling and heating for regions with limited access to power grid. It is suggested that more study be conducted in order to evaluate primary and secondary cost (exergoeconomical aspect). The optimum design of the GSHX-PV system can be identified using exergoeconomic analysis that is undertaken as the continuation of this study.

Nomenclatures

Variables

- A: Photovoltaic panels area (m²)
 AEC: Annual energy consumption (kWh)
 A': Temperature wave magnitude (K)
 d: Depth parameter (m)
 E: Energy (kJ)
 E_c: Specific carbon dioxide emissions
 h: Enthalpy per unit of mass (kJ kg⁻¹)
 I: Irradiance intensity (kJ m⁻²)
 İ: Irreversibility (destruction) rate (kJ s⁻¹)
 I_m: Electrical current (ampere)
 L: Ground heat exchanger length (m)
 LHV: Lower heating value (MJ/kg)
 P: Reference pressure (kPa)
 Q̇: Heat transfer rate (kJ)
 R: Heat resistance (kJ m⁻¹ s⁻¹ K⁻¹)

T : Temperature (K)
 \bar{T} : Mean temperature (K)
 V_m : Electrical voltage (volt)
 \dot{W} : Work rate (kJ)
 m : Mass (kg)
 \dot{m} : Mass flow rate (kg s^{-1})
 n : Number of heat exchangers
 t : Time (s)
 t_0 : Time of the year's warmest day (hour)
 V : Velocity (m s^{-1})
 z : Ground depth (m)
 \forall : Volume (m^3).

Greek Letters

Φ : Exergy (kJ)
 Ψ : Flow exergy (kJ kg^{-1})
 α : Conductivity of soil ($\text{m}^2 \text{s}^{-1}$)
 π : Global constant
 \mathcal{G} : Gravity acceleration (m s^{-2})
 ψ : Flow exergy (kJ kg^{-1})
 ω : Temperature wave frequency (s^{-1}).

Efficiencies

COP: Coefficient of performance
 η_{II} : Exergy efficiency
 $\eta_{g,p}$: Ground pump efficiency
 $\eta_{g,x}$: Ground heat exchanger efficiency
 $\eta_{p,1,c}$: Evaporator efficiency in cooling mode
 $\eta_{p,2,c}$: Condenser efficiency in cooling mode
 $\eta_{p,1,h}$: Evaporator efficiency in heating mode
 $\eta_{p,2,h}$: Condenser efficiency in heating mode
 $\eta_{p,p}$: Refrigerant pump efficiency
 $\eta_{p,v}$: Expansion valve efficiency
 η_{pce} : Power conversion efficiency
 $\eta_{s,f}$: Fan-coil heat exchanger efficiency
 $\eta_{s,p}$: Fan-coil pump efficiency.

Subscripts

0 : Dead state (reference)
 CV: Control Volume
 PV: Photovoltaic
 c : Compressor
 d : Design condition
 e : Electrical
 g : Ground
 geo: Geothermal
 i : Initial condition
 in: Inlet
 load: Cooling and heating loads
 mean: Averaged
 out: Outlet
 tot: Total condition
 tr: Throttling Process
 s : Solar.

Operators

d/dt : Time derivation
 Σ : Summation.

Abbreviations

EES: Engineering Equation Solver
 GSHP: Ground source heat pump
 GSHX: Ground source heat exchanger.

Competing Interests

The authors declare that they have no competing interests.

References

- [1] D. Üрге-Vorsatz, L. F. Cabeza, S. Serrano, C. Barreneche, and K. Petrichenko, "Heating and cooling energy trends and drivers in buildings," *Renewable and Sustainable Energy Reviews*, vol. 41, pp. 85–98, 2015.
- [2] Low Exergy Systems for High-Performance Buildings and Communities, <http://www.annex49.info/background.html>.
- [3] D. Schmidt, "Low exergy systems for high-performance buildings and communities," *Energy and Buildings*, vol. 41, no. 3, pp. 331–336, 2009.
- [4] O. Kwon, K. Bae, and C. Park, "Cooling characteristics of ground source heat pump with heat exchange methods," *Renewable Energy*, vol. 71, pp. 651–657, 2014.
- [5] M. De Carli, S. Fiorenzato, and A. Zarrella, "Performance of heat pumps with direct expansion in vertical ground heat exchangers in heating mode," *Energy Conversion and Management*, vol. 95, pp. 120–130, 2015.
- [6] W. Wu, T. You, B. Wang, W. Shi, and X. Li, "Simulation of a combined heating, cooling and domestic hot water system based on ground source absorption heat pump," *Applied Energy*, vol. 126, pp. 113–122, 2014.
- [7] M. Yari and N. Javani, "Performance assessment of a horizontal-coil geothermal heat pump," *International Journal of Energy Research*, vol. 31, no. 3, pp. 288–299, 2007.
- [8] J. Hirvonen, G. Kayo, S. Cao, A. Hasan, and K. Sirén, "Renewable energy production support schemes for residential-scale solar photovoltaic systems in Nordic conditions," *Energy Policy*, vol. 79, pp. 72–86, 2015.
- [9] A. Martinez-Rubio, F. Sanz-Adan, and J. Santamaria, "Optimal design of photovoltaic energy collectors with mutual shading for pre-existing building roofs," *Renewable Energy*, vol. 78, pp. 666–678, 2015.
- [10] E. K. Akpınar and A. Hepbasli, "A comparative study on exergetic assessment of two ground-source (geothermal) heat pump systems for residential applications," *Building and Environment*, vol. 42, no. 5, pp. 2004–2013, 2007.
- [11] Y. Bi, X. Wang, Y. Liu, H. Zhang, and L. Chen, "Comprehensive exergy analysis of a ground-source heat pump system for both building heating and cooling modes," *Applied Energy*, vol. 86, no. 12, pp. 2560–2565, 2009.
- [12] A. Hepbasli and O. Akdemir, "Energy and exergy analysis of a ground source (geothermal) heat pump system," *Energy Conversion and Management*, vol. 45, no. 5, pp. 737–753, 2004.
- [13] H. Sayyaadi, E. H. Amlashi, and M. Amidpour, "Multi-objective optimization of a vertical ground source heat pump using

- evolutionary algorithm,” *Energy Conversion and Management*, vol. 50, no. 8, pp. 2035–2046, 2009.
- [14] L. C. Tagliabue, M. Maistrello, and C. Del Pero, “Solar heating and air-conditioning by GSHP coupled to PV system for a cost effective high energy performance building,” *Energy Procedia*, vol. 30, pp. 683–692, 2012.
- [15] M. Bakker, H. A. Zondag, M. J. Elswijk, K. J. Strootman, and M. J. M. Jong, “Performance and costs of a roof-sized PV/thermal array combined with a ground coupled heat pump,” *Solar Energy*, vol. 78, no. 2, pp. 331–339, 2005.
- [16] A. L. Biauou and M. A. Bernier, “Achieving total domestic hot water production with renewable energy,” *Building and Environment*, vol. 43, no. 4, pp. 651–660, 2008.
- [17] Q.-Y. Li, Q. Chen, and X. Zhang, “Performance analysis of a rooftop wind solar hybrid heat pump system for buildings,” *Energy and Buildings*, vol. 65, pp. 75–83, 2013.
- [18] M. Mikati, M. Santos, and C. Armenta, “Electric grid dependence on the configuration of a small-scale wind and solar power hybrid system,” *Renewable Energy*, vol. 57, pp. 587–593, 2013.
- [19] L. Dai, S. Li, L. DuanMu, X. Li, Y. Shang, and M. Dong, “Experimental performance analysis of a solar assisted ground source heat pump system under different heating operation modes,” *Applied Thermal Engineering*, vol. 75, pp. 325–333, 2015.
- [20] E. Bertram, “Solar assisted heat pump systems with ground heat exchanger—simulation studies,” *Energy Procedia*, vol. 48, pp. 505–514, 2014.
- [21] A. Sahay, V. K. Sethi, A. C. Tiwari, and M. Pandey, “A review of solar photovoltaic panel cooling systems with special reference to Ground coupled central panel cooling system (GC-CPCS),” *Renewable and Sustainable Energy Reviews*, vol. 42, pp. 306–312, 2015.
- [22] F. Sobhnamayan, F. Sarhaddi, M. A. Alavi, S. Farahat, and J. Yazdanpanahi, “Optimization of a solar photovoltaic thermal (PV/T) water collector based on exergy concept,” *Renewable Energy*, vol. 68, pp. 356–365, 2014.
- [23] E. Saloux, A. Teyssedou, and M. Sorin, “Analysis of photovoltaic (PV) and photovoltaic/thermal (PV/T) systems using the exergy method,” *Energy and Buildings*, vol. 67, pp. 275–285, 2013.
- [24] M. Gholampour, M. Ameri, and M. Sheykh Samani, “Experimental study of performance of Photovoltaic-Thermal Unglazed Transpired Solar Collectors (PV/UTCs): energy, exergy, and electrical-to-thermal rational approaches,” *Solar Energy*, vol. 110, pp. 636–647, 2014.
- [25] S. N. Jahromi, A. Vadiee, and M. Yaghoubi, “Exergy and economic evaluation of a commercially available PV/T collector for different climates in Iran,” *Energy Procedia*, vol. 75, pp. 444–456, 2015.
- [26] A. Bejan, *Advanced Engineering Thermodynamics*, John Wiley & Sons, New York, NY, USA, 1988.
- [27] K. Wark, *Advanced Thermodynamics for Engineers*, McGraw-Hill, New York, NY, USA, 1995.
- [28] M. Boxwell, *Solar Electricity Handbook: A Simple, Practical Guide to Using Electric Solar Panels and Designing and Installing Photovoltaic Solar PV Systems*, Code Green Publishing, 2009.
- [29] H. Caliskan, I. Dincer, and A. Hepbasli, “Energy, exergy and sustainability analyses of hybrid renewable energy based hydrogen and electricity production and storage systems: modeling and case study,” *Applied Thermal Engineering*, vol. 61, no. 2, pp. 784–798, 2013.
- [30] S. Kalogirou, *Solar Energy Engineering: Processes and Systems*, Academic Press, 2009, <http://www.books24x7.com/marc.asp?bookid=37184>.
- [31] J. R. S. Brownson, *Solar Energy Conversion Systems*, 2014, <http://public.eblib.com/choice/publicfullrecord.aspx?p=1562328>.
- [32] C. Koroneos and M. Tsarouhis, “Exergy analysis and life cycle assessment of solar heating and cooling systems in the building environment,” *Journal of Cleaner Production*, vol. 32, pp. 52–60, 2012.
- [33] Carbon Dioxide Emission, http://www.engineeringtoolbox.com/co2-emission-fuels-d_1085.html.

Research Article

Exact Optimum Design of Segmented Thermoelectric Generators

M. Zare,¹ H. Ramin,² S. Naemi,¹ and R. Hosseini¹

¹Mechanical Engineering Department, Amirkabir University of Technology, 424 Hafez Avenue, P.O. Box 15875-4413, Tehran, Iran

²Center of Excellence in Design and Optimization of Energy Systems, School of Mechanical Engineering, College of Engineering, University of Tehran, Tehran, Iran

Correspondence should be addressed to H. Ramin; hadi.ramin@ut.ac.ir

Received 11 December 2015; Revised 10 March 2016; Accepted 20 March 2016

Academic Editor: Pouria Ahmadi

Copyright © 2016 M. Zare et al. This is an open access article distributed under the Creative Commons Attribution License, which permits unrestricted use, distribution, and reproduction in any medium, provided the original work is properly cited.

A considerable difference between experimental and theoretical results has been observed in the studies of segmented thermoelectric generators (STEGs). Because of simplicity, the approximate methods are widely used for design and optimization of the STEGs. This study is focused on employment of exact method for design and optimization of STEGs and comparison of exact and approximate results. Thus, using new highly efficient thermoelectric materials, four STEGs are proposed to operate in the temperature range of 300 to 1300 kelvins. The proposed STEGs are optimally designed to achieve maximum efficiency. Design and performance characteristics of the optimized generators including maximum conversion efficiency and length of elements are calculated through both exact and approximate methods. The comparison indicates that the approximate method can cause a difference up to 20% in calculation of some design characteristics despite its appropriate results in efficiency calculation. The results also show that the maximum theoretical efficiency of 23.08% is achievable using the new proposed STEGs. Compatibility factor of the selected materials for the proposed STEGs is also calculated using both exact and approximate methods. The comparison indicates a negligible difference in calculation of compatibility factor, despite the considerable difference in calculation of reduced efficiency (temperature independence efficiency).

1. Introduction

Nowadays, the use of thermoelectric cooler and generator has become increasingly developed. The thermoelectric applications include electronic cooling, portable refrigerator, air conditioning, high-precision temperature measurement, and space applications. The thermoelectric method has outstanding features compared to the other energy conversion methods such as exclusion of moving parts, high reliability, and long life span [1]. In addition, there are several studies on the combined use of the thermoelectric technology with other energy conversion methods (e.g., steam and gas turbine) as an efficient way of harnessing waste heat in power plant and other industries [2]. However, the need for high temperature heat source and low efficiency is a remarkable challenge in the thermoelectric technology. Today, the first challenge has been overcome thanks to the abundant waste heat sources, high temperature exhausted gas of diesel engine [3], and so forth. However, so many studies have been done to increase the efficiency of thermoelectric applications and a lot is still

needed. The effort to enhance thermoelectric efficiency can be classified into three categories: invention and development of highly efficient materials, segmentation, and cascading. The first two of them are discussed in the current study.

Invention and Development of Highly Efficient Materials. Thermoelectric efficiency not only depends on temperature, but also depends on physical properties of the material such as electrical and thermal conductivity and Seebeck coefficient. The effect of such properties on efficiency can be analysed using figure of merit (FOM or Z) or dimensionless figure of merit (ZT). The higher the FOM, the higher the conversion efficiency. In this category, the attempts are inclined to enhance the performance of thermoelectric applications by modification of physical properties which results in the increase of FOM, that is, increase in Peltier coefficient, electrical conductivity, and thermal resistivity. Many studies have focused on this category. In particular, in recent years, with the advent of nanotechnology, many researchers have made attempts to develop thermoelectric materials with

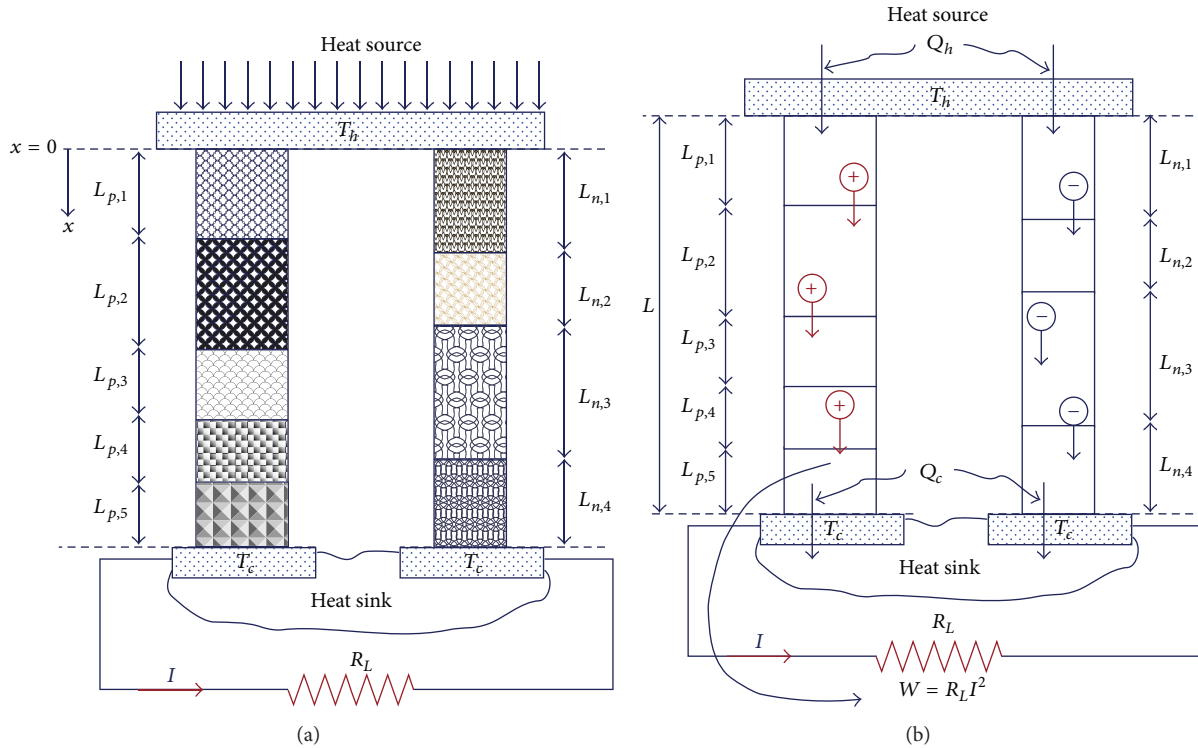


FIGURE 1: Schematic of a segmented thermoelectric generator.

higher FOM [4–7]. The remarkable achievements of Boston and MIT researchers can be mentioned [8, 9].

Segmentation. Considering the temperature dependence of FOM, so far, no material has been found with a satisfactory FOM within a sufficiently large temperature range (e.g., 300 to 1300 K). Different materials have a satisfactory FOM only within a limited temperature range. Hence, the segmented thermoelectric devices have emerged (see Figure 1(a) which shows a segmented thermoelectric generator). In the segmented thermoelectric device, each material is supposed to be used in its own specific temperature range, in which it has a reasonable FOM. Numerous researches have been done in this category. Chen et al. [8] proposed a STEG for operation between 300 and 900 K and achieved theoretical efficiency of 15%. Kang et al. [10] presented a *p*-type thermoelectric leg and claimed that 17% efficiency can be achieved experimentally. Snyder and Caillat [11] presented a STEG, considering compatibility factor. With the assumption of negligible contact resistance and adiabatic outside surface area, they achieved 18.1% efficiency theoretically in temperature range of 25 and 1000°C.

Efficiency calculation is one of the most important parts of thermoelectric generators research, as it is important in other energy conversion methods. Due to importance of efficiency, several researches have been conducted on the methods of efficiency calculation of thermoelectric generators. Sherman et al. [12] presented a comprehensive method for calculation of performance of thermoelectric devices. With the advent of segmented thermoelectric systems, Swanson et al. [13] offered an approximate method for calculation of

performance and design of segmented thermoelectric systems. Moore [14] calculated the performance characteristics of a feasible STEG using the exact and Swanson et al.'s methods and compared the results. Moore did not design or optimize a STEG; he only focused on performance calculation of a predesigned generator. El-Genk and Saber [15] improved Swanson et al.'s method. Their model uses volume average to calculate thermoelectric properties rather than temperature average of Swanson et al.'s method. Until now, due to the widespread application of STEGs, the researchers work on a new methodology for calculation of the efficiency of the STEGs [16, 17].

Considering FOM as the only factor in design of STEGs can adversely affect the thermoelectric efficiency. Therefore, another parameter (called compatibility factor) must be considered in design of STEGs. The compatibility factor also shows whether segmentation or cascading should be used in different conditions [18].

One of the most important steps in exergy analysis of energy systems is identification of waste heat sources in order to minimize exergy destruction. The thermoelectric technology is a promising way to harness the waste heat. Thus, the thermoelectric generators and specially STEGs are of importance in exergy optimization. A considerable difference between experimental and theoretical results (approximate methods) has been observed in the studies of STEGs [15]. Although a major portion of the differences can result from contact resistance and experimental uncertainty, it seems necessary to confirm the validity of theoretical results. Up to now, all of the thermoelectric researchers use the approximate methods for design and optimization of the STEGs, because

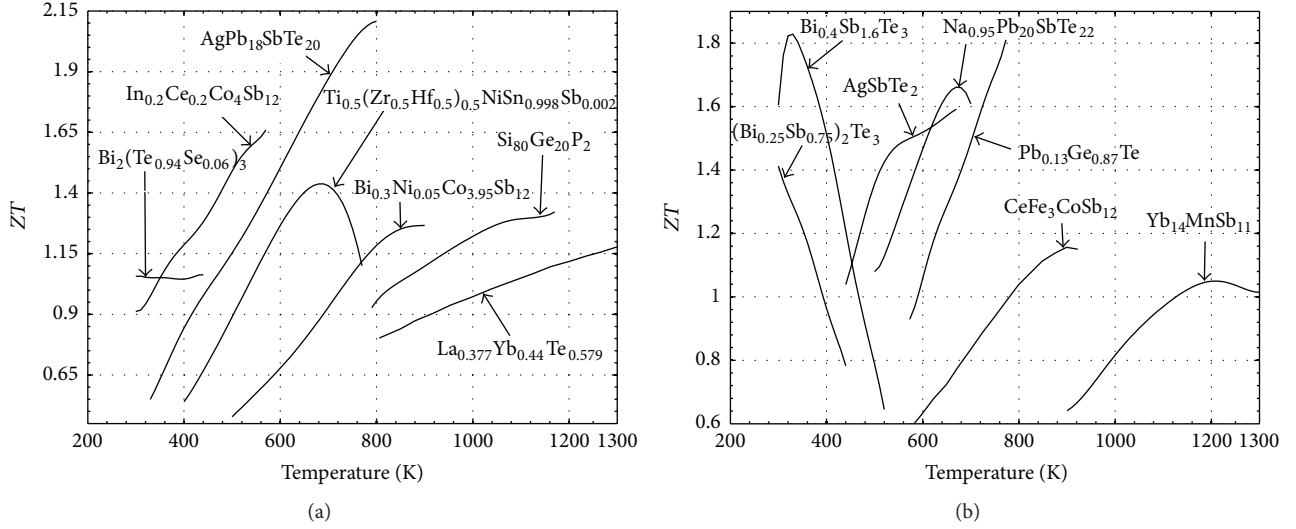


FIGURE 2: Temperature dependence of dimensionless figure of merit for (a) *n*-type and (b) *p*-type materials.

of their simplicity. But this may be a cause of the difference between experimental and theoretical results. There was lack of using exact method for optimization of STEGs in the literature; therefore, application of exact method can bridge the gap between theoretical and experimental results [15–17]. Considering this fact, the main objectives of this study can be categorized as follows:

- (i) In order to design and optimize STEGs, at the first step, the chemically and physically modified thermoelectric materials are reviewed. Thus, the materials which have high efficiency in a temperature range are selected. Then, four STEGs are proposed for optimization process.
- (ii) As the main objective of this study, the proposed STEGs are optimized using the exact method rather than the common simple approximate methods. Then, the design and performance characteristics of the STEGs are calculated through exact method.
- (iii) Finally, the design and performance characteristics of the proposed STEGs are also calculated through common approximate methods. Then, the results of exact and approximate methods are compared.

2. Selection of Materials

In this paper, a major study has been done on the latest known thermoelectric materials, the best of which have been applied for the design of a thermoelectric generator. Due to the temperature dependence of FOM, the materials with a satisfactory FOM in a specific temperature range have been selected. Figures 2(a) and 2(b) show the variation of FOM with temperature for *n*-type and *p*-type legs, respectively. Two arrangements have been optimized for each type of leg. Next, by considering different combinations, four STEGs have been proposed and analysed. The materials used in the mentioned arrangements, as well as temperature ranges for each arrangement, are presented in Table 1.

3. Optimization and Performance Calculations

3.1. Exact Method. Performance calculation methods of single-segmented generator were introduced by Sherman et al. [12]. Efficiency of a thermoelectric generator is defined by the following relation:

$$\eta = \frac{W}{Q_h}, \quad (1)$$

where W and Q_h are output power and input heat, respectively (see Figure 1(b)). Assuming ideal condition,

$$W = R_L I^2 = Q_h - Q_c, \quad (2)$$

where R_L , I , and Q_c are load resistance, electrical current, and output heat, respectively. Using relations (1) and (2) for given Q_h and Q_c , it is possible to calculate efficiency. Q_c and Q_h are determined by energy balance in cold and hot junctions as follows [12]:

$$Q_c = \pi_c I + A_p k_p (T_c) \frac{dT_p}{dx}(L) + A_n k_n (T_c) \frac{dT_n}{dx}(L), \quad (3)$$

$$Q_h = \pi_h I + A_p k_p (T_h) \frac{dT_p}{dx}(0) + A_n k_n (T_h) \frac{dT_n}{dx}(0),$$

where A , k , and π are cross section area, thermal conductivity, and Peltier coefficient, respectively. The subscripts c , h , p , and n refer to cold junction, hot junction, *p*-type leg, and *n*-type leg, respectively. Equation (3) denotes that it is necessary to determine temperature gradient as well as the electrical current passing through the legs to calculate Q_c and Q_h . Therefore, it is essential to determine the temperature

TABLE 1: The materials of the proposed arrangements and their operation temperature range.

$p1$ (temperature range)	$p2$ (temperature range)	$n1$ (temperature range)	$n2$ (temperature range)
$(\text{Bi}_{0.25}\text{Sb}_{0.75})_2\text{Te}_3$ [19] (300–440)	$\text{Bi}_{0.4}\text{Sb}_{1.6}\text{Te}_3$ [20] (300–520)	$\text{Bi}_2(\text{Te}_{0.94}\text{Se}_{0.06})_3$ [21] (300–440)	$\text{In}_{0.2}\text{Ce}_{0.2}\text{Co}_4\text{Sb}_{12}$ [22] (300–570)
AgSbTe_2 [23] (440–670)	$\text{Na}_{0.95}\text{Pb}_{20}\text{SbTe}_{22}$ [24] (520–700)	$\text{AgPb}_{18}\text{SbTe}_{20}$ [25] (440–800)	$\text{AgPb}_{18}\text{SbTe}_{20}$ [25] (570–800)
$\text{Pb}_{0.13}\text{Ge}_{0.87}\text{Te}$ [26] (670–770)	$\text{Pb}_{0.13}\text{Ge}_{0.87}\text{Te}$ [26] (700–770)	$\text{Si}_{80}\text{Ge}_{20}\text{P}_2$ [27] (800–1200)	$\text{Si}_{80}\text{Ge}_{20}\text{P}_2$ [27] (800–1200)
$\text{CeFe}_3\text{CoSb}_{12}$ [28] (770–920)	$\text{CeFe}_3\text{CoSb}_{12}$ [28] (770–920)	$\text{La}_{0.377}\text{Yb}_{0.44}\text{Te}_{0.579}$ [29] (1200–1300)	$\text{La}_{0.377}\text{Yb}_{0.44}\text{Te}_{0.57}$ [29] (1200–1300)
$\text{Yb}_{14}\text{MnSb}_{11}$ [30] (920–1300)	$\text{Yb}_{14}\text{MnSb}_{11}$ [30] (920–1300)	—	—

distribution in legs. The temperature distribution of a single-segmented leg is calculated through the following equation [31]:

$$\frac{d}{dx} [k(T) T'(x)] - \gamma(T) J T'(x) + \rho(T) J^2 = 0, \quad (4)$$

$$\gamma(T) = T \frac{d\alpha}{dT}, \quad J = \frac{I}{A}.$$

In the above equation, T' is derivative of temperature with respect to x . γ and J are Thomson coefficient and current density, respectively. It is evident that solving such equation requires knowing exactly how the thermoelectric properties change with temperature. Equation (4) is solved for each leg using the following change of variable:

$$y(T) = -\frac{k(T)}{J dx/dT} \quad (5)$$

$$\text{or } u = -\frac{J}{k(T) dT/dx}.$$

Hence, (4) can be written as the following:

$$\frac{dy}{dT} = -\gamma(T) - \frac{\rho(T) K(T)}{y(T)} \quad (6)$$

$$\text{or } \frac{du}{dT} = (\gamma(T) + \rho(T) K(T) y(T)) u^2,$$

where u represents relative current density. In exact method, the above equation can be solved using the variable substitution of (5) and considering an initial condition for $u(T)$ or $y(T)$. The solution results include determination of electrical current and temperature distribution, two mentioned necessary factors for calculation of Q_c and Q_h . Consequently, the efficiency is determined. Next, the efficiency can be maximized by repeating the process with different initial conditions.

In this study, specific modifications must be applied to this process due to the fact that more than one material is used in each leg and the Peltier heat is also presented in each interface. To solve the problem, (4) is solved separately for each segment, and the following continuity conditions

are applied at the interfaces for n -type and p -type legs, respectively [14]:

$$k_j A_j T'_j = k_{j+1} A_{j+1} T'_{j+1} + TI (\alpha_{j+1} - \alpha_j), \quad (7)$$

$$k_j A_j T'_j = k_{j+1} A_{j+1} T'_{j+1} - TI (\alpha_{j+1} - \alpha_j).$$

Electrical and thermal conductivity and Seebeck coefficient of the materials have been obtained from references given in Table 1. Then, (4) has been solved numerically using $\Delta T = 1$ and assuming initial condition for $u(T_h)$ or $y(T_h)$.

Integrating of (4) gives (8) which is used for calculation of current density:

$$\int_{T_c}^{T_h} k(T) u(T) dT = -JL. \quad (8)$$

The length of each segment is calculated using (8) and conservation of electrical current.

It is common that the cross section area of p -leg is assumed to be constant and the cross section of n -leg is optimized. Hence, $A_{n,\text{opt}}$ is obtained using current density, conservation of electrical current, and the assumption of $A_p = 100 \text{ mm}^2$. Consequently, the cross section area ratio is calculated.

The internal resistance (R_{int}) is calculated using material properties and relation $R = \rho L/A$. Finally, $R_{L,\text{opt}}$ and the resistance ratio are calculated through (2).

3.2. Swanson et al.'s Method. In approximate methods such as Swanson et al.'s method, approximate equations are used, rather than (4), to determine the efficiency. In fact, Swanson et al.'s method includes calculation of performance characteristics on the basis of temperature average properties. In this method, an approximate relation for efficiency is derived in terms of temperature average properties. The next step is optimization of all characteristics including the ratios of cross section area and resistance to maximize the efficiency (A_n/A_p , R_L/R_{int}). The electrical current and temperature distribution required in exact method are the current and element lengths in Swanson et al.'s method. The calculation of the mentioned parameters through Swanson et al.'s method is based on solution of energy-balance equation on the interfaces [13], which is different from solution of overall energy-balance equation (4) in exact method.

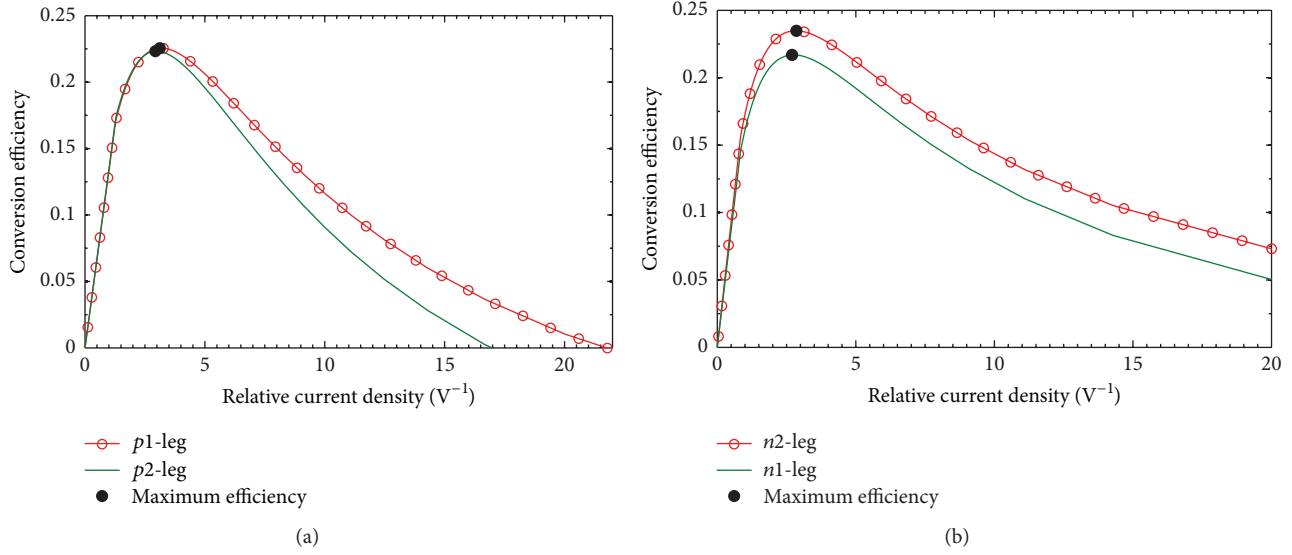


FIGURE 3: Variation of conversion efficiency versus $u(T_h)$ (relative current density at T_h) for (a) $p1$ -leg and $p2$ -leg and (b) $n1$ -leg and $n2$ -leg.

3.3. Compatibility Factor (Exact and Approximate Methods). Compatibility factor is an important parameter which must be considered in addition to FOM in the design of STEGs [18]. Compatibility factor indicates whether the use of two materials in an arrangement has a positive or negative effect on reduced efficiency. The compatibility factor is the relative current density in which reduced efficiency of a material or arrangement is maximized. Reduced efficiency is an intrinsic characteristic of a material which eliminates the effect of temperature range from the total efficiency. It is defined in the following form:

$$\eta_r = \frac{\eta}{\eta_c}, \quad (9)$$

$$\eta_c = \frac{\Delta T}{T_h},$$

where η and η_c are the absolute and Carnot efficiency, respectively. In order to add a new material to an original material or arrangement, it is necessary to calculate the compatibility factor of the two elements. If the compatibility factor of the new material differs by a factor of two or less, reduced efficiency of the resulting arrangement increases, which means the two elements are compatible [32]. Otherwise, it is said that they are incompatible and segmentation leads to a decrease in reduced efficiency. Compatibility factor of each element is the relative current density of the element at its maximum reduced efficiency. In order to calculate compatibility factor, (4) is solved for each material by supposing a boundary condition for y , and the reduced efficiency is obtained. Next, by changing the boundary condition of y , reduced efficiency is maximized. The compatibility factor is the relative current density corresponding to the maximized reduced efficiency. Owing to the fact that compatibility factor is temperature dependent, it is calculated at a specific temperature. Also, the compatibility factor should not change considerably with temperature; such materials are called self-compatible. In approximate method, the calculation of compatibility factor

is the same as exact method but the reduced efficiency is calculated through the following relation [18]:

$$\eta_r = \frac{u(\rho k/\alpha)(1 - u(\rho k/\alpha))}{u(\rho k/\alpha) + 1/ZT}, \quad (10)$$

$$Z = \frac{\alpha^2}{\rho k}.$$

At a specific temperature, the curve of reduced efficiency versus current density is plotted using (10), and then the compatibility factor is obtained.

In this study, the proposed STEGs have been optimally designed to achieve maximum efficiency using both exact and approximate methods (exact and Swanson et al.'s methods). The design and performance characteristics of the optimized STEGs have been calculated using both methods and results have been compared. Compatibility factors of the proposed arrangements have also been calculated through both exact and approximate methods and results have been compared.

4. Results and Discussion

4.1. Analysis of the Proposed Generators. In this paper, two arrangements have been suggested for each n -type and p -type leg using the best available thermoelectric materials. Then, with the combination of them, four STEGs have been proposed. Table 1 shows the arrangements of legs as well as their temperature range. The proposed STEGs have been optimized in order to achieve maximum efficiency. Design and performance characteristics of the optimized STEGs including length of elements, electrical current, cross section ratio, and resistance ratio have been calculated using exact method. The overall length of each leg and the cross section of p -type legs are assumed to be 10 mm and 100 mm², respectively.

Figures 3(a) and 3(b) indicate the efficiency of p -type and n -type legs versus relative current density, respectively,

TABLE 2: Design and performance characteristics of $p1-n1$ and $p1-n2$ generators at maximum efficiency, calculated through both exact and Swanson et al.'s [13] methods. The differences between Swanson et al.'s and exact results are shown in parenthesis. A_p and L are assumed as constant inputs of the optimization process.

Parameters	Swanson method ($p1-n1$)	Exact method ($p1-n1$)	Swanson method ($p1-n2$)	Exact method ($p1-n2$)
L (mm) (input)	10	10	10	10
A_p (mm ²) (input)	100	100	100	100
Calculated Q_{in} (W)	37.61 (4.1)	39.24	38.15 (1.2)	38.63
Calculated Q_{rej} (W)	31.48 (2.9)	30.58	31.13 (4.8)	29.71
Calculated P_e (W)	8.57 (1.03)	8.65	9.12 (2.3)	8.92
Residual power ($Q_{in} - Q_{rej} - P_e$) (W)	-2.43	—	-2.10	—
Calculated peak efficiency, η (%)	22.77 (3.2)	22.06	23.91 (3.6)	23.00
$A_{n,opt}$ (mm ²)	83.49 (7.7)	77.51	92.81 (14.5)	81.08
$L_{p,1}, L_{p,2}, L_{p,3}, L_{p,4}, L_{p,5}$ (mm)	2.656, 3.263, 1.529, 0.808, 1.7350 (5.05)	2.636, 3.199, 1.514, 0.823, 1.827	2.661, 3.262, 1.532, 0.807, 1.728 (5.4)	2.636, 3.199, 1.514, 0.823, 1.827
$L_{n,1}, L_{n,2}, L_{n,3}, L_{n,4}$ (mm)	0.488, 5.716, 2.504, 1.283 (9.12)	0.447, 5.734, 2.543, 1.275	0.533, 6.231, 1.667, 1.559 (8.09)	0.493, 6.240, 1.711, 1.556
I (A)	28.11 (7.1)	30.27	28.75 (5.01)	30.27
$R_{L,opt}$ (m Ω)	10.8 (14.9)	9.4	11.0 (13.4)	9.7

which are calculated using exact method. In this study, absolute values of u and y have been used. Sherman et al. [12] mentioned that if the efficiency changes in the range of 0.3–0.03, the value of u will change in the range of 0.9–3.57 (y : 0.28–1.12). As can be inferred from the figures, the optimum value of u is 2.7 and 2.85 for n -type and 3.125 and 2.95 for p -type, respectively, which shows great agreement with Sherman et al.'s data. The maximum efficiency for the $p1$ -leg and $p2$ -leg equals 22.56% and 22.32%, respectively, while it equals 21.69% and 23.48% for the $n1$ -leg and $n2$ -leg, respectively.

Four generators resulting from combination of the legs have been presented in Tables 2 and 3. The computed design characteristics of the generators at maximum efficiency using the exact method are shown in these tables as well. The highest efficiency is 23.08%, which belongs to the generator resulting from the combination of $p1$ and $n2$, which shows 4.98% increase in comparison with Snyder arrangement which is 18.1% [11]. The $p1-n2$ generator has also been designed for operating between 300 and 973 K in order for making comparison with Fleurial and Caillat's arrangement [15, 33]. The output power, inlet heat, and outlet heat of the mentioned generator are equal to 6.67 W, 31.52 W, and 24.851 W, respectively, in the same temperature range. These values are by far less than those of Fleurial and Caillat's generator at the same temperature range. However, the efficiency of the current generator is by far higher than that of Fleurial and Caillat (i.e., 21.28% compared with 13.29%). The mentioned results are mainly caused by a decrease in thermal conductivity which has been a basis for most of the recent works in the field of new thermoelectric materials especially where nanotechnology is used.

Since the amount of output power is of great importance in most applications, the $p1-n2$ generator has also been designed at maximum power (instead of at maximum efficiency). The results are shown in Table 4.

Nevertheless, it is explained in the following section that such design cannot be an ideal design because the system is not so-called load-following [15]. According to Table 2, the power generated by such generator is 8.92 W at maximum efficiency and 9.33 W at maximum power design. Also, the efficiency reduces from 23.08% to 22.72%, revealing an increase of 4.62% in power in exchange for 1.58% decrease in efficiency. It is remarkable that electrical current has undergone 17.33% increase and the optimum external resistance decreases by 23.71%. Figures 4(a) and 4(b) show the variation of generated power per unit cross section area and the inlet heat flux versus relative current density for p -type and n -type legs, respectively. The solid circles and open triangles show maximum efficiency and maximum power, respectively. Generator's function in load-following and non-load-following mode has been indicated by full lines and dotted lines, respectively. Therefore, the operation point of generator should be selected in fully lined portion of the curve. According to the figures, the design of generator at maximum power results in loss of load-following, while design at maximum efficiency keeps the generator in a range with load-following [15].

4.2. Evaluation of Generators Using Compatibility Factor.

Variations of reduced efficiency with respect to relative current density for n -type and p -type legs at T_{av} have been calculated by exact method and are presented with solid lines in Figures 5 and 6, respectively. The solid circles show the maximum of reduced efficiency. The values of relative current density corresponding to these maximum points represent the compatibility factor of each segment. The curves of p -type and n -type legs reveal that, in general, the compatibility factors of materials are better for p -type than for n -type. However, the curves cannot be used to investigate the whole leg compatibility. This is due to the fact that when a new material is added to an original arrangement,

TABLE 3: Design and performance characteristics of $p2-n1$ and $p2-n2$ generators at maximum efficiency, calculated through both exact and Swanson et al.'s [13] methods. The differences of Swanson et al.'s results compared to the exact ones are shown in parenthesis. A_p and L are assumed as constant inputs of the optimization process.

Parameters	Swanson method ($p2-n1$)	Exact method ($p2-n1$)	Swanson method ($p2-n2$)	Exact method ($p2-n2$)
L (mm) (input)	10	10	10	10
A_p (mm ²) (input)	100	100	100	100
Calculated Q_{in} (W)	37.91 (0.62)	38.15	38.46 (2.4)	37.57
Calculated Q_{rej} (W)	31.55 (5.99)	29.77	31.21 (7.8)	28.94
Calculated P_e (W)	8.58 (2.4)	8.38	9.13 (5.8)	8.63
Residual power ($Q_{in} - Q_{rej} - P_e$) (W)	-2.22	—	-1.88	—
Calculated peak efficiency, η (%)	22.63 (3.0)	21.97	23.74 (3.3)	22.97
$A_{n,opt}$ (mm ²)	83.38 (13.2)	73.65	92.71 (20.3)	77.04
$L_{p,1}, L_{p,2}, L_{p,3}, L_{p,4}, L_{p,5}$ (mm)	2.570, 3.167, 1.050, 1.821, 1.382 (5.11)	2.562, 3.132, 1.042, 1.808, 1.456	2.573, 3.164, 1.052, 1.825, 1.376 (5.5)	2.562, 3.132, 1.042, 1.808, 1.456
$L_{n,1}, L_{n,2}, L_{n,3}, L_{n,4}$ (mm)	0.488, 5.716, 2.504, 1.283 (9.03)	0.447, 5.734, 2.543, 1.275	0.532, 6.232, 1.668, 1.560 (7.99)	0.493, 6.240, 1.711, 1.556
I (A)	28.01 (2.63)	28.76	28.65 (0.4)	28.76
$R_{L,opt}$ (m Ω)	10.9 (7.9)	10.1	11.1 (6.7)	10.4

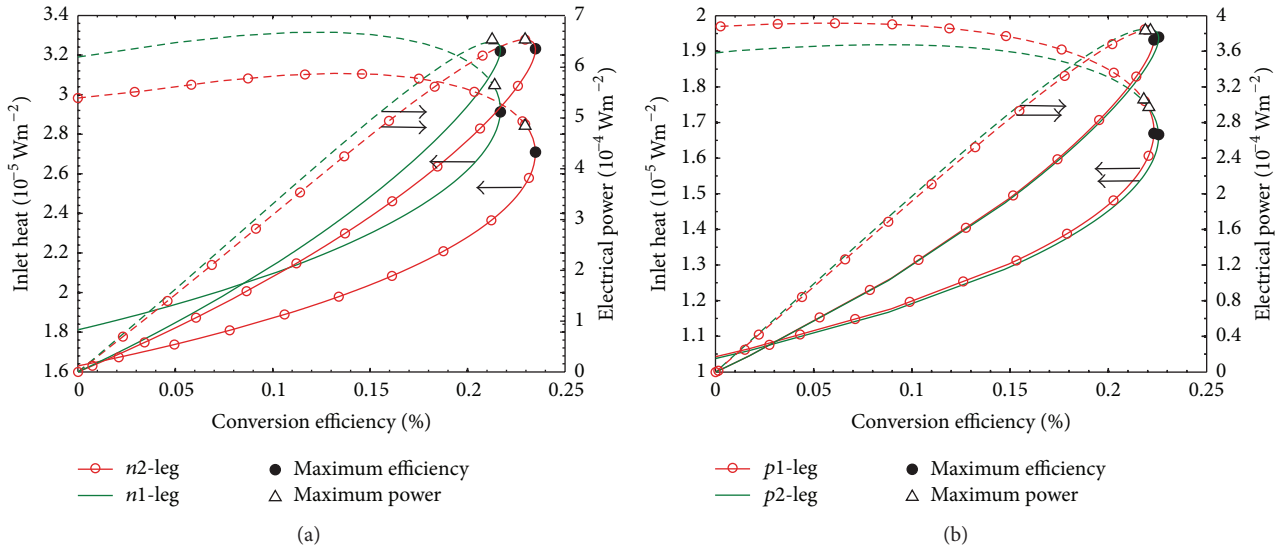


FIGURE 4: Electrical output power per cross section area and input heat flux versus conversion efficiency for (a) $p1$ -leg and $p2$ -leg and (b) $n1$ -leg and $n2$ -leg which have been calculated through exact method.

the compatibility of the original arrangement as a whole and new material must be assessed, but the curves are plotted for each material separately. Therefore, they are only useful for a general assessment of materials' compatibility. In order to clarify the subject, the change of reduced efficiency of legs with increasing number of elements has been shown in Table 5. The table reveals that the materials used in the $p1$ -leg are compatible; and adding material increases the reduced efficiency of the resulting assembly. Also, in $p2$ -leg, the materials are compatible but the first two materials are on the border of compatibility and incompatibility. For the arrangements $n1$ and $n2$, only the first three materials are compatible, and the fourth material is incompatible with them; therefore, adding it to the arrangement leads to

a decrease in the reduced efficiency of the arrangement as a whole. The materials used would be compatible, if the n -legs were used in temperature range of 300 and 1200 K. However, owing to the fact that p -legs have been used in range of 300 and 1300 K, n -legs should be used in the same temperature range to preserve consistency. Our search for a material with a better compatibility factor did not lead to any satisfactory results in the mentioned temperature range. Therefore, these arrangements have been proposed.

4.3. *Evaluation of Approximate Methods.* The optimized generators have also been designed using Swanson et al.'s method at maximum efficiency. The calculated performance and design characteristics are shown in Tables 2 and 3 and

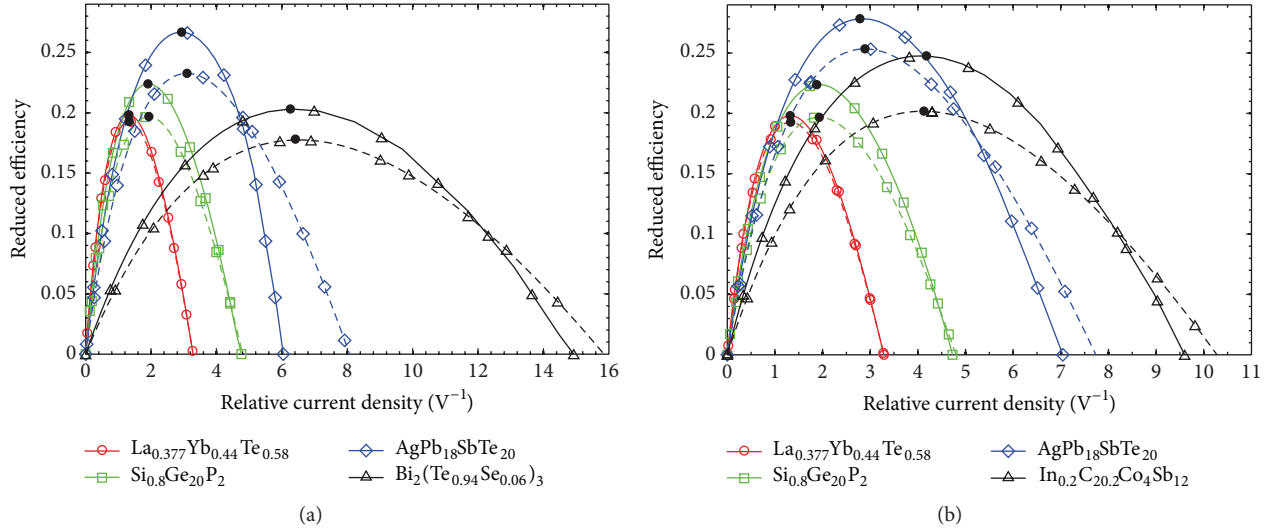


FIGURE 5: Variation of reduced efficiency versus $u(T_{av})$ (relative current density at T_{av}) for the materials used in (a) $n1$ -leg and (b) $n2$ -leg. The solid and dashed lines indicate results of exact and approximate method, respectively.

TABLE 4: Design and performance characteristics of $p1$ - $n2$ generator at maximum output power, calculated through exact method.

Parameters	Exact ($p1$ - $n2$)
L (mm) (input)	10
A_p (mm ²) (input)	100
Calculated Q_{in} (W)	41.07
Calculated Q_{rej} (W)	31.73
Calculated P_e (W)	9.33
Calculated peak efficiency, η (%)	22.72
$A_{n,opt}$ (mm ²)	84.03
$L_{p,1}, L_{p,2}, L_{p,3}, L_{p,4}, L_{p,5}$ (mm)	2.762, 3.274, 1.574, 0.841, 1.831
$L_{n,1}, L_{n,2}, L_{n,3}, L_{n,4}$ (mm)	0.540, 6.521, 1.784, 1.589
I (A)	35.52
$R_{L,opt}$ (m Ω)	7.4

TABLE 5: Reduced efficiency of arrangements with increasing number of elements.

Number of elements	Leg			
	$p1$	$p2$	$n1$	$n2$
1	20.61	24.66	20.32	24.76
2	25.87	24.66	25.35	28.68
3	27.41	26.15	28.42	30.91
4	28.46	27.54	28.19	30.53
5	29.32	29.02	—	—

compared with those of exact method. These tables show that, in Swanson et al.'s method, design and characteristic properties of p -type and n -type legs depend on each other, while in the exact method p -type legs are designed separately and independently of n -type legs. The differences of Swanson et al.'s results compared to exact ones are presented in parenthesis in these tables. The tables indicate that Swanson

et al.'s method could cause a difference of up to 4.1% in inlet heat, 7.8% in outlet heat, 5.8% in generated power, 3.3% in efficiency, 20.3% in n -type leg cross section area, 9.1% in element lengths, 7.1% in current, and 14.0% in external resistance. In these tables, the two highest differences belong to the external resistance and n -type leg cross sections area (i.e., 14% and 20.3%, resp.). Swanson et al. [13] has referred to such differences by optimizing the efficiency for the two following cases: constant $R_L/R = \text{optimum value}$, variable A_n/A_p , and variable R_L/R , constant $A_n/A_p = \text{optimum value}$. In this paper, the two preceding cases have been investigated, in four generators, and the results are shown in Figures 7(a)–7(d), through the curves of efficiency with respect to electrical current. In Swanson et al.'s method, the amount of calculated electrical power is not equal to that of thermal power obtained through satisfaction of the energy-balance equation. This is because of the approximations and use of temperature average properties of materials. Therefore, there exists residual power shown in Tables 2 and 3. The exact method satisfies the overall energy-balance equation completely and thus there is no residual power.

The compatibility factor of the materials used in n -type and p -type legs has also been calculated using the approximate relation (10) and indicated with dashed lines in Figures 5 and 6, respectively. A comparison of results with the ones of exact method reveals that relation (10) yields somewhat exact results and there is not a considerable difference in compatibility factor whereas there is a noticeable difference in reduced efficiency.

5. Conclusion

Four STEGs with the best known thermoelectric materials have been optimized for operating between 300 and 1300 K. The maximum theoretically achievable efficiency has been calculated assuming insulated outside surface area and

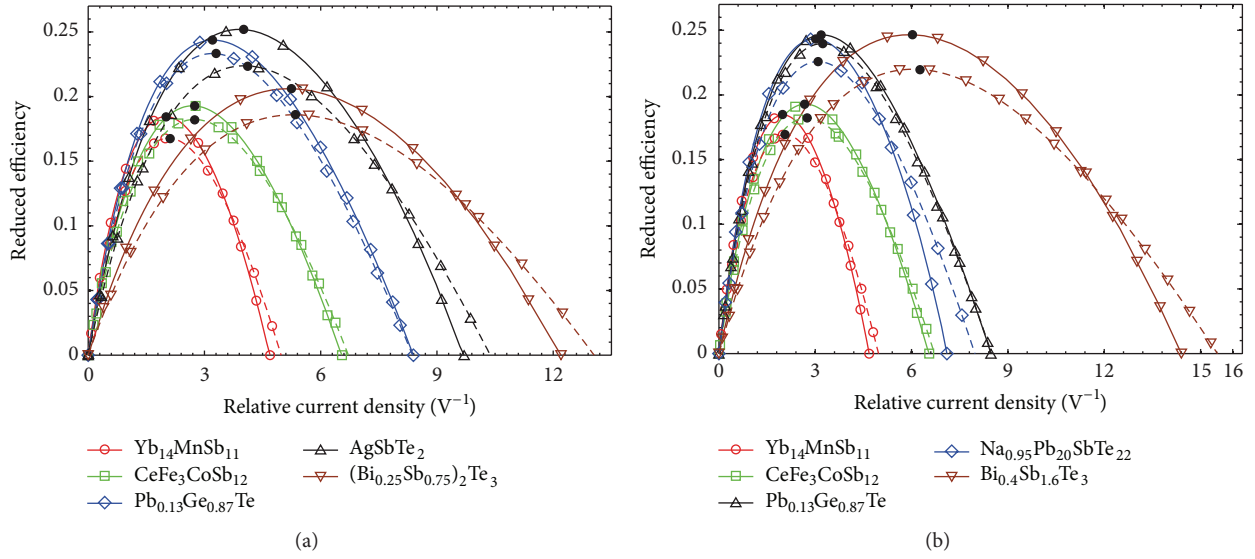


FIGURE 6: Variation of reduced efficiency versus $u(T_{av})$ (relative current density at T_{av}) for the materials used in (a) $p1$ -leg and (b) $p2$ -leg. The solid and dashed lines indicate results of exact and approximate method, respectively.

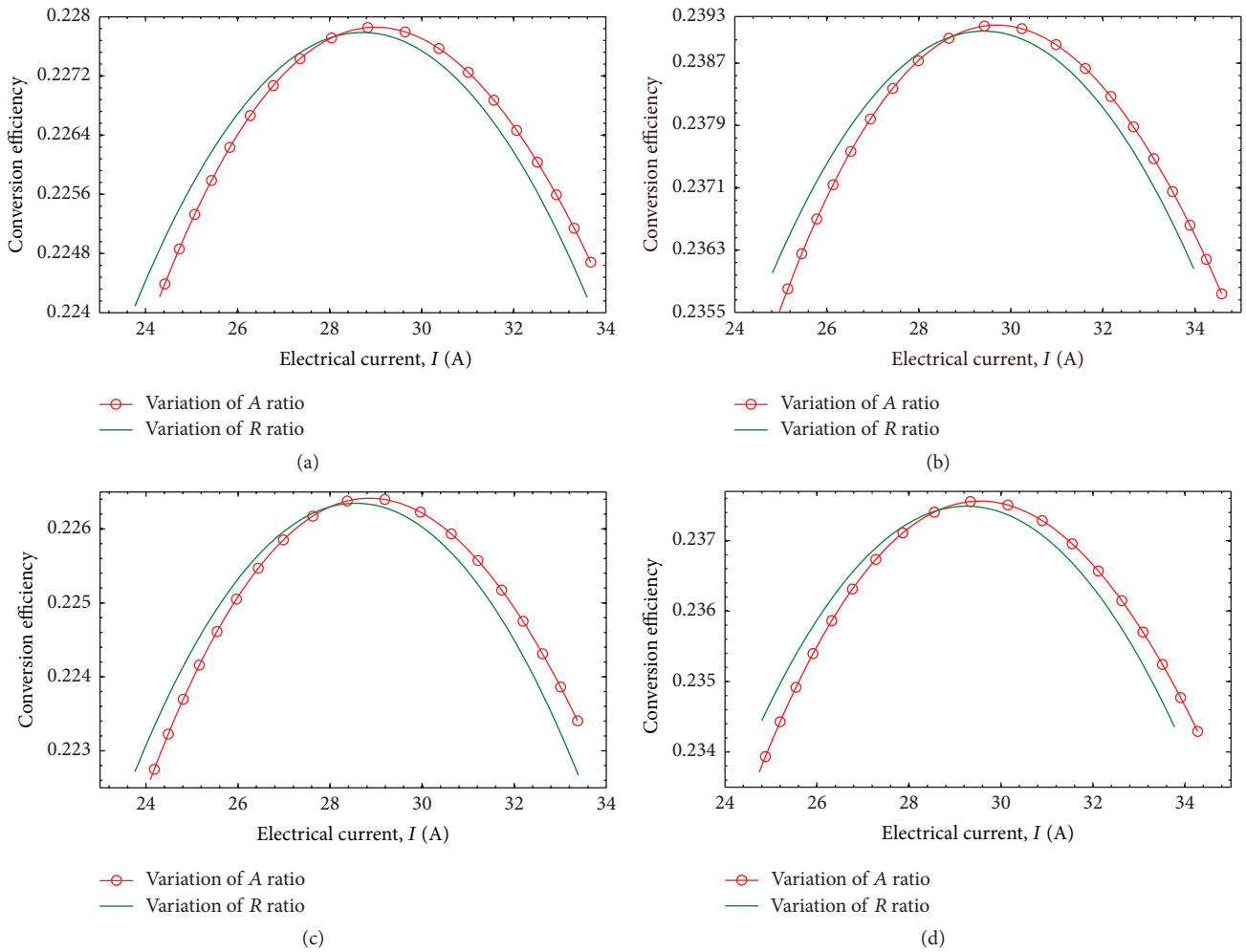


FIGURE 7: Variation of efficiency with respect to electrical current for the two following cases: constant $R_L/R = \text{optimum value}$, variable A_n/A_p , and variable R_L/R , constant $A_n/A_p = \text{optimum value}$. (a)-(d) represent $p1$ - $n1$, $p1$ - $n2$, $p2$ - $n1$, and $p2$ - $n2$ generators, respectively.

negligible contact resistance. Design and performance characteristics of the generators have been calculated at maximum efficiency using exact and Swanson et al.'s method. Maximum efficiency of 23.08% has been obtained for the best arrangement, which shows 4.98% increase in comparison with the best of the previous published results in a similar temperature range (298 and 1273 K). Compatibility factor of the arrangements has been calculated through both exact and Swanson et al.'s method. Satisfactory compatibility has been observed for the materials in each arrangement. All the results of exact and Swanson et al.'s method have been compared. It has been observed that Swanson et al.'s method could cause a difference of up to 20% in some characteristics despite its sufficiently good results in calculation efficiency. Enhancing thermoelectric efficiency opens the way to generate electrical power especially by using waste heat as source. Owing to the great deal of attempt and investigation to improve thermoelectric properties, especially based on nanotechnology, this direct energy conversion method and consequently the energy optimization are awaiting a bright future.

Nomenclature

Variables

A :	Cross section area (m^2)
I :	Electrical current (A)
J :	Electrical current density (Am^{-2})
k :	Thermal conductivity ($\text{Wm}^{-1}\text{K}^{-1}$)
L :	Length of legs (m)
$L_{p,1}, \dots, L_{n,1}, \dots$:	Length of segments (m)
P_e :	Output electrical power (W)
Q :	Heat power (W)
R :	Electrical resistance (Ω)
T :	Temperature (K)
u :	Relative electrical current density (V^{-1})
W :	Work output (W)
x :	Coordinate originated from hot source (m)
Z :	Figure of merit (FOM) (K^{-1})
ZT :	Dimensionless figure of merit.

Greek Symbols

α :	Seebeck coefficient (VK^{-1})
η :	Efficiency
η_c :	Carnot efficiency
η_r :	Reduced efficiency
γ :	Thomson coefficient (VK^{-1})
π :	Peltier coefficient (V)
ρ :	Electrical resistivity ($\Omega\cdot\text{m}$).

Scripts

$'$:	Derivative with respect to x
av:	Average
c:	Cold source
h:	Hot source

in:	Input
int:	Internal
j :	Index for segment number
L :	Electrical load
n :	n -leg
opt:	Optimum
p :	p -leg
rej:	Reject or output.

Competing Interests

The authors declare that they have no competing interests.

References

- [1] S. B. Riffat and X. Ma, "Thermoelectrics: a review of present and potential applications," *Applied Thermal Engineering*, vol. 23, no. 8, pp. 913–935, 2003.
- [2] K. Yazawa and A. Shakouri, "Thermoelectric topping cycles with scalable design and temperature dependent material properties," *Scripta Materialia*, vol. 111, pp. 58–63, 2016.
- [3] H. Tian, X. Sun, Q. Jia, X. Liang, G. Shu, and X. Wang, "Comparison and parameter optimization of a segmented thermoelectric generator by using the high temperature exhaust of a diesel engine," *Energy*, vol. 84, pp. 121–130, 2015.
- [4] J. P. Heremans, V. Jovovic, E. S. Toberer et al., "Enhancement of thermoelectric efficiency in PbTe by distortion of the electronic density of states," *Science*, vol. 321, no. 5888, pp. 554–557, 2008.
- [5] G. J. Snyder and E. S. Toberer, "Complex thermoelectric materials," *Nature Materials*, vol. 7, no. 2, pp. 105–114, 2008.
- [6] L. I. Soliman, M. M. Nassary, H. T. Shaban, and A. S. Salwa, "Influence of Se on the electron mobility in thermal evaporated $\text{Bi}_2(\text{Te}_{1-x}\text{Se}_x)_3$ thin films," *Vacuum*, vol. 85, no. 3, pp. 358–364, 2010.
- [7] L. T. Hung, N. Van Nong, G. J. Snyder et al., "High performance p-type segmented leg of misfit-layered cobaltite and half-Heusler alloy," *Energy Conversion and Management*, vol. 99, pp. 20–27, 2015.
- [8] G. Chen, M. Dresselhaus, and Z. Ren, "Nanocomposites with high thermoelectric figures of merit," US Patent App 20, 090/068, 465, 2008.
- [9] Z. Ren, B. Poudel, G. Chen, Y. Lan, D. Wang, and Q. E. A. Hao, "Methods for high figure-of-merit in nanostructured thermoelectric materials," US Patent App. 11/949, 353, 2007.
- [10] Y. S. Kang, M. Niino, I. A. Nishida, and J. Yoshino, "Development and evaluation of 3-stage segmented thermoelectric elements," in *Proceedings of the 17th International Conference on Thermoelectrics (ICT '98)*, pp. 429–432, May 1998.
- [11] G. J. Snyder and T. Caillat, "Using the compatibility factor to design high efficiency segmented thermoelectric generators," *Materials Research Society Symposium Proceedings*, vol. 793, pp. 37–42, 2003.
- [12] B. Sherman, R. R. Heikes, and R. W. Ure Jr., "Calculation of efficiency of thermoelectric devices," *Journal of Applied Physics*, vol. 31, no. 1, pp. 1–16, 1960.
- [13] B. W. Swanson, E. V. Somers, and R. R. Heikes, "Optimization of a sandwiched thermoelectric device," *Journal of Heat Transfer*, vol. 83, no. 1, pp. 77–82, 1961.
- [14] R. G. Moore, "Exact computer solution of segmented thermoelectric devices," *Advanced Energy Conversion*, vol. 2, pp. 183–195, 1962.

- [15] M. S. El-Genk and H. H. Saber, "High efficiency segmented thermoelectric unicouple for operation between 973 and 300 K," *Energy Conversion and Management*, vol. 44, no. 7, pp. 1069–1088, 2003.
- [16] C. Hadjistassou, E. Kyriakides, and J. Georgiou, "Designing high efficiency segmented thermoelectric generators," *Energy Conversion and Management*, vol. 66, pp. 165–172, 2013.
- [17] T. Ming, Y. Wu, C. Peng, and Y. Tao, "Thermal analysis on a segmented thermoelectric generator," *Energy*, vol. 80, pp. 388–399, 2015.
- [18] T. Ursell and G. Snyder, "Compatibility of segmented thermoelectric generators," in *Proceedings of the 21st International Conference on Thermoelectrics (ICT '02)*, pp. 412–417, Long Beach, Calif, USA, 2002.
- [19] O. Yamashita, S. Tomiyoshi, and K. Makita, "Bismuth telluride compounds with high thermoelectric figures of merit," *Journal of Applied Physics*, vol. 93, no. 1, pp. 368–374, 2003.
- [20] S. Fan, J. Zhao, J. Guo, Q. Yan, J. Ma, and H. H. Hng, "P-type Bi_{0.4}Sb_{1.6}Te₃ nanocomposites with enhanced figure of merit," *Applied Physics Letters*, vol. 96, no. 18, Article ID 182104, 2010.
- [21] O. Yamashita and S. Tomiyoshi, "High performance n-type bismuth telluride with highly stable thermoelectric figure of merit," *Journal of Applied Physics*, vol. 95, no. 11, pp. 6277–6283, 2004.
- [22] M. Subramanian, T. He, and J. Krajewski, "High performance thermoelectric materials and their method of preparation," US Patent Application 12/785,605, 2010.
- [23] H. Wang, J.-F. Li, M. Zou, and T. Sui, "Synthesis and transport property of AgSbTe₂ as a promising thermoelectric compound," *Applied Physics Letters*, vol. 93, no. 20, Article ID 202106, 2008.
- [24] P. F. P. Poudeu, J. D'Angelo, A. D. Downey, J. L. Short, T. P. Hogan, and M. G. Kanatzidis, "High thermoelectric figure of merit and nanostructuring in bulk p-type Na_{1-x}Pb_mSb_yTe_{m+2}," *Angewandte Chemie-International Edition*, vol. 45, no. 23, pp. 3835–3839, 2006.
- [25] K. F. Hsu, S. Loo, F. Guo et al., "Cubic AgPb_mSb_yTe_{2+m}: bulk thermoelectric materials with high figure of merit," *Science*, vol. 303, no. 5659, pp. 818–821, 2004.
- [26] Y. Gelbstein, B. Dado, O. Ben-Yehuda, Y. Sadia, Z. Dashevsky, and M. P. Dariel, "Highly efficient Ge-rich Ge_xPb_{1-x}Te thermoelectric alloys," *Journal of Electronic Materials*, vol. 39, no. 9, pp. 2049–2052, 2010.
- [27] X. W. Wang, H. Lee, Y. C. Lan et al., "Enhanced thermoelectric figure of merit in nanostructured n-type silicon germanium bulk alloy," *Applied Physics Letters*, vol. 93, no. 19, Article ID 193121, 2008.
- [28] J.-P. Fleurial, A. Borshchevsky, T. Caillat, D. T. Morelli, and G. P. Meisner, "High figure of merit in Ce-filled skutterudites," in *Proceedings of the 15th International Conference on Thermoelectrics (ICT '96)*, pp. 91–95, March 1996.
- [29] A. F. May, J.-P. Fleurial, and G. J. Snyder, "Optimizing thermoelectric efficiency in La_{3-x}Te₄ via Yb substitution," *Chemistry of Materials*, vol. 22, no. 9, pp. 2995–2999, 2010.
- [30] S. R. Brown, S. M. Kauzlarich, F. Gascoin, and G. Jeffrey Snyder, "Yb₁₄MnSb₁₁: new high efficiency thermoelectric material for power generation," *Chemistry of Materials*, vol. 18, no. 7, pp. 1873–1877, 2006.
- [31] C. A. Domenicali, "Stationary temperature distribution in an electrically heated conductor," *Journal of Applied Physics*, vol. 25, no. 10, pp. 1310–1311, 1954.
- [32] G. J. Snyder and T. S. Ursell, "Thermoelectric efficiency and compatibility," *Physical Review Letters*, vol. 91, no. 14, 2003.
- [33] J.-P. Fleurial, A. Borshchevsky, T. Caillat, and R. Ewell, "New materials and devices for thermoelectric applications," in *Proceedings of the 32nd Intersociety Energy Conversion Engineering Conference (IECEC '97)*, vol. 2, pp. 1080–1085, Honolulu, Hawaii, USA, August 1997.

Research Article

Power Prediction and Technoeconomic Analysis of a Solar PV Power Plant by MLP-ABC and COMFAR III, considering Cloudy Weather Conditions

M. Khademi,¹ M. Moadel,² and A. Khosravi³

¹Department of Applied Mathematics, Islamic Azad University, South Tehran Branch, No. 209, North Iranshahr Street, Tehran 11365-4435, Iran

²Department of Energy Systems Engineering, Islamic Azad University, South Tehran Branch, No. 209, North Iranshahr Street, Tehran 11365-4435, Iran

³Islamic Azad University, South Tehran Branch, No. 209, North Iranshahr Street, Tehran 11365-4435, Iran

Correspondence should be addressed to M. Khademi; khademi@azad.ac.ir

Received 4 December 2015; Revised 24 January 2016; Accepted 31 January 2016

Academic Editor: Pouria Ahmadi

Copyright © 2016 M. Khademi et al. This is an open access article distributed under the Creative Commons Attribution License, which permits unrestricted use, distribution, and reproduction in any medium, provided the original work is properly cited.

The prediction of power generated by photovoltaic (PV) panels in different climates is of great importance. The aim of this paper is to predict the output power of a 3.2 kW PV power plant using the MLP-ABC (multilayer perceptron-artificial bee colony) algorithm. Experimental data (ambient temperature, solar radiation, and relative humidity) was gathered at five-minute intervals from Tehran University's PV Power Plant from September 22nd, 2012, to January 14th, 2013. Following data validation, 10665 data sets, equivalent to 35 days, were used in the analysis. The output power was predicted using the MLP-ABC algorithm with the mean absolute percentage error (MAPE), the mean bias error (MBE), and correlation coefficient (R^2), of 3.7, 3.1, and 94.7%, respectively. The optimized configuration of the network consisted of two hidden layers. The first layer had four neurons and the second had two neurons. A detailed economic analysis is also presented for sunny and cloudy weather conditions using COMFAR III software. A detailed cost analysis indicated that the total investment's payback period would be 3.83 years in sunny periods and 4.08 years in cloudy periods. The results showed that the solar PV power plant is feasible from an economic point of view in both cloudy and sunny weather conditions.

1. Introduction

Photovoltaic cells collect sunlight and convert it to electrical energy, which is the most convenient way to utilize solar energy. The performance of a PV panel is strongly dependent on the availability of solar irradiance at the required location, PV panel temperature, and other environmental conditions. Thus, reliable knowledge and understanding of the PV panels' performance under different operating conditions are of great importance for accurate prediction of their energy output and correct site selection [1].

In recent years, large numbers of research projects have been carried out relating to the prediction of a solar PV system's efficiency and optimizing the effective parameters with the use of artificial intelligence techniques [2]. Some studies

have been done in order to investigate the environmental factors which affect the current-voltage ($I-V$) characteristics of PV modules based on the simultaneous measurement of the open-circuit voltage V_{oc} as a function of a slowly varying light intensity [3]. Bayrakci et al. [4] analyzed the effect of temperature on the performance of PV modules. There are also some power efficiency models [5] that can predict the real dynamic or average performance of a PV system under variable climatic conditions [6].

The main disadvantage of mathematical modeling is the dependency of the model's parameters on operating conditions; that is, a given set of operating conditions needs a corresponding set of parameters. This weak point largely limits the application of the model. Additionally, there is no specific mathematical model for the prediction of PV



FIGURE 1: University of Tehran's Photovoltaic Plant Complex (Source: <http://pvlab.ut.ac.ir>).

output in cloudy conditions. Many artificial neural networks (ANNs), which use only one algorithm for different weather conditions, have been developed in order to find the optimum operating point of PV panels [7–9]. The research that has been carried out in the field of ANNs shows that with more accurate data classification and the development of a special algorithm for each classification, better results can be achieved.

By increasing the forecast accuracy of output power of the solar panels, better control could be achieved with greater precision. This would allow us to increase the energy efficiency of photovoltaic panels and make them more cost effective [10, 11]. The results could be used in order to build an intelligent controller, which could find the maximum power point (MPP) [12–14]. The controller would find the MPP according to the ANN prediction when the radiation decreases caused by sudden cloud coverage. The regions with wet climatic conditions with cloudy skies, such as the Mediterranean or the north of Iran, are suitable for study by this approach in order to optimize the output energy prediction of the panels.

The main objective of this study was to pursue a simplified simulation model, with acceptable levels of precision, in order to predict the output power of PV modules under different operating conditions, giving particular consideration to the sudden occurrence of clouds. For this purpose, the classification method was applied and data was divided into two groups: cloudy data and sunny data. The financial indexes of a 20-year life cycle of the PV power plant, considering sunny days and cloudy periods, were calculated and compared. In this paper, MLP-ABC algorithms were used to predict the output energy of solar panels. The obtained results show that these methods can be used instead of time-consuming experimental tests to determine the PV panels' output energy with a desirable level of accuracy. A detailed economic analysis was also carried out using COMFAR III software.

2. Material and Method

2.1. Data. Data was measured and registered by data loggers at five-minute intervals and was taken from the Tehran University Photovoltaic Power Plant, located in Tehran, Iran,

at a longitude of $N^{\circ} 37.51$, latitude of $E^{\circ} 47.35$, and an altitude of 1548 meters (see Figure 1).

In this study, ambient temperature, relative humidity, incoming radiation, and PV output power between September 22nd, 2012, and January 14th, 2013, was used. The validation test was done on the data to verify the accuracy of the data's registration. To accomplish this, incoming radiations were compared with extraterrestrial radiation. The measured power was integrated to calculate the total obtained energy within each day and the nominal power values of PV modules were then compared to one another.

3. MLP (Multilayer Perceptron) Neural Network

An MLP neural network was used for data classification. MLPs are composed of input layers, hidden layers, and output layers, which contain certain neurons (see Figure 2). This MLP build, to calculate the power of the solar array, had an output layer comprising of two neurons for calculating the MPP that represent the output voltage and current, corresponding to the maximum power point of the array. We used 215 samples for training and 104 samples for testing the network. In the MLP neural network training process for data classification categories, the ultimate goal is to find the best neural network weights that could be terminated to the smallest Mean Square Error (MSE). In this paper, the reduced gradient method was proposed for finding the optimal weights for the neural network. The outputs corresponding to these inputs are compared with outputs from the network. If the difference between these two values is lesser, the network will be better trained.

4. MLP-ABC (Multilayer Perceptron Neural Network with ABC Algorithm)

The bee colony algorithm was proposed in 2005 by Karaboga. This algorithm was inspired by the exploratory behavior of bee colonies, which is similar to other intelligent group methods. It uses a collection of certain individuals within a group that alone have not been specifically intelligent.

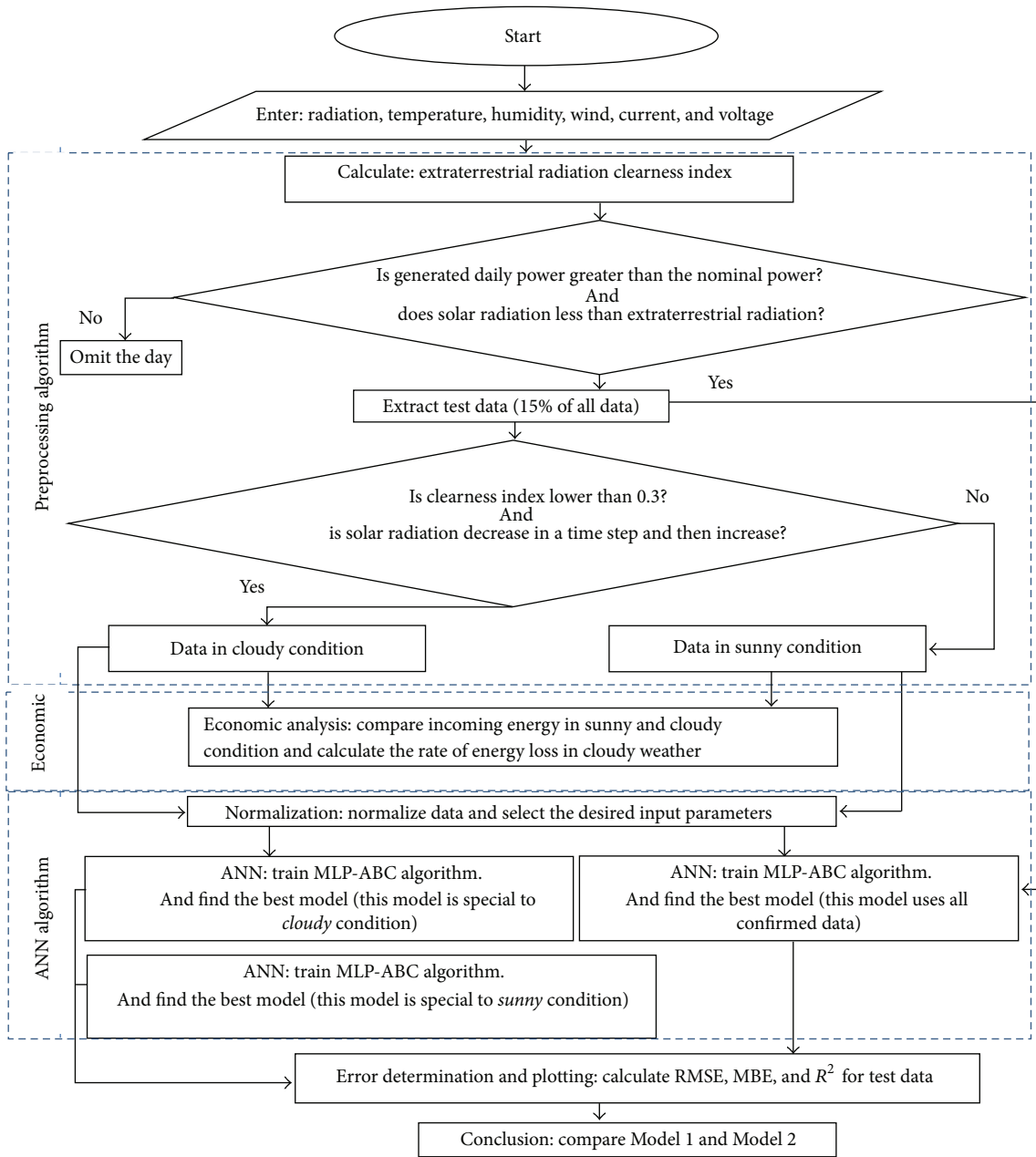


FIGURE 2: Data selection method, preparation for feed-forward neural network, and output result.

Both employed and scout bees work together to find the best solution to the problems. The first one works on the current solution and those around it hoping for an improved result. In the case of no acceptable result, an employed bee becomes a scout and tries to look for another solution in areas farther away. The ABC algorithm is used to solve continuous optimization problems and find the optimum of a function or a combination of multiple scalar functions [15]. The main steps of the ABC algorithm are used as per Aryan et al. [16].

MLP finds its best weights via a gradient descent approach, in which they are computed by backpropagation of errors (different between the network outputs and the desired ones) through the network. However, since it is

a problem of optimization, ABC can be utilized instead of the backpropagation approach. In MLP-ABC, weights are computed by collection of bee agents. They look for the optimum combination of weights in the solution space that results in the best network for the problem.

In order to apply the MLP-ABC model, input parameters are air temperature ($^{\circ}\text{C}$), irradiance (W/m^2), and relative humidity (%) and the output is power. The model consists of two hidden layers. The first layer has four neurons and the second has two neurons.

4.1. The Underlying Assumption and Data Selection. Determining the cloudiness of the sky requires complex and costly

TABLE 1: The statistical classification of cloud database.

Criteria	Power (W)	Solar radiation (W/m ²)	Ambient temperature (°C)	Relative humidity (%)
Average	841	99.8	17.05	44.73
Maximum	2724	499.7	30.40	99.9
Minimum	0	5.03	-5.1	21.35
Standard deviation	718.7	86.3	7.83	18.16

devices. However, as it is well known, the incoming solar radiation is directly related to the level of cloudiness. The clearness index (K_t) is the criteria (amount of the total solar radiation on a horizontal surface at the surface of the Earth, divided by the corresponding irradiance available outside of the atmosphere) for determining the sudden cloud appearances. The key point is that the clear index changes during a sunny day. For instance, the color index is 0.25 at the 7:00 solar time, but it becomes 0.65 at the 12:00 solar time. The average of K_t was therefore calculated for different times in a day. It is assumed that in any given moment, whenever K_t becomes 40% lower than the long-term average of K_t , it is considered that cloud coverage is occurring.

As a more precise criterion, if, in a short time period (less than 5 minutes), the irradiance decreases and then increases, this time period is supposed to be the shade effect on the photovoltaic panel. This assumption may lead to errors in determining the correct time of sudden clouds. Dust, fleeting shadows, and other factors could also cause such situations. To minimize this error, both of the above criteria were used simultaneously. This means that whenever K_t decreases while the amount of radiation fluctuates, the conditions are considered to be cloudy. With regard to this fact, 3,090 sets of data demonstrated cloudy conditions. However, since the aim was to predict the effect of cloudy conditions on decreasing irradiance and output of the panel, the assumption is acceptable.

Table 1 indicates the statistical classification of cloud databases. Daily data analysis indicates that in days of clear sky with neither cloud nor dust, solar radiation at 12:00 (which is considered as the maximum irradiance that could be achieved) varies between 850 W and 1100 W. The data during cloudy days shows the maximum irradiance as 499.7 W, which indicates the impact of clouds on the incidental radiation. Consequently, when the irradiance is associated with abnormal fluctuation, it could be considered the result of cloud occurrence over the panel. The idea of this research is not only to forecast the output power and energy of PV panels, but also to build a control system for these conditions. It could be a great help to optimize output power of PV panels when sudden cloud coverage occurs.

5. Data Preparation

The data was normalized between 0 and 1 for better network learning by the following equation:

$$F(x) = \frac{X - X_{\min}}{X_{\max} - X_{\min}}, \quad (1)$$

TABLE 2: Comparison of results between two conditions (COMFAR's report).

Economic index	Model #1	Model #2
Total fixed investment (\$)	150000000	150000000
Net present value (NPV) (\$) (discounting rate: 4%)	10641,71	9914,05
Internal rate of return (IRR)	35,13%	32,25%
Break-even ratio (%)	17.40%	18.29%
Normal payback period	3.83 years	4.08 years
Dynamic payback period	4.07 years	4.36 years

where $F(x)$ indicates the normalized value and x indicates the actual value. The data was gathered over approximately four months. However, after applying data preprocessing, only 6,895 collections of "sunny" data and 3,090 collections of "cloudy" data remained for creating the MLP-ABC and 680 pieces of data for the testing of the networks. The mean absolute percentage error (MAPE) was used to compare the models. It is a measure of the accuracy of a method for constructing fitted time series values in statistics, specifically in trend estimation [17]. It usually expresses accuracy as a percentage which is defined as follows:

$$\text{MAPE} = \frac{1}{N} \sum_{i=1}^N \frac{|X_i - x_i|}{x_i}. \quad (2)$$

Mean bias error (MBE) and correlation coefficient (R^2) were calculated by the following:

$$\text{MBE} = \sum_{i=1}^N \frac{(X_i - x_i)}{x_i}, \quad (3)$$

$$R^2 = \frac{\sum_{i=1}^N (x_i - \bar{X})(X_i - \bar{X})}{\left(\sqrt{\sum_{i=1}^N (x_i - \bar{X})^2}\right) \times \left(\sqrt{\sum_{i=1}^N (X_i - \bar{X})^2}\right)}.$$

6. Economic Analysis

In this case study, the lifetime economic analyses of PV panels using MLP-ABC algorithms for sunny and cloudy periods were compared.

Net present value (NPV), internal rate of return (IRR), payback period (PBP), and the balance sheet of the project were prepared according to accepted standards based on a 20-year useful life. The details can be found in the full version of COMFAR's report; however, a brief summary is presented in Table 2.

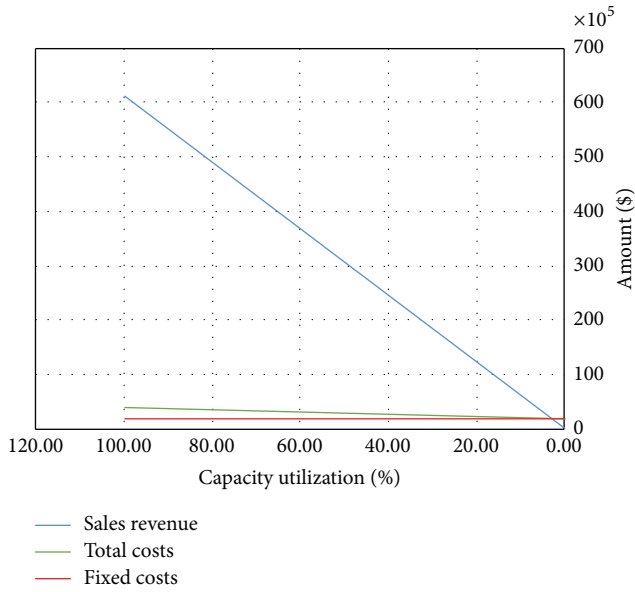


FIGURE 3: Break-even analysis for Model #1.

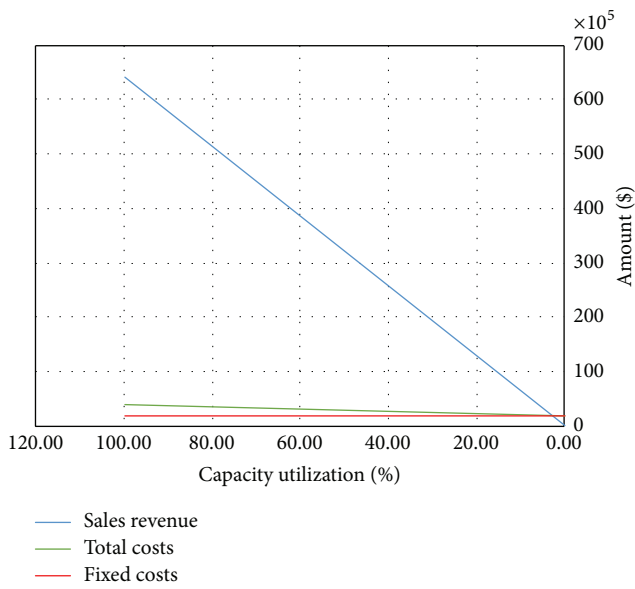


FIGURE 4: Break-even analysis for Model #2.

A useful tool in tracking the cash flow of a business is a break-even analysis. This point is important to determine the price of power in order for the PV to still generate a contribution. The break-even analysis of the investment is performed to determine how many years it takes to generate enough contribution to cover the fixed and variable costs [18]. As the goal is to lower the break-even point and generate profit, it is important to understand this concept. Figures 3 and 4 show the break-even analysis for cloudy periods and sunny days, respectively. In this study, the best efficiency points (BEP) for sunny and cloudy periods are 17.40% and 18.29%, respectively.

The internal rate of return, or discounted cash flow rate of return, offers analysts a way to quantify the rate of return provided by an investment. The COMFAR report shows that

TABLE 3: The generated error in PV panels' power prediction using MLP-ABC.

Model number	Model	MAPE (%)	R ² (%)	MBE (W)
1	Sunny and cloudy (separately)	3.7	94.7	3.1
2	All conditions together	4.7	83.1	9.5

the project is sufficiently feasible as it generates an IRR of 35.13% for sunny days. This is considered an attractive rate of return. The project IRR remains attractive even for the cloudy days as 32.25%. Ultimately, IRR gives an investor the means to compare alternative investments based on their yield.

The panels' output power under cloudy conditions was measured and recorded. The effective clouds on the panel were divided into two categories: (1) clouds that cover the sky and have an effect on the panel for more than 2 hours and (2) parts of clouds that shade the panels for only a moment or several minutes (see Figure 5).

7. Results and Discussion

This study proposes an analysis to exhibit what happens when clouds pass over a solar power plant. The economic analysis, which is presented throughout this study, demonstrates the economic losses caused by sudden cloud coverage and shadows over the panel.

In this research, the effect of cloudy sky conditions on the energy produced by the panels is investigated. The energy generated by the panels during cloudy and sunny climatic conditions was separately predicted by artificial neural methods (MLP-ABC).

Two separate models were developed in different ways for the cloudy and sunny weather conditions. Error calculation and the evaluation of results showed that the first model for different conditions could significantly reduce errors (Table 3).

As mentioned, a more accurate output energy prediction of PV panels could increase the precision of energy supply planning and the design accuracy of control systems. Figures 6, 7, 8, and 9 show the output power prediction of PV panels using the referred methods.

Figures 6 and 8 show the comparison between the predicted power by Model 1 and the measured power. As shown, this model also tracks the fluctuations of the clouds. Looking on a precise level, small fluctuations have occurred in the measured data where the power gets close to its maximum level. The developed model faces some difficulties in tracking these fluctuations. However, these fluctuations are not caused by cloud or external factors, and their value is very low. Thus, it is reasonable to ignore it.

Comparisons between Figures 7 and 9 show the effect of privatization data in order to reduce errors for sunny and cloudy conditions. The method that was demonstrated in the economic analysis section was used to determine the energy loss. Data was collected from September 22nd, 2012, to January 14th, 2013.

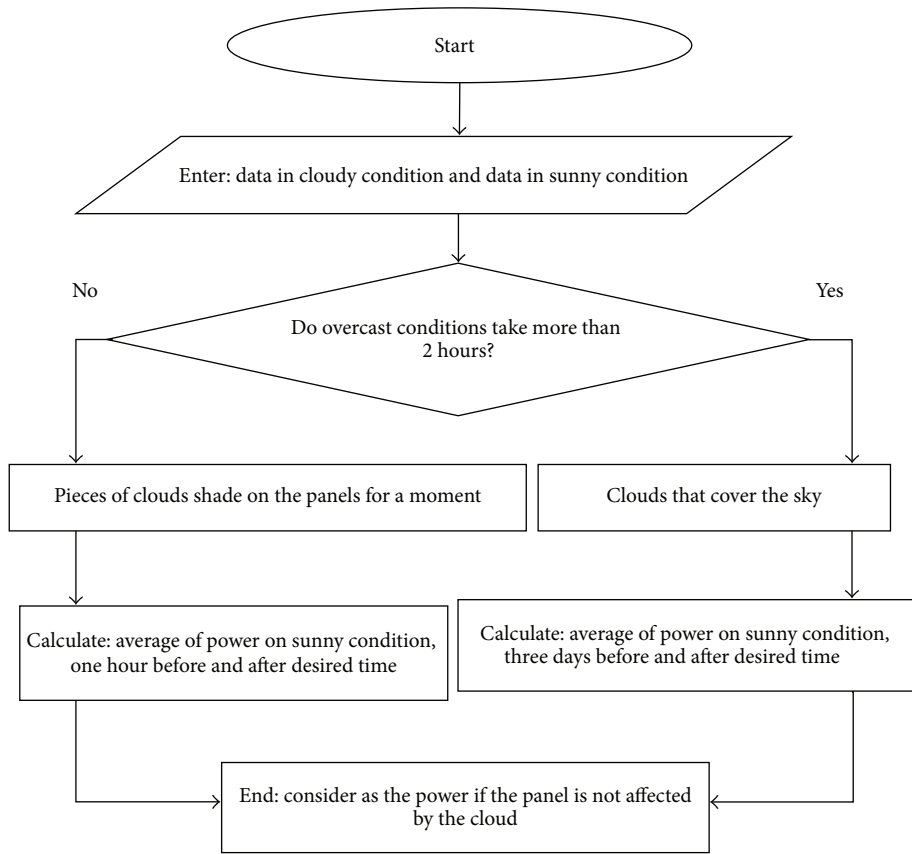


FIGURE 5: The method of determining the amount of power generated if the panel is not affected by clouds.

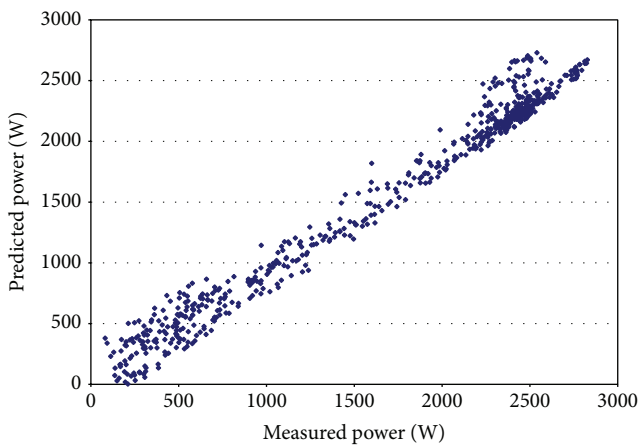


FIGURE 6: Output power prediction for Model #1, which selects sunny and cloudy data randomly.

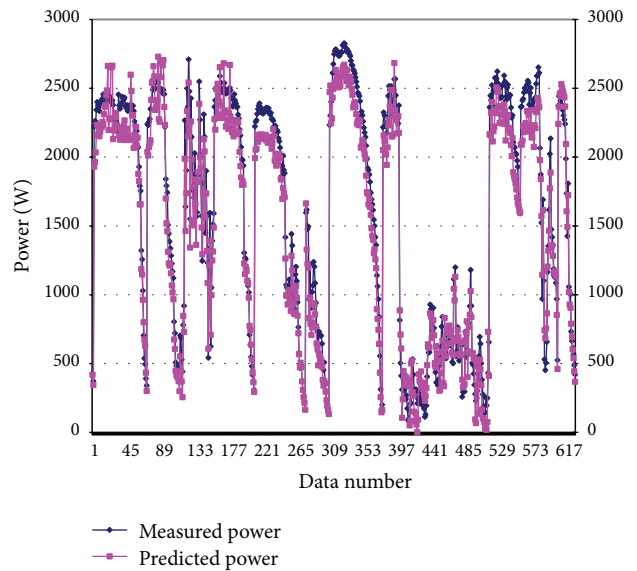


FIGURE 7: Output power prediction for Model #1, which selects sunny and cloudy data randomly.

8. Conclusions

In this paper, the output energy of a 3.2kW PV solar power plant was predicted using an MLP-ABC algorithm and the results were compared with the experimental data. The ambient temperature, irradiance on the horizontal surface, and PV power (by multiplying current and voltage) were collected in the photovoltaic laboratory of Tehran University between September 22nd, 2012, and January 14th, 2013. 10,665

pieces of data were measured at five-minute intervals (over approximately 35 days) after preprocessing.

To improve the performance of the neural network, the sunny days were separated from the cloudy days. For clearness index values less than 0.3, the day was considered as

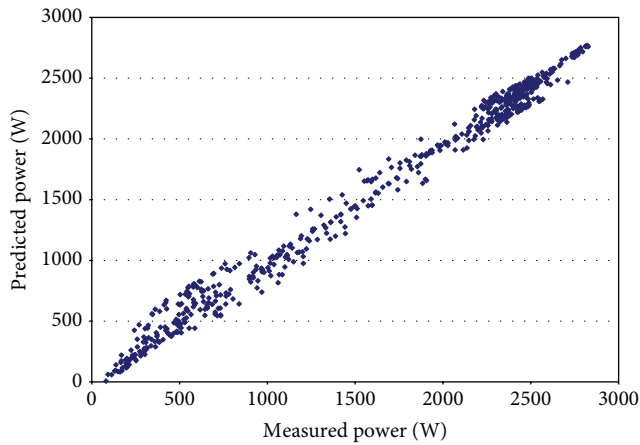


FIGURE 8: Output power prediction for Model #2, which selects sunny and cloudy data separately.

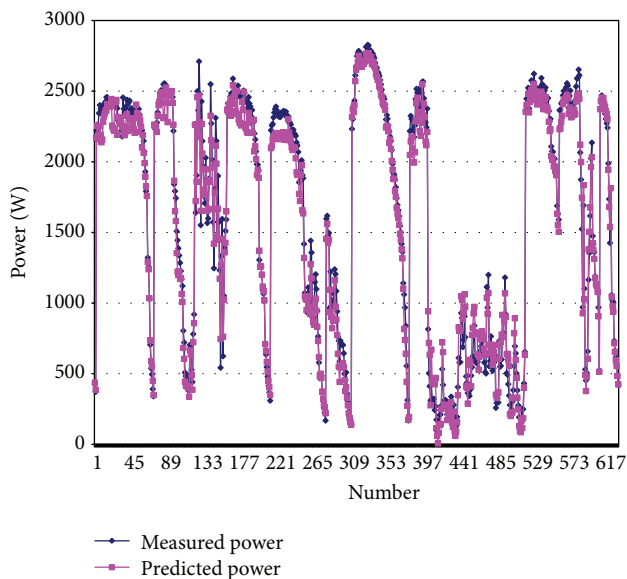


FIGURE 9: Output power prediction for Model #2, which selects sunny and cloudy data separately.

sunny and if radiation fluctuation over a short time interval occurred, it was considered as cloudy time.

The output energy was predicted by two methods. In the first method, all sunny and cloudy data were used and acceptable results were obtained (MAPE = 4.7%, $R^2 = 83.1\%$, MBE = 9.5). In the second method, forecasting precision was improved significantly by separating the sunny and cloudy data (MAPE = 3.7%, $R^2 = 94.7\%$, MBE = 3.1).

The hypothesis was that neural network data classifications improve this model's performance. It has been concluded that with the weather forecast and the separation of different weather conditions, output power prediction can be done more accurately.

Within the period of this study, the solar power plant produced approximately 5237 kWh/year of electricity in sunny weather conditions and 924 kWh/year in cloudy weather conditions, with the energy loss due panel shading around 293 kWh/year.

The results show that the project is feasible because of IRRs of 35.13% and 32.25% (for sunny and cloudy periods, resp.). These are considered to be attractive rates of return in capital markets. The investment has a payback period of 3.83 years in Model #1 and 4.08 years in Model #2.

Conflict of Interests

The authors declare that there is no conflict of interests regarding the publication of this paper.

Acknowledgments

This paper is based up on a research work supported by the Research Council of the Islamic Azad University South Tehran Branch (Contract no. 812). The authors are also grateful to Dr. Farzad Jafarkazemi for his academic advices and Alireza Nikookar and Ahmad Razeghi for their technical support.

References

- [1] A. S. Joshi, I. Dincer, and B. V. Reddy, "Performance analysis of photovoltaic systems: a review," *Renewable and Sustainable Energy Reviews*, vol. 13, no. 8, pp. 1884–1897, 2009.
- [2] M. M. Farzad Jafarkazemi, M. Khademi, and A. Razeghi, "Performance prediction of flat-plate solar collectors using MLP and ANFIS," *Journal of Basic and Applied Scientific Research*, vol. 3, no. 2, pp. 196–200, 2013.
- [3] W. Zhou, H. Yang, and Z. Fang, "A novel model for photovoltaic array performance prediction," *Applied Energy*, vol. 84, no. 12, pp. 1187–1198, 2007.
- [4] M. Bayrakci, Y. Choi, and J. R. S. Brownson, "Temperature dependent power modeling of photovoltaics," *Energy Procedia*, vol. 57, pp. 745–754, 2014.
- [5] W. G. J. H. M. van Sark, "1.02—introduction to photovoltaic technology," in *Comprehensive Renewable Energy*, A. Sayigh, Ed., pp. 5–11, Elsevier, Oxford, UK, 2012.
- [6] K. Ishaque and Z. Salam, "A review of maximum power point tracking techniques of PV system for uniform insolation and partial shading condition," *Renewable and Sustainable Energy Reviews*, vol. 19, pp. 475–488, 2013.
- [7] A. Mellita and M. Benghalem, "Sizing of stand-alone photovoltaic systems using neural network adaptive model," *Desalination*, vol. 209, no. 1–3, pp. 64–72, 2007.
- [8] A. Mellit and S. A. Kalogirou, "Artificial intelligence techniques for photovoltaic applications: a review," *Progress in Energy and Combustion Science*, vol. 34, no. 5, pp. 574–632, 2008.
- [9] A. Mellit and S. A. Kalogirou, "MPPT-based artificial intelligence techniques for photovoltaic systems and its implementation into field programmable gate array chips: review of current status and future perspectives," *Energy*, vol. 70, pp. 1–21, 2014.
- [10] H. Belmili, M. Haddadi, S. Bacha, M. F. Almi, and B. Bendib, "Sizing stand-alone photovoltaic-wind hybrid system: techno-economic analysis and optimization," *Renewable and Sustainable Energy Reviews*, vol. 30, pp. 821–832, 2014.
- [11] E. İzgi, A. Öztopal, B. Yerli, M. K. Kaymak, and A. D. Şahin, "Short-mid-term solar power prediction by using artificial neural networks," *Solar Energy*, vol. 86, no. 2, pp. 725–733, 2012.

- [12] J. Ma, K. L. Manb, T. O. Tingb, N. Zhangb, S.-U. Guanb, and P. W. H. Wonga, "DEM: direct estimation method for photovoltaic ximum power point tracking," *Procedia Computer Science*, vol. 17, pp. 537–544, 2013.
- [13] P. Bhatnagar and R. K. Nema, "Maximum power point tracking control techniques: state-of-the-art in photovoltaic applications," *Renewable and Sustainable Energy Reviews*, vol. 23, pp. 224–241, 2013.
- [14] L. L. Jiang, D. R. Nayanasiri, D. L. Maskell, and D. M. Vilathgamuwa, "A hybrid maximum power point tracking for partially shaded photovoltaic systems in the tropics," *Renewable Energy*, vol. 76, pp. 53–65, 2015.
- [15] A. Abraham and B. Nath, "Hybrid heuristics for optimal design of artificial neural networks," in *Developments in Soft Computing*, vol. 9 of *Advances in Soft Computing*, pp. 15–22, Springer, Berlin, Germany, 2001.
- [16] H. Aryan, M. Khademi, and M. Pedram, "Prediction of photovoltaic panels output power by using MLP, RNN and neuroevolution models," *Advances in Natural and Applied Sciences*, vol. 8, no. 14, pp. 74–81, 2014.
- [17] D. T. Larose, *Discovering Knowledge in Data, an Introduction to Data Mining*, John Wiley & Sons, 2005.
- [18] O. Ekren, B. Y. Ekren, and B. Ozerdem, "Break-even analysis and size optimization of a PV/wind hybrid energy conversion system with battery storage—a case study," *Applied Energy*, vol. 86, no. 7-8, pp. 1043–1054, 2009.

Research Article

Modeling and Assessment of a Biomass Gasification Integrated System for Multigeneration Purpose

Shoab Khanmohammadi, Kazem Atashkari, and Ramin Kouhikamali

Department of Mechanical Engineering, Faculty of Engineering, University of Guilan, P.O. Box 3756, Rasht, Iran

Correspondence should be addressed to Kazem Atashkari; atashkar@guilan.ac.ir

Received 31 October 2015; Accepted 6 January 2016

Academic Editor: Ahmadreza Ghaffarizadeh

Copyright © 2016 Shoab Khanmohammadi et al. This is an open access article distributed under the Creative Commons Attribution License, which permits unrestricted use, distribution, and reproduction in any medium, provided the original work is properly cited.

The use of biomass due to the reduction in greenhouse gas emissions and environmental impacts has attracted many researchers' attention in the recent years. Access to an energy conversion system which is able to have the optimum performance for applying valuable low heating value fuels has been considered by many practitioners and scholars. This paper focuses on the accurate modeling of biomass gasification process and the optimal design of a multigeneration system (heating, cooling, electrical power, and hydrogen as energy carrier) to take the advantage of this clean energy. In the process of gasification modeling, a thermodynamic equilibrium model based on Gibbs energy minimization is used. Also, in the present study, a detailed parametric analysis of multigeneration system for undersigning the behavior of objective functions with changing design parameters and obtaining the optimal design parameters of the system is done as well. The results show that with exergy efficiency as an objective function this parameter can increase from 19.6% in base case to 21.89% in the optimized case. Also, for the total cost rate of system as an objective function it can decrease from 154.4 \$/h to 145.1 \$/h.

1. Introduction

One important issue which has attracted the attention of researchers in the recent years is the environmental problems and use of renewable energy sources to mitigate the global warming effects in energy conversion systems. The use of biomass as a clean fuel with organism sources as a suitable fuel with high conversion efficiency has been considered by many researchers.

Reducing fossil fuels dependency by utilizing new energies such as biomass is possible. The use of renewable fuels can significantly help reduce the effects of greenhouse gases and global warming phenomenon. A multigeneration system can generate some output products using one or more input energy. The main objectives of a multigeneration system include increase in efficiency, reduction in the environmental impacts, and reduction in final cost rate of products. In recent years, some studies have been done on trigeneration systems as a type of multigeneration and the use of renewable energies as the prime mover of such systems.

Li et al. [1] carried out a thermal-economic optimization for a distributed multigeneration energy system. They find the optimum system configuration, design, and operation under different economic and environmental legislation.

Al-Sulaiman et al. [2] modeled a trigeneration system including an Organic Rankine Cycle, a single effect absorption chiller, and a biomass burning unit and carried out an exergy and exergoeconomic analysis for the proposed system. The analysis of the system showed that biomass burner with 55% exergy destruction rate and organic Rankine Cycle evaporator with 38% have the maximum exergy destruction rate in the system. Chicco and Mancarella [3] investigated polygeneration system from thermodynamic and environmental impact point of view. In another study, Huang et al. [4] examined key, technical, and economic characteristics of a system combined with Organic Rankine Cycle and direct combustion of biomass. This study was performed for ash content of biomass from 0.57% to 14.26% and moisture content of 10.6. The results showed that, in the pure electric generation mode, maximum efficiency and final cost rate are 221 £/kWh and 11.1%, respectively. Also, for cogeneration heat

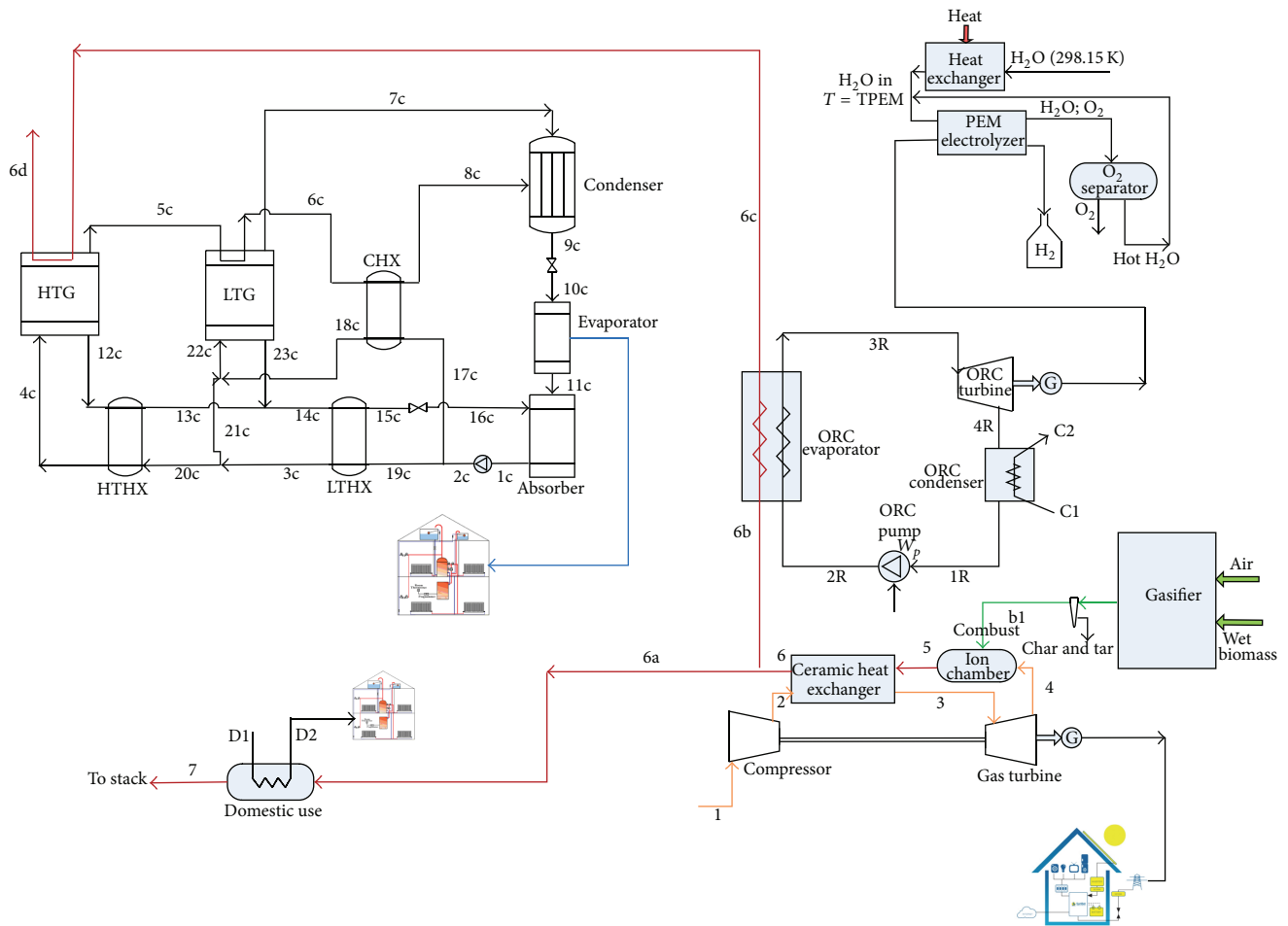


FIGURE 1: Schematic diagram of multigeneration system.

and power, maximum efficiency and cost rate were 87 £/kWh and 85%, and for trigeneration, maximum efficiency and cost rate were 103 £/kWh and 71.7%, respectively.

Rubio-Maya et al. [5] proposed a procedure based on the superstructure definition containing possible configurations of polygeneration system to produce electricity, heat, cool, and fresh water. They used an optimization procedure which included three important criteria, namely, energy saving aspects, greenhouse gas (GHG) emission, and economic factors. Hosseini et al. [6] investigated an integrated solid oxide fuel cell and a microgas turbine for desalination purposes. The results showed that the fuel cell stack pressure has a significant effect on the hybrid system and increase in the stack pressure increases the output power and fresh water capacity. Huang et al. [7] in their study examined a system with biomass feed for a number of residential buildings. In this study, a downdraft gasifier and different type of biomasses were used. They concluded that trigeneration system with heat to power ratio of 0.5 is suitable in residential buildings application. Furthermore, specific investment costs show that trigeneration system with biomass fuel for small units ranges from 2520 £/kWh to 2579 £/kWh. As the literature review shows, there is a gap in the multiobjective optimization of

multigeneration systems integrated with biomass gasification. The present study attempts to give a precise model of biomass gasification process using a thermodynamic equilibrium model based on Gibbs free energy minimization. Also, this exact model is used in a multigeneration system for cooling, heating, electric power generation, and hydrogen energy as an energy carrier. To obtain the optimum design parameters, an optimization procedure based on defined objectives is performed.

2. System Description

Figure 1 shows a schematic of the multigeneration system integrated with biomass gasification. The system consists of a gas turbine to be launched by hot air. A gasifier produces syngas using gasification of dry biomass. Produced syngas is combined with air exiting the gas turbine and generates combustion products at 1450 K in combustion chamber. Part of the combustion products after passing through ceramic heat exchanger enters an organic evaporator to run an Organic Rankin Cycle and after that by entering a double

TABLE 1: Thermodynamic properties of modeled system.

Point	Mass flow rate (kg/s)	Pressure (kPa)	Temperature (K)	Enthalpy (kJ/kg)
1	6.689	100	298.2	305.8
2	6.689	911.9	601	623.3
3	6.689	884.5	1250	1370
4	6.689	101.8	667.2	785.4
5	8.581	106.63	1400	1614
6	8.581	101.3	940.3	1032
6a	1.716	101.3	940.3	1032
6b	6.865	101.3	940.3	1032
6c	6.865	101.3	400	414.3
6d	6.865	101.3	373	385.5
7	1.716	101.3	400	414.3
1R	20.08	130.7	308	236.6
2R	20.08	1000	308.4	237.7
3R	20.08	1000	384.1	448.4
4R	20.08	130.7	326.4	417.6
D1	42.23	200	308	146.6
D2	42.23	200	338	272.1

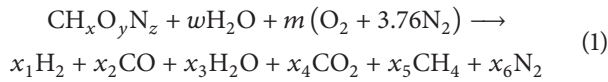
effect absorption chiller discharge to environment. Remaining combustion products enter into a heat exchanger with a lower temperature for generation of hot water and finally will be released in environment at 110°C. A proton exchange membrane (PEM) uses a part of electrical output of ORC to produce hydrogen as an energy carrier.

Table 1 shows some thermodynamic properties of multi-generation system.

3. Modeling

3.1. Thermodynamic Modeling

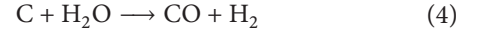
3.1.1. *Gasifier.* Thermodynamic equilibrium equations have been used for modeling the gasification process which take place in the gasifier. The general form of chemical reaction in the gas producer is assumed as [13]



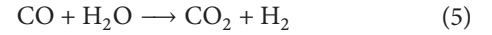
Here, $\text{CH}_x\text{O}_y\text{N}_z$ indicate the biomass chemical formula and w is the amount of water per kmol of biomass. All coefficients x_1 to x_6 can be obtained from atomic balance and using equilibrium constant equations. The procedure can be expressed as

$$\begin{aligned} x_2 + x_4 + x_5 &= 1, \\ 2x_1 + 2x_3 + 4x_5 &= x + 2w, \\ x_2 + x_3 + 2x_4 &= y + w + 2m, \\ x_2 + x_3 + 2x_4 &= y + 2m + w. \end{aligned} \quad (2)$$

The other equations can be obtained from equilibrium reaction. As it is expected pyrolysis products before reaching reduction region are fired and prior to emitting from gasifier achieve equilibrium state; the reactions can be written as follows:



Zainal et al. [12] and Higman and Van der Burgt [14] showed that (3) and (4) can be combined to give the water-gas shift reaction as follows:



Another equilibrium reaction is methane reaction, which can be expressed as



The equilibrium constants for water-gas shift reaction and methane reaction can be written as follows [11]:

$$K_1 = \frac{x_1 x_4}{x_2 x_3}, \quad (7)$$

$$K_2 = \frac{x_5}{x_1^2 n_{\text{total}}}.$$

The equilibrium constant can be obtained using Gibbs function change for each reaction as [8]

$$\ln K = -\frac{\Delta G_T^\circ}{RT}, \quad (8)$$

$$\Delta G_T^\circ = \sum_i v_i \Delta \bar{g}_{f,T,i}^\circ.$$

Here, ΔG_T° is the standard Gibbs free energy of reaction, and $\Delta \bar{g}_{f,T,i}^\circ$ shows the standard Gibbs function of formation at the given temperature T for the gas species i and \bar{R} is the universal gas constant, 8.314 kJ/(kmol·K). Finally, an energy balance is utilized to evaluate the gasification temperature (T_g) as follows [8]:

$$\begin{aligned} \bar{h}_{f,\text{biomass}}^\circ + w\bar{h}_{f,\text{H}_2\text{O}}^\circ &= x_1 (\bar{h}_{f,\text{H}_2}^\circ + \Delta \bar{h}) \\ &+ x_2 (\bar{h}_{f,\text{CO}}^\circ + \Delta \bar{h}) \\ &+ x_3 (\bar{h}_{f,\text{H}_2\text{O}}^\circ + \Delta \bar{h}) \\ &+ x_4 (\bar{h}_{f,\text{CO}_2}^\circ + \Delta \bar{h}) \\ &+ x_5 (\bar{h}_{f,\text{CH}_4}^\circ + \Delta \bar{h}) \\ &+ x_6 (\bar{h}_{f,\text{N}_2}^\circ + \Delta \bar{h}). \end{aligned} \quad (9)$$

\bar{h}_f° is the formation enthalpy in terms of kJ/kmol, and $\Delta \bar{h}^\circ$ is enthalpy difference for the given state with reference state. \bar{h}_f°

is the enthalpies of the formation of the biomass, moisture, hydrogen, carbon monoxide, water, carbon dioxide, methane, and nitrogen, respectively. To calculate LHV, the experimental relation used by Channiwala and Parikh [15] has been used:

$$\begin{aligned} \text{HHV} &= 0.3491\text{C} + 1.1783\text{H} + 0.1005\text{S} - 0.1034\text{O} \\ &\quad - 0.0151\text{N} - 0.0211\text{Ash}, \quad (10) \\ \text{LHV} &= \text{HHV} - 9m_{\text{H}}h_{fg}. \end{aligned}$$

The coefficients ASH, N, O, S, and H are the weight percent of the components of solid fuel, m_{H} is the weight percent of hydrogen in fuel, and h_{fg} is the water vapor enthalpy.

3.1.2. Organic Rankine Cycle. As it can be seen in Figure 1, the combustion products enter the Organic Rankine Cycle evaporator at 6b point and launch this cycle. The governing equations of the Organic Rankine Cycle at steady state condition are mass balance and energy balance; more detail can be found in [16].

3.1.3. Proton Exchange Membrane (PEM) Electrolyzer. In this research hydrogen is used as our energy carrier. Thus, a PEM electrolyzer for hydrogen production is used. The electricity and heat are fed to the electrolyzer to drive the electrochemical reactions in PEM electrolyzer. As shown in Figure 1, liquid water at ambient temperature enters a heat exchanger that heats it to the PEM electrolyzer temperature before it enters the electrolyzer. Leaving the cathode at the reference temperature, the hydrogen produced is stored in a storage tank. The oxygen gas produced at the anode is separated from the water and oxygen mixture and then cooled to the reference environment temperature. The remaining water is returned to the water supply stream for the next hydrogen production cycle. The overall PEM electrolysis reaction is water splitting; that is, electricity and heat are used to separate water into hydrogen and oxygen.

The mass flow rate of hydrogen produced from PEM electrolyzer can be calculated as

$$\dot{m}_{\text{H}_2} = \eta_{\text{elec}} \frac{\dot{W}_{\text{net,ORC}}}{\text{HHV}_{\text{H}_2}}. \quad (11)$$

Here η_{elec} is efficiency of the electrolyzer which is about 60% and HHV_{H_2} is the higher heating value of hydrogen which is 142.19×10^6 J/kg. The exergy of hydrogen stream can be calculated as

$$\text{ex}_{\text{H}_2} = \text{ex}_{\text{ph,H}_2} + \text{ex}_{\text{ch,H}_2}. \quad (12)$$

The physical and chemical exergy of hydrogen are given as [17]

$$\begin{aligned} \text{ex}_{\text{ph,H}_2} &= (h_{\text{H}_2} - h_{\text{o,H}_2}) - T_0 (s_{\text{H}_2} - s_{\text{o,H}_2}), \\ \text{ex}_{\text{ch,H}_2} &= \frac{253153}{\text{MW}_{\text{H}_2}}. \end{aligned} \quad (13)$$

More details about thermochemical modeling of the PEM electrolyzer are given elsewhere [18].

3.1.4. Gas Turbine. The governing equation on the gas turbine cycle that is used for the thermodynamic modeling of the system components is as follows:

$$\begin{aligned} \dot{W}_{\text{GT}} &= \dot{m}_3 (h_3 - h_4), \\ \eta_{\text{Eva,organic}} &= \frac{\dot{m}_5 (h_5 - h_6)}{\dot{m}_2 (h_3 - h_2)}, \\ \eta_{\text{is,comp}} &= \frac{h_{2s} - h_1}{h_2 - h_1}, \\ \dot{m}_4 h_4 + \dot{m}_{b_1} h_{b_1} &= \dot{m}_5 h_5. \end{aligned} \quad (14)$$

To calculate the chemical exergy of the fuel, lower heating value and the coefficient β are required and written as follows [19, 20]:

$$\begin{aligned} \text{ex}_{\text{biomass}} &= \beta \text{LHV}_{\text{wood}}, \\ \text{HHV (kJ/kg)} &= 349.1\text{C} + 1178.3\text{H} + 100.5\text{S} - 103.4\text{O} - 15.1\text{N} - 21.1\text{ASH}, \\ \beta &= \frac{1.044 + 016 (Z_{\text{H}}/Z_{\text{C}}) - .34493 (Z_{\text{O}}/Z_{\text{C}}) (1 + .0531 (Z_{\text{H}}/Z_{\text{C}}))}{1 - 0.4124 (Z_{\text{O}}/Z_{\text{C}})}. \end{aligned} \quad (15)$$

Z_{O} , Z_{H} , and Z_{C} are the mass components of carbon, hydrogen, oxygen, and nitrogen in biomass. For the studied biomass with the presented chemical formula and the above equation, the higher heating value of fuel is 19980 kJ/kg. Also, the lower heating value of the biomass can be calculated by the following equation and given that $h_{fg} = 2258$ kJ/kg [20]:

$$\text{LHV (kJ/kg)} = \text{HHV} - h_{fg} \left(\frac{9\text{H}}{100} + \frac{\text{M}}{100} \right). \quad (16)$$

In the above equation, H and M are the percent of hydrogen and moisture content, respectively.

3.1.5. Double Effect Absorption Chiller. This type of chiller can be used for ventilation and cooling purposes. Compared to the compressed cooling system, this system requires less shaft work for cooling generation. Water-ammonium is a widely used working fluid and is used in absorption systems and multigeneration objectives. In the system analysis, the

mass conservation law and energy balance are used for each component of double effect absorption chiller as a control volume. The law of conservation of mass for the overall mass and component conservation for each component of the solution in a steady mode and constant current is written as follows:

$$\begin{aligned}\sum \dot{m}_i &= \sum \dot{m}_o, \\ \sum (\dot{m}x)_i &= \sum (\dot{m}x)_o.\end{aligned}\quad (17)$$

Here, \dot{m} is the mass flow rate of working fluid and x is the concentration of ammonium in the solution. The energy equilibrium for the system components is written as follows [21]:

$$\dot{Q} - \dot{W} = \sum_o \dot{m}_o h_o - \sum_i \dot{m}_i h_i. \quad (18)$$

(a) *Exergy Analysis.* To obtain the exergy of each point of the cycle, by considering the control volume for each component in the steady state, the exergy balance equation is as follows:

$$\sum_i \dot{m}_i \text{ex}_i = \sum_o \dot{m}_o \text{ex}_o + \dot{I}. \quad (19)$$

The exergy of different points is composed of two parts including physical exergy and chemical exergy:

$$\text{ex} = \text{ex}_{\text{ph}} + \text{ex}_{\text{ch}}. \quad (20)$$

The chemical exergy of each state depends on its pressure and temperature that is shown as follows:

$$\text{ex}_{\text{ph}} = (h - h_o) - T_o (s - s_o). \quad (21)$$

In general, the chemical exergy for a gas mixture can be obtained by the following equation:

$$\text{ex}_{\text{ch}} = \sum_i x_i \text{ex}_{o,i}^{\text{ch}} + \bar{R}T_o \sum_i x_i \ln x_i, \quad (22)$$

where x_i is the molar fraction of the i th component and $\text{ex}_{o,i}^{\text{ch}}$ is the standard exergy of the i th pure material. In the absorption chiller, as ammonium water solution is not ideal, the following equation is used for calculating the chemical exergy:

$$\bar{\text{ex}}_{\text{ch}} = \left(\frac{1}{\bar{M}_{\text{sol}}} \right) \left[\sum_{i=1}^n y_i \bar{\text{ex}}_{\text{ch}}^k + \bar{R}T_o \sum_{i=1}^n y_i \ln(a_i) \right]. \quad (23)$$

With the extension of the above equation for the ammonium water solution, the following can be written:

$$\begin{aligned}\bar{\text{ex}}_{\text{ch}} \\ = \left(\frac{1}{\bar{M}_{\text{sol}}} \right) \left[y_{\text{H}_2\text{O}} \bar{\text{ex}}_{\text{H}_2\text{O}}^o + y_{\text{NH}_3} \bar{\text{ex}}_{\text{NH}_3}^o + \bar{R}T_o \right. \\ \left. \left[(y_{\text{H}_2\text{O}} \ln(a_{\text{H}_2\text{O}}) + y_{\text{NH}_3} \ln(a_{\text{NH}_3})) \right] \right],\end{aligned}\quad (24)$$

where $a_{\text{H}_2\text{O}}$ is water activity and is the ratio of water vapor pressure in the mixture to pure water pressure and

a_{NH_3} is ammonium activity which is considered as ratio of ammonium vapor pressure in the mixture to pure water pressure. This equation is composed of two parts: the standard chemical exergy of the pure material and the exergy caused by separation process as follows:

$$\begin{aligned}\bar{\text{ex}}_{\text{ch}}^o &= \left(\frac{1}{\bar{M}_{\text{sol}}} \right) \left[y_{\text{H}_2\text{O}} \bar{\text{ex}}_{\text{H}_2\text{O}}^o + y_{\text{NH}_3} \bar{\text{ex}}_{\text{NH}_3}^o \right], \\ \bar{\text{ex}}_{\text{ch}}^{\text{dis}} &= \left(\frac{1}{\bar{M}_{\text{sol}}} \right) \left[y_{\text{H}_2\text{O}} \ln(a_{\text{H}_2\text{O}}) + y_{\text{NH}_3} \ln(a_{\text{NH}_3}) \right],\end{aligned}\quad (25)$$

where y_i as a molar fraction is as follows:

$$y_{\text{H}_2\text{O}} = \frac{(1 - x_{1w}) \bar{M}_{\text{NH}_3}}{(1 - x_{1w}) \bar{M}_{\text{NH}_3} + x_{1w} \bar{M}_{\text{H}_2\text{O}}}, \quad (26)$$

$$y_{\text{NH}_3} = 1 - y_{\text{H}_2\text{O}}.$$

And x_{1w} is defined as follows:

$$x_{1w} = \frac{x_{\text{NH}_3}}{100}, \quad (27)$$

where x_{NH_3} is the concentration of ammonium water concentration in a percent form and \bar{M}_{NH_3} and $\bar{M}_{\text{H}_2\text{O}}$ are 17 kg/kmol and 18 kg/kmol, respectively.

(b) *Economic Analysis.* The main aim of the economic modeling is to obtain the cost functions of each component and a calculation of the final cost rate of the system. There are various methods for determining purchase equipment cost in terms of the designed parameters. Here, the function is presented by Bejan and Moran [22], Ahmadi [23], and Soltani et al. [24], with some modifications done in accordance with local conditions and interest rate in Iran. Table 2 shows the cost functions for each component of the trigeneration system in terms of design parameters.

(c) *System Assessment.* To perform an exact evaluation of the system and the impact of the design parameters on thermodynamic and economic performance, the exergy efficiency and the final cost rate are considered as two objective functions. These objective functions are defined as follows:

$$\psi = \frac{\dot{\text{E}}x_{\text{Q,domestic}} + \dot{\text{E}}x_{\text{Cooling}} + \dot{W}_{\text{net}} + \dot{m}_{\text{H}_2} \text{ex}_{\text{H}_2}}{\dot{\text{E}}x_{\text{biomass}}}, \quad (28)$$

$$\dot{C}_{\text{total}} = \dot{Z}_{\text{total}} + \dot{C}_{\text{biomass}}, \quad (29)$$

$$\begin{aligned}\dot{Z}_{\text{total}} &= \dot{Z}_{\text{comp}} + \dot{Z}_{\text{GT}} + \dot{Z}_{\text{AP}} + \dot{Z}_{\text{CC}} + \dot{Z}_{\text{DHW}} + \dot{Z}_{\text{Chiller}} \\ &+ \dot{Z}_{\text{Pump,R}} + \dot{Z}_{\text{Eva,R}} + \dot{Z}_{\text{Tur,R}} + \dot{Z}_{\text{Cond,R}} \\ &+ \dot{Z}_{\text{PEM}}.\end{aligned}\quad (30)$$

In the above equation \dot{C}_{biomass} is the biomass cost which is obtained from an analysis of local data and wood purchase costs.

TABLE 2: The cost function for each composition of the multigeneration system in terms of design parameters [8, 9].

Component	Cost function	
Air compressor	$Z_{AC} = \left(\frac{C_{11}}{C_{12} - \eta_{sc}} \right) r_p \ln(r_p)$	$C_{11} = 71.1 \text{ \$/}(\text{kgs}^{-1})$ $C_{12} = 0.9$
Combustion chamber	$Z_{CC} = \left(\frac{C_{21} \dot{m}_a}{C_{22} - 0.98} \right) (1 + \exp(C_{32} T_{comb} - C_{24}))$	$C_{21} = 46.08, C_{22} = 0.995$ $C_{23} = 0.018, C_{24} = 26.4$
Gas turbine	$Z_{GT} = \left(\frac{C_{31} \dot{m}_g}{C_{32} - \eta_{GT}} \right) \ln \left(\frac{P_4}{P_3} \right) (1 + \exp(C_{33} T_3 - C_{34}))$	$C_{31} = 479.34, C_{32} = 0.92$ $C_{33} = 0.036, C_{34} = 54.4$
Air preheater	$Z_{AP} = C_{41} \left(\frac{\dot{m}_5 (h_5 - h_6)}{U \Delta T_{LM}} \right)^{0.6}$	$U = 6, C_{41} = 4122$
Gasifier	$Z_{gasif} = 1600 (3600 \times \dot{m}_{biomass})^{0.67}$	—
Domestic hot water	$Z_{DHW} = 0.3 \dot{m}_{DHW}$	—
ORC evaporator	$Z_{Eva} = 309.14 (A_{Eva})^{0.85}$	—
ORC pump	$Z_{Pump} = 200 (\dot{W}_{Pump})^{0.65}$	—
ORC turbine	$Z_{Tur} = 4750 (\dot{W}_{Tur})^{0.75}$	—
ORC condenser	$Z_{Condenser} = 516.62 (A_{Condenser})^{0.6}$	—
Double effect absorption chiller	$Z_{Chiller} = 1144.3 (\dot{Q}_{Eva})^{0.67}$	—
PEM electrolyzer	$Z_{PEM} = 1000 (\dot{W}_{PEM,in})$	—

TABLE 3: A comparison of the modeling syngas composition and experimental result.

Composition	The present model	Experimental [10]	Jarunghammachote and Dutta [11] MC = 16%	Zainal et al. [12]
H ₂	24.52	17	18.03	21.06
CO	26.8	18.4	18.51	19.6
CO ₂	11.03	10.6	11.43	12.01
CH ₄	2.43	1.3	0.11	0.64
N ₂	42	52.7	51.92	46.68

4. Result and Discussion

4.1. Model Validation. Biomass gasification process is the most important part of the thermodynamic modeling of the multigeneration system. To validate the developed thermodynamic equilibrium model, the results are compared to those of other studies. In order to determine the error of the modeling, the root mean square error of syngas compounds with compounds derived from experimental results [10] and also other researchers' modeling [11] is used. Table 3 shows the syngas compounds produced in the present model, experimental results also the work of others.

As it can be seen, there is a reasonable consistency between the present modeling results and the experimental results by Jayah et al. [10]. The maximum deviation from the experimental results is related to methane. The calculations indicate that root mean square error of the experimental results and the present modeling is 6.9. Also, the error of the present modeling results in the work by Jarunghammachote and Dutta [11] is 6.55. Figure 2 shows the mole fraction of each component of syngas.

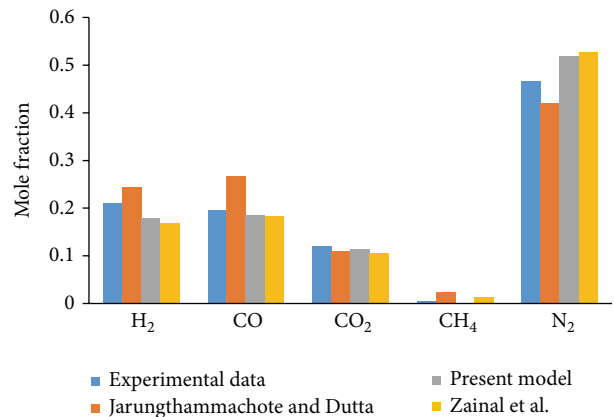


FIGURE 2: Mole fraction of syngas for present and other experimental and numerical studies.

4.2. Exergy Analysis Result. Table 4 presents the different important parameters of multigeneration system under initial operation conditions. The results indicate that the exergy

TABLE 4: Performance parameters of multigeneration system for the initial state.

Parameter	Unit	Value
Fuel (biomass) flow rate	kg/s	0.6
Exergy efficiency	%	19.69
Energy efficiency	%	19.36
Gasification air mass flow rate	kg/s	1.04
Combustion air mass flow rate	kg/s	6.68
ORC turbine output	kW	616.6
Gas turbine output	kW	1798
Domestic hot water flow rate	kg/s	42.16
Gasifier purchase cost	\$/h	5.9
Compressor purchase cost	\$/h	4.16
Gas turbine cost rate	\$/h	2.08
Heat exchanger cost rate	\$/h	5.14
Combustion chamber cost rate	\$/h	0.47
Domestic water heater cost rate	\$/h	0.22
Organic Rankine Cycle cost rate	\$/h	11.53
Biomass fuel cost	\$/GJ	2

efficiency of multigeneration system is 19.69%. Also, the domestic hot water flow rate in the initial state is 42.16 kg/s. The economic results show that the ORC unit and gasifier with 11.53 \$/h and 5.9 \$/h have the highest cost rate compared with other components.

4.3. Parametric Analysis. In order to determine the effects of the key parameters on the system performance, a parametric study is done. Given that the gasification temperature can significantly impact the percent of the syngas components, to study the impacts of the change in such parameter, its value has changed from 950 K to 1250 K. Figure 3 shows the range of such changes. As it could be seen, increase in the gasification temperature can reduce both overall system efficiency and costs simultaneously. Given that changes in gasification temperature can directly influence the percent of the generated gases, it can influence the air required for complete combustion in combustion chamber. By an increase in the relevant range, it can be found that the air required for combustion decreases from 7.57 kg/s to 5.88 kg/s.

Figure 4 shows the effect of this parameter on the main output of the system. The results indicate that cooling capacity and hot water output are not sensitive to change the gasification temperature while electricity output of the system decreases with an increment in the gasification temperature. Also, the hydrogen production rate in changing range of gasification temperature experiences an increment and decrement trend. It should be noted that such behavior is due to increment and decrement trend of electrical output of ORC. When the gasification temperature increases, there are two opposite effects.

To investigate the combustion temperature effects on the system performance this parameter is changed from 1300 K to

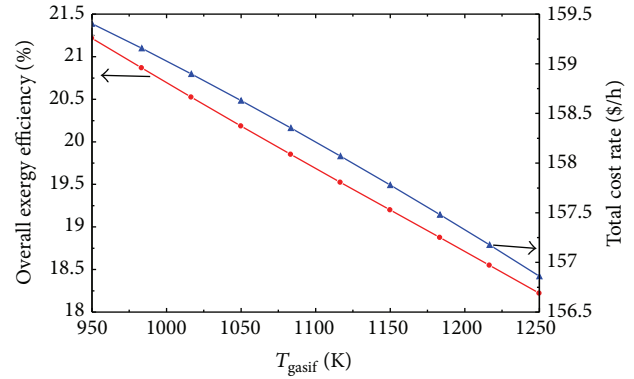


FIGURE 3: The impact of the gasification temperature on the objective functions.

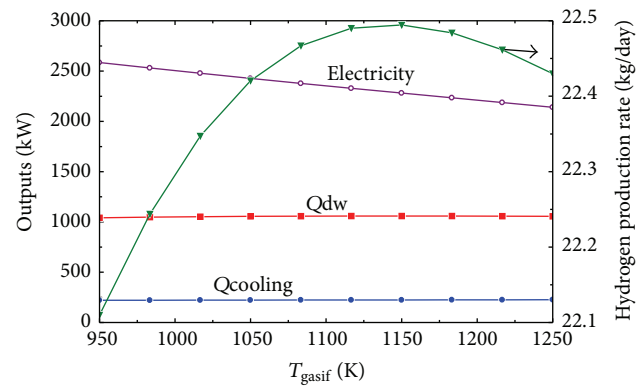


FIGURE 4: The impact of the gasification temperature on the main outputs. Qdw: domestic water heater. Qcooling: absorption chiller output.

1400 K. It can be seen in the higher combustion temperature that the exergy efficiency of the system and total cost rate of the system experience lower values (Figure 5).

The changing of the main outputs of the system with variation of combustion temperature of syngas is illustrated in Figure 6. As it can be seen the cooling capacity of the system has no change with combustion temperature change, while hydrogen production rate and domestic hot water increase with combustion temperature increment. It can be found that in the reasonable range of combustion temperature the total electricity output decreases from 2534 kW to 2353 kW. Since the decrement in the electricity output of the system is higher than increment in the exergy of produced hydrogen, the exergy efficiency decreases with raising the combustion temperature.

One of the main parameters effective in the system performance is compressor pressure ratio. The result shows that increase in the compressor pressure ratio leads to energy and exergy efficiency to a limited extent. Figure 7 presents that for the pressure ratio higher than 9.5 the energy efficiency will decrease. Since the higher pressure ratio imposes more work to derive compressor, the exergy and energy efficiency in higher pressure ratio show a decrement.

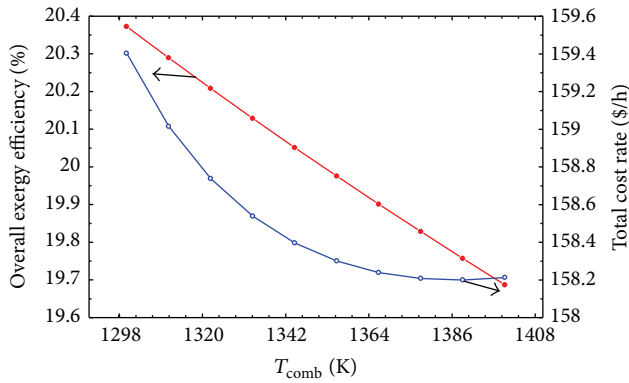


FIGURE 5: The impact of the combustion temperature on the two objective functions.

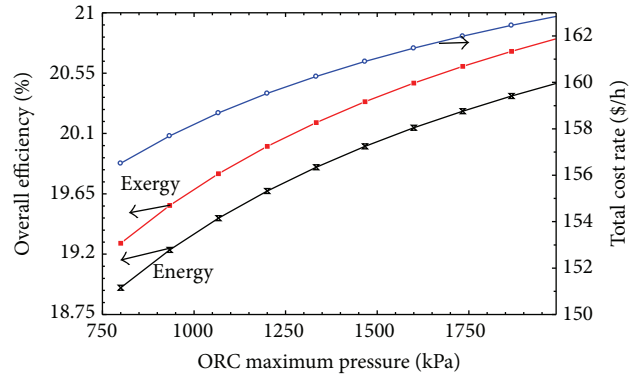


FIGURE 8: The impact of the compressor pressure ratio on the maximum pressure of ORC.

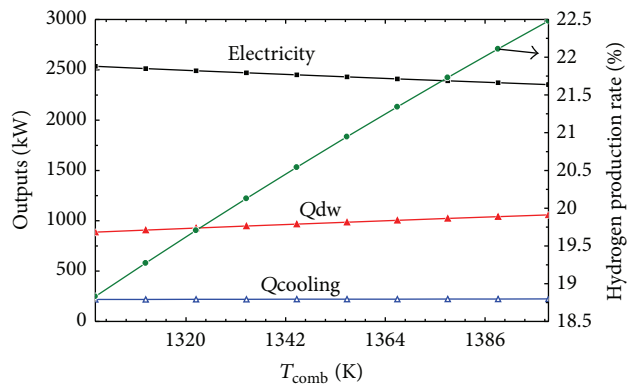


FIGURE 6: The impact of the combustion temperature on the main outputs. Qdw: domestic water heater. Qcooling: absorption chiller output.

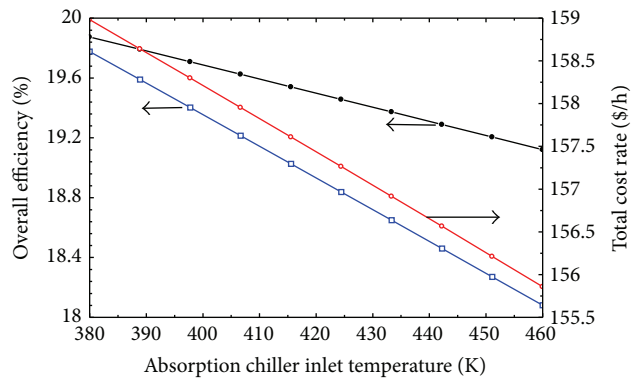


FIGURE 9: The impact of the inlet temperature to chiller on the objective functions.

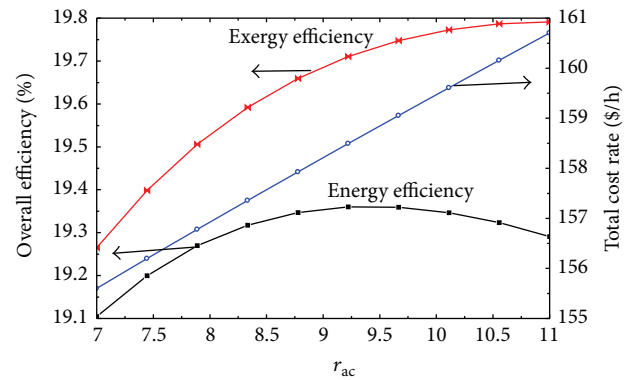


FIGURE 7: The impact of the compressor pressure ratio on the cost rate and efficiencies.

An important parameter which has a severe effect on the ORC performance is the ORC maximum pressure. To examine the influence of this parameter, the maximum pressure in the range of 800 kPa to 2000 kPa has been considered as variable. As it can be seen in Figure 8 an increase in Organic Rankine Cycle pressure simultaneously increases the overall cost of the system, energy efficiency, and exergy efficiency.

The higher ORC maximum pressure leads to the higher work output from organic turbine which results in increase in the exergy and energy efficiency of the system. At the higher ORC maximum pressure the cost of the ORC components increases which leads to increase in the total cost rate of the system as it can be seen in Figure 9.

Also, Figure 9 illustrates the effect of changing inlet temperature to the chiller on the total cost rate, energy efficiency, and exergy efficiency. The results exhibit that an increment in the inlet temperature to chiller decreases energy efficiency, exergy efficiency, and total cost rate of the system. Increasing this parameter has two effects on the system. Increasing this temperature could lead to increase in cooling capacity and on the other hand decrease in the ORC power output because of lower energy gain in the ORC evaporator.

Due to the change of molar fraction of syngas composition, the biomass moisture content can significantly impact the system performance. As it could be seen in Figure 10, by increasing the moisture from 0.1 to 0.3, the system overall cost rate and the second law efficiency are reduced substantially.

The ratio of the mass flow rate for ORC evaporator (\dot{m}_{eb}) to the mass flow rate of ceramic heat exchanger (\dot{m}_c) is bypass ratio. The result of bypass ratio variation demonstrates that an increment in this parameter results in an increment in the

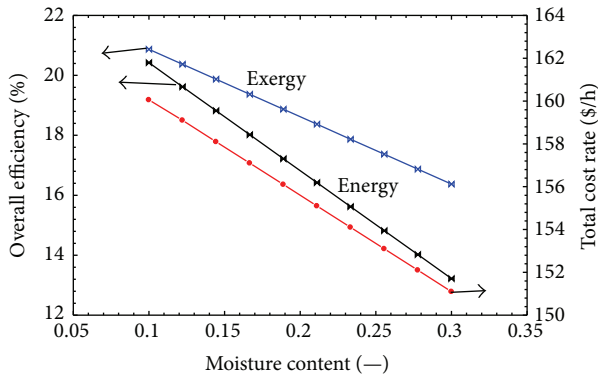


FIGURE 10: The impact of the biomass moisture content on the objective functions.

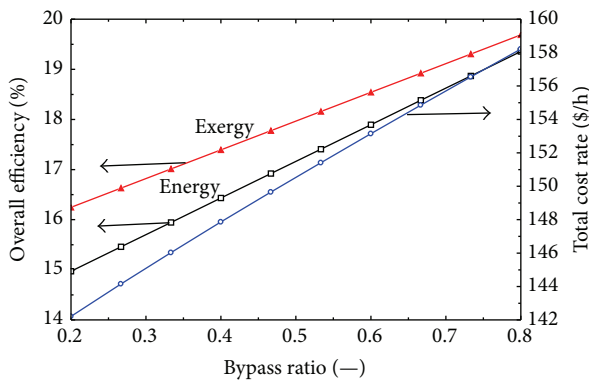


FIGURE 11: The impact of the bypass ratio on the objective functions.

energy efficiency, exergy efficiency, and total cost rate of the multigeneration system (Figure 11).

The parametric study of multigeneration system reveals that the design parameters have different effects on the thermodynamic and economic performance of the system. To select the best value of design parameters an optimization method should be done. In the following section the optimization procedure is described.

5. Optimization Results

To optimize the performance of the system two objective functions in (28) and (29) are defined. Seven decision variables, namely, gasification temperature, combustion temperature, compressor pressure ratio, moisture content of biomass, temperature inlet to the chiller, bypass ratio, and maximum pressure of ORC, are selected to carry out optimization. Table 5 represents the reasonable range of decision variables.

In this study the genetic optimization option of EES is used to find the optimized value of problem. Genetic algorithm as a repetitive algorithm with random search strategy and biological evolution modeling attempts to find optimal solutions. Exergy efficiency and total cost rate are selected separately as two objective functions. The result of optimization is presented in Table 6.

TABLE 5: Reasonable range of decision variables.

Decision variables	Lower bound	Upper bound
Gasification temperature (K)	950	1150
Combustion temperature (K)	1300	1400
Compressor pressure ratio (—)	7	11
Moisture content of biomass (—)	0.1	0.6
Temperature inlet to the chiller (K)	383	460
Bypass ratio (—)	0.2	0.8
Maximum pressure of ORC (kPa)	800	1200

The result of optimization indicates that the exergy efficiency of the system can increase to 21.89% and total cost rate of the system can reduce to 145.1 \$/h.

6. Conclusion

Biomass is clean and available and is a type of renewable energy source that is derived from biomass resources. Biomass energy can be used for direct combustion or gasification process. Accurate modeling of biomass gasification is highly important due to the complex reactions of the gasification process. In this study a multigeneration system integrated with biomass gasifier unit is investigated. A parametric study and a single objective optimization are carried out. The result of parametric study for seven decision variables is presented. The optimization results reveal that the exergy efficiency of the multigeneration system increases about 2.29% and total cost rate of system can decrease 13.1 \$/h compared to the initial state of the system.

Nomenclature

\dot{C} :	Cost rate (\$/h)
DHW:	Domestic hot water heater
ex:	Exergy (kJ/kg)
HHV:	Higher heating value (kJ/kg)
LHV:	Lower heating value (kJ/kg)
m :	Number of moles required for firing per kmol of wood
\dot{m} :	Mass flow rate (kg/s)
ORC:	Organic Rankine Cycle
r_p :	Pressure ratio
T :	Temperature
w :	Amount of water per kmol of biomass
Z :	Cost of component.

Subscripts

AP:	Air preheater
C:	Carbon
CC:	Combustion chamber
ch:	Chemical
comb:	Combustion
comp:	Compressor
Cond,R:	Organic condenser
Eva,R:	Organic evaporator

TABLE 6: Optimization results of multigeneration system.

	T_{gasif} (K)	r_{ac} (—)	P_{2R} (kPa)	x_{bypass} (—)	MC (—)	T_{comb} (K)	$T_{\text{inlet,chiller}}$ (K)	Exergy eff. (%)	Total cost rate (\$/h)
Exergy efficiency as objective function									
Design	1100	9	1000	0.8	0.6	1400	400	19.6	158.2
Optimum	1050	8.99	1125	0.54	0.1	1362	412	21.89	154.4
Variation	-4.55	-0.11	12.5	-32.5	-83.3	-2.71	3	11.68	-2.4
Total cost rate as objective function									
Optimum	1100	9	1125	0.44	0.3	1325	430	15.3	145.1
Variation	0	0	12.5	-45	-50	-5.4	7.5	-21.9	-8.3

f : Formation
 gasif: Gasification
 GT: Gas turbine
 h : Enthalpy (kJ/kg)
 K : Equilibrium constant
 ph: Physical
 Prod: Product
 Pump,R: Organic pump
 \bar{R} : Universal gas constant (kJ/kg·K)
 Tur,R: Organic turbine
 \circ : Reference state.

Greek Symbols

β : Biomass exergy coefficient
 ψ : Exergy efficiency.

Conflict of Interests

The authors declare that there is no conflict of interests regarding the publication of this paper.

Acknowledgment

The authors would like to thank National Iranian Gas Company (NIGC) for the helpful support.

References

- [1] H. Li, R. Nalim, and P.-A. Haldi, "Thermal-economic optimization of a distributed multi-generation energy system—a case study of Beijing," *Applied Thermal Engineering*, vol. 26, no. 7, pp. 709–719, 2006.
- [2] F. A. Al-Sulaiman, I. Dincer, and F. Hamdullahpur, "Energy and exergy analyses of a biomass trigeneration system using an organic Rankine cycle," *Energy*, vol. 45, no. 1, pp. 975–985, 2012.
- [3] G. Chicco and P. Mancarella, "A unified model for energy and environmental performance assessment of natural gas-fueled poly-generation systems," *Energy Conversion and Management*, vol. 49, no. 8, pp. 2069–2077, 2008.
- [4] Y. Huang, Y. D. Wang, S. Rezvani et al., "A techno-economic assessment of biomass fuelled trigeneration system integrated with organic Rankine cycle," *Applied Thermal Engineering*, vol. 53, no. 2, pp. 325–331, 2013.
- [5] C. Rubio-Maya, J. Uche-Marcuello, A. Martínez-Gracia, and A. A. Bayod-Rújula, "Design optimization of a polygeneration plant fuelled by natural gas and renewable energy sources," *Applied Energy*, vol. 88, no. 2, pp. 449–457, 2011.
- [6] M. Hosseini, I. Dincer, P. Ahmadi, H. B. Avval, and M. Ziaasharhagh, "Thermodynamic modelling of an integrated solid oxide fuel cell and micro gas turbine system for desalination purposes," *International Journal of Energy Research*, vol. 37, no. 5, pp. 426–434, 2013.
- [7] Y. Huang, Y. D. Wang, S. Rezvani, D. R. McIlveen-Wright, M. Anderson, and N. J. Hewitt, "Biomass fuelled trigeneration system in selected buildings," *Energy Conversion and Management*, vol. 52, no. 6, pp. 2448–2454, 2011.
- [8] S. Khanmohammadi, K. Atashkari, and R. Kouhikamali, "Exergoeconomic multi-objective optimization of an externally fired gas turbine integrated with a biomass gasifier," *Applied Thermal Engineering*, vol. 91, pp. 848–859, 2015.
- [9] M. R. Meigounpoory, P. Ahmadi, A. R. Ghaffarizadeh, and S. Khanmohammadi, "Optimization of combined cycle power plant using sequential quadratic programming," in *Proceedings of the ASME Heat Transfer Summer Conference Collocated with the Fluids Engineering, Energy Sustainability, and 3rd Energy Nanotechnology Conferences*, pp. 109–114, American Society of Mechanical Engineers, Jacksonville, Fla, USA, August 2008.
- [10] T. H. Jayah, L. Aye, R. J. Fuller, and D. F. Stewart, "Computer simulation of a downdraft wood gasifier for tea drying," *Biomass and Bioenergy*, vol. 25, no. 4, pp. 459–469, 2003.
- [11] S. Jarunghammachote and A. Dutta, "Thermodynamic equilibrium model and second law analysis of a downdraft waste gasifier," *Energy*, vol. 32, no. 9, pp. 1660–1669, 2007.
- [12] Z. A. Zainal, R. Ali, C. H. Lean, and K. N. Seetharamu, "Prediction of performance of a downdraft gasifier using equilibrium modeling for different biomass materials," *Energy Conversion and Management*, vol. 42, no. 12, pp. 1499–1515, 2001.
- [13] N. S. Barman, S. Ghosh, and S. De, "Gasification of biomass in a fixed bed downdraft gasifier—a realistic model including tar," *Bioresource Technology*, vol. 107, pp. 505–511, 2012.
- [14] C. Higman and M. Van der Burgt, *Gasification*, Gulf Professional Publishing, 2011.
- [15] S. A. Channiwala and P. P. Parikh, "A unified correlation for estimating HHV of solid, liquid and gaseous fuels," *Fuel*, vol. 81, no. 8, pp. 1051–1063, 2002.
- [16] S. Khanmohammadi, K. Atashkari, and R. Kouhikamali, "Performance assessment and multi-objective optimization of a trigeneration system with a modified biomass gasification model," *Modares Mechanical Engineering*, vol. 15, no. 9, pp. 209–222, 2015.

- [17] S. Ozlu, *Development and Analysis of Solar Energy Based Multigeneration Systems*, University of Ontario Institute of Technology, 2015.
- [18] P. Ahmadi, I. Dincer, and M. A. Rosen, "Energy and exergy analyses of hydrogen production via solar-boosted ocean thermal energy conversion and PEM electrolysis," *International Journal of Hydrogen Energy*, vol. 38, no. 4, pp. 1795–1805, 2013.
- [19] S. Soltani, S. M. S. Mahmoudi, M. Yari, T. Morosuk, M. A. Rosen, and V. Zare, "A comparative exergoeconomic analysis of two biomass and co-firing combined power plants," *Energy Conversion and Management*, vol. 76, pp. 83–91, 2013.
- [20] P. Basu, *Biomass Gasification and Pyrolysis: Practical Design and Theory*, Academic Press, 2010.
- [21] H. Ganjehsarabi, A. Gungor, and I. Dincer, "Exergoeconomic evaluation of a geothermal power plant," *International Journal of Exergy*, vol. 14, no. 3, pp. 303–319, 2014.
- [22] A. Bejan and M. J. Moran, *Thermal Design and Optimization*, John Wiley & Sons, 1996.
- [23] P. Ahmadi, *Modeling, Analysis and Optimization of Integrated Energy Systems for Multigeneration Purposes*, Faculty of Engineering and Applied Science, University of Ontario Institute of Technology, 2013.
- [24] S. Soltani, S. M. S. Mahmoudi, M. Yari, and M. A. Rosen, "Thermodynamic analyses of a biomass integrated fired combined cycle," *Applied Thermal Engineering*, vol. 59, no. 1-2, pp. 60–68, 2013.